University of Rome Sapienza

National Institute for Astrophysics (INAF)

University of Rome Tor Vergata

PhD thesis:

On the dynamical evolution of a young planetary system

Thesis Advisor:
Prof. Roberto Capuzzo Dolcetta

Candidate:
Raffaele Stefano Cattolico

A. A. 2018 - 2019

To Andrea.

Contents

Chapter 1

Introduction

The dynamical evolution of planetary and protoplanetary structures represents one of the major challenges in the modern computational astrophysics. Celestial mechanics, which is the main theoretical tool, saw a large development leading to the great successes of the discovery of external planets of the solar system and the intra-solar system probes. Unfortunately, the field of planetary dynamics has been little considered in the recent past because it seemed that most of the output has already been obtained. Nowadays, with the ever rising number of exoplanetary systems discoveries and with the increasing details in the information about their characteristics and architectures, it has become clear that an interpretation on the base of a study of their dynamics is getting more and more important, in particular when the system is young and still embedded in a stellar environment. The focus of this thesis is to investigate the dynamical evolution of a young planetary system under exogenous perturbations in a typical open stellar cluster.

We start, in Chapter 2, explaining the characteristics of planetary and protoplanetary systems, investigating their structure and evolution in the light of thousand

extrasolar planetary systems discovered in the last decades.
In Chapter 3 we explain the planet-disk interactions in presence of a low-mass gaseous disk when a young planet is still forming (Type I migration) and when it is fully formed (Type II migration).
In Chapter 4 we deal with the state of the art of the numerical investigations of young circumstellar structures, exploiting a modern hydrodynamical approach: Smoothed Particles Hydrodynamic (SPH).
In Chapter 5, we show the results of our numerical simulations of the dynamics of a young planetary system embedded in a young stellar cluster.
Finally, in Chapter 6, we discuss some relevant astrophysical aspects and implications and potential future perspectives are outlined in Chapter 7.
Part of this work has been done in collaboration with the Racah Institute of Physics at The Hebrew University of Jerusalem (Israel) and the Department of Astrophysics in the Rose Center for Earth and Space at the American Museum of Natural History (USA).

Chapter 2

Protoplanetary disks and planetary systems

A protoplanetary system is a structure composed by a young central star surrounded by gas, dust and planetary seeds. It represents the ancestor of planetary systems like our Solar System. The young central star, usually called *protostar*, is in the early stage of the star formation, before the beginning of its inner nucleosynthesis. The dust component is generally a fraction (in mass) $\frac{1}{100}$ of the gaseous component, but this ratio may slightly increase moving inwards the system. The planetary seeds with an initial mass $\sim 1\mathrm{M}_{\oplus}$ are the candidate planetary cores of the future planetary system.

How the rocky planets and the rocky cores of the gaseous giant planets form interacting with the gaseous system is explained by the well known accretion model (Pollack *et al.*, 1996 and see Fig 2.1). However if we consider some giant gaseous planets around solar-type star with semi-major axis $\geq$ 10 AU around the central star, this accretion scenario doesn't clearly explain their formation in a timescale comparable to the life-time of the disk: the *Gravitational Instability*

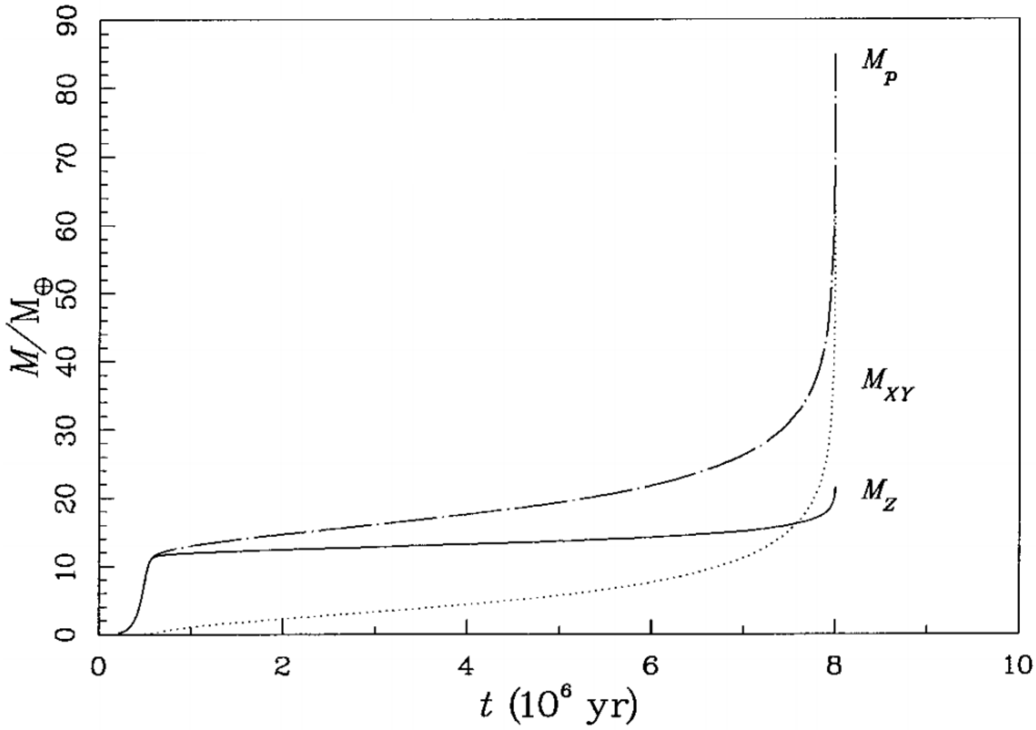

Figure 2.1: The planet's mass accretion as a function of time. The planet is located at 5.2 AU, the initial surface density of the protoplanetary disk is 10 g/cm^2, and planetesimals that dissolve during their journey through the planet's envelope are allowed to sink to the planet's core. The solid line (M_Z) represents accumulated solid mass, the dotted line (M_{XY}) accumulated gas mass, and the dot-dashed line (M_p) the planet's total mass. The planet's growth occurs during the first $\sim 10^5$ years, the planet accumulates solids by rapid runaway accretion and this phase ends when the planet has severely depleted its feeding zone of planetesimals (from Pollack *et al.*, 1996).

scenario may explain a formation in situ of these massive planets in wide orbits. In any case, when the gas depletes and most of the dust has accreted into larger objects, like planets and planetesimals, a planetary system is formed. However, in order to be defined “planet”, this celestial body, according to the International Astronomical Union (IAU), must satisfy the following requirements:

1. To be in orbit around the Sun.

2. To have sufficient mass for its self-gravity to overcome rigid body forces so that it assumes a hydrostatic equilibrium (nearly round) shape.

3. To have cleared the neighbourhood around its orbit.

Hence, following this definition, as shown in the Fig. 2.2, the eight planets of the Solar System are: Mercury, Venus, Earth, Mars, Jupiter, Saturn, Uranus, and Neptune. In this frame, Pluto, which was considered a planet until the IAU 2006 General Assembly, is now defined a “dwarf planet” and recognized as the prototype of a new category of “Trans-Neptunian Objects”.

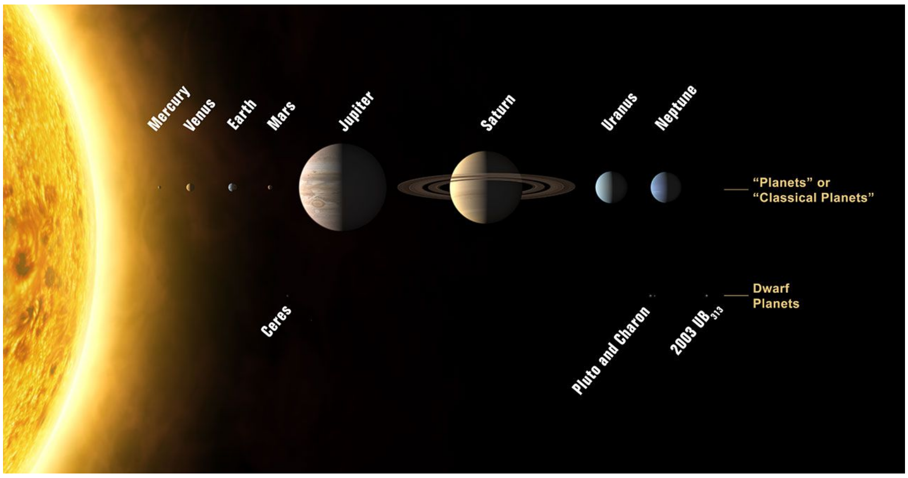

Figure 2.2: The eight planets and the *dwarf planets* of our Solar System according to the results of the IAU 2006 General Assembly (from: https://www.iau.org).

2.1 Protoplanetary disks

The disk is the main substratum where the whole dynamical evolution of the protoplanetary system takes hold; we describe its vertical structure with some geometrical assumptions and approximations like the razor-thin disk (section 2.2) and the flared disk one (section 2.3).
Planets form from protoplanetary disks observed to surround young stars (Haisch *et al.*, 2001). Observationally, most of the star formation occurs in young stellar clusters, where many stars are part of binary or small multiple systems (Duquennoy, 1991). Once disks have formed, the three dominant environmental effects are stellar flybys inside the cluster, close binary companions (if present) and the external radiation produced by other stars in the cluster (especially massive ones that produce strong ultraviolet fluxes and pressure).

At the fist stage of their formation, the protoplanetary disks are composed by non homogeneous structures, such as the molecular clouds. Inside these structures, stars form from dense gaseous cores. Goodman *et al.* (1993), from an observational analysis, estimated the typical ratio between the rotational energy and the gravitational energy in dense cores:

$$\beta = \frac{E_{rot}}{|E_{grav}|} \simeq 0.02 \ ;$$

Later Armitage (2010), in the hypothesis of a uniform density sphere in solid body rotation of a core with a mass 1 $M_\odot$ and a radius of 0.05 pc, for $\beta = 0.02$ estimated an angular momentum:

$$J_{core} \simeq 10^{54} \ g \ cm^2 \ s^{-1} \ ;$$

which exceeding roughly four orders of magnitude the total angular momentum in the Solar System. Understanding how this angular momentum is lost and/or redistributed during, or subsequently, the collapse represents the heart of the "angular momentum problem of star formation". If a solar-mass star forms from such a cloud, the mean specific angular momentum is $l_{core} = J_{core}/M_\odot \simeq 4 \times 10^{20} cm^2 s^{-1}$. The gas with this angular momentum circularizes around the newly formed star at the radius, r_{circ}, where the specific angular momentum of a Keplerian orbit equals that of the core:

$$l_{core} = \sqrt{GM_\odot r_{circ}} \tag{2.1}$$

with the values $r_{circ} \simeq 100AU$. Hence, the formation of disks with sizes comparable to, or larger than, the Solar System is an inevitable consequence of the collapse of molecular cloud cores.
The equilibrium structure of a protoplanetary, self-gravitationally, disk orbiting a star is determined by solving the hydrodynamic equations and the Poisson's equation for the gravitational potential. However no analytic solutions exist, and in order to solve the complex hydrodynamic equations and Poisson's equation for a protoplanetary disks we considered this simplification:

- The vertical thickness of the disk H is a small fraction of the maximum orbital radius $H/r \ll 1$.

The classical structure of a geometrically thin protoplanetary disk follows from considering the vertical force balance at height z above the mid-plane in a disk orbiting at the cylindrical radius r around a star of mass $M_\star$. The vertical component of the gravitational acceleration:

$$g_z = gsin\theta = \frac{GM_\star}{(r^2+z^2)} \frac{z}{(r^2+z^2)^{1/2}} \; ; \tag{2.2}$$

must balance the acceleration due to the vertical pressure gradient in the gas $(1/\rho)(dP/dz)$. If we assume that the disk is *vertically isothermal* (a reasonable hypothesis if the temperature of the gas is set by stellar the radiation) writing the pressure as $P = \rho {c_s}^2$ (with c_s the sound speed) we have:

$$ {c_s}^2 \frac{d\rho}{dz} = -\frac{GM_\star z}{(r^2 + z^2)^{3/2}} \rho \; ; \tag{2.3} $$

with the solution:

$$ \rho = C \exp\left[\frac{GM_\star}{{c_s}^2 (r^2 + z^2)^{1/2}} \right] \; ; \tag{2.4} $$

where the constant of integration C is set by the mid-plane density.
For a thin disk $z \ll r$ and $g_z \simeq \Omega^2 z$, where $\Omega = \sqrt{GM_\star / r^3}$ is the Keplerian angular velocity, thus the vertical density profile has the form:

$$ \rho = \rho_0 e^{-z^2/2H^2}; \tag{2.5} $$

where the mid-plane density ρ_0 can be written in terms of initial total surface density Σ_0 as:

$$ \rho_0 = \frac{1}{\sqrt{2\pi}} \frac{\Sigma_0}{H}; \tag{2.6} $$

and H, the vertical disk scale-height, is given by,

$$ H \equiv \frac{c_s}{\Omega}; \tag{2.7} $$

The corresponding isothermal sound speed is

$$ {c_s}^2 = \frac{k_B T}{\mu m_p}; \tag{2.8} $$

where k_B is the Boltzmann constant and μ is the mean molecular weight in units of the proton mass m_p. As reported by Armitage (2010), considering a molecular gas of cosmic composition with $\mu = 2.3$, $c_s \simeq 0.6 kms^{-1}$, at 1 AU around a solar-mass star, the ratio H/r is $\simeq 0.02$, implying that the condition of a disk geometrically thin is adequately satisfied.

2.1.1 Razor-thin disk

The temperature profile and spectral energy distribution of a protoplanetary disk are essentially determined by the shape of the disk (flat, flared, or warped) and by thermal mechanism of absorption and emission of the radiation. The simplest model of protoplanetary disk is the flat razor-thin disk that absorbs all incident stellar radiation and re-emits it locally as a black-body. We consider a surface coplanar to the plane of the disk at distance r from a star of radius $R_\star$. The star is assumed to be a sphere of constant surface brightness $I_\star$. Setting up spherical polar coordinates such that the axis of the coordinate system points to the center of the star (see Fig.2.3), the stellar flux, passing through this surface, is:

$$F = \int I_\star \, sin\theta \; cos\phi \; d\Omega; \tag{2.9}$$

where $d\Omega$ represents the element of solid angle. We count the flux coming from the top half of the star only (and to be consistent equate that to radiation from only the top surface of the disk), so the limits on the integral are

$$-\frac{\pi}{2} < \phi \leq \frac{\pi}{2}$$

$$0 < \theta < sin^{-1}\Big(\frac{R_\star}{r}\Big);$$

which gives

$$F = I_\star \Big[sin^{-1}\Big(\frac{R_\star}{r}\Big) - \Big(\frac{R_\star}{r}\Big)\sqrt{1 - \Big(\frac{R_\star}{r}\Big)^2} \Big]; \tag{2.10}$$

For a star with effective temperature $T_\star$, the brightness is $I_\star = (1/\pi)\sigma T_\star^4$, with σ the Stefan-Boltzmann constant. Equating the 2.10 to the disk emission, σT_{disk}^4, we obtain a radial temperature profile:

$$\Big(\frac{T_{disk}}{T_\star}\Big)^2 = \frac{1}{\pi}\Big[sin^{-1}\Big(\frac{R_\star}{r}\Big) - \Big(\frac{R_\star}{r}\Big)\sqrt{1 - \Big(\frac{R_\star}{r}\Big)^2} \Big]; \tag{2.11}$$

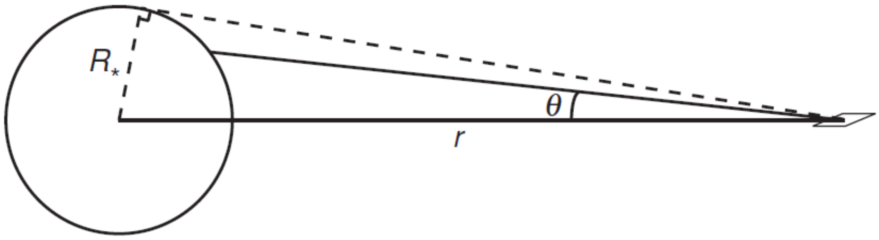

Figure 2.3: Geometry for calculation of the radial temperature profile of a razor-thin protoplanetary disk (from Armitage, 2010).

Integrating over radii, the total disk luminosity is:

$$L_{disk} = \frac{1}{4} L_\star; \tag{2.12}$$

Therefore, a flat disk intercepts a quarter of the stellar flux.

Expanding the right side of 2.11 in Taylor series in the limit that $\frac{R_\star}{r} \ll 1$ (i.e. far from the star) the temperature profile is:

$$T_{disk} \propto r^{-3/4};$$

as the limiting temperature profile of a thin, flat disk.

Moreover, assuming vertical isothermality, the ratio $\frac{H}{r}$ is

$$\frac{H}{r} \propto r^{1/8};$$

predicting a modest flaring at large radii.

2.1.2 Flared disk

The next step to describe a protoplanetary disk closer to a real protoplanetary disk, is to consider a flared disk. The disk is described as flared if at the cylindrical distance r from the star, it absorbs stellar radiation at a height H_p above the mid-plane and if the ratio H_p/r is an increasing function of radius. Features of flared disks are, first, that all points on the surface of the disk have a clear line of sight to the star and, second, the disk subtends a greater solid angle than a razor-thin disk. In this way, flared disks absorb a greater fraction of the stellar radiation than flat disks, and thus produce a stronger IR excess. The temperature profile of a flared disk can be computed in the same way of the razor-thin disk, integrating over the part of the stellar surface visible from the disk surface at radius r (Kenyon & Hartmann, 1987).

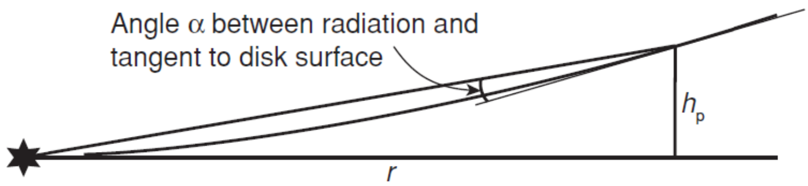

Figure 2.4: Geometry for the calculation of the radial temperature profile of a flared protoplanetary disk. At the distance r $\gg$ R$_\star$ radiation from the star is absorbed by the disk at height h_p above the mid-plane. The angle between the tangent to the disk surface and radiation is α (from Armitage P., 2010)

Adopting the approximation $r \gg R_\star$, the star can be considered a point source of radiation. At the cylindrical distance r, the stellar radiation is absorbed by the disk at height H_p above the mid-plane. Note that H_p is not the same as the disk scale-height H, since the absorption of stellar radiation depends not just on the density but also on the opacity of the disk. From consideration of the geometry (see Fig. 2.4), the angle between the incident radiation and the local disk surface is given by:

$$\alpha = \frac{dH_p}{dr} - \frac{H_p}{r} \tag{2.13}$$

The rate of heating per unit disk area at distance r is:

$$Q_{+} = 2\alpha\Big(\frac{L_\star}{4\pi r^2};\Big) \tag{2.14}$$

Equating the heating rate to the rate of cooling by black-body radiation,

$$Q_{-} = 2\sigma T_{disk}^4 \tag{2.15}$$

the temperature profile becomes:

$$T_{disk} = \Big(\frac{L}{4\pi\sigma}\Big)^{1/4}\alpha^{1/4}r^{-1/2} \tag{2.16}$$

Since $L_\star = 4\pi R_\star^2\sigma T_\star^4$, an equivalent expression is:

$$\frac{T_{disk}}{T_\star} = \Big(\frac{R_\star}{r}\Big)^{1/2}\alpha^{1/4} \tag{2.17}$$

Assuming a relation between H and H_p, it may be plausible if the disk is very optically thick, Kenyon & Hartmann (1987), at large radii, find that the surface temperature is:

$$T_{disk}(r) \propto r^{-1/2};$$

which is flatter than the $T_{disk} \propto r^{-3/4}$ profile of a flat disk.

The formalism of the flared disk and its dynamical viscous evolution will be numerically studied in the Chapter 5.1 and simulated in our theoretical investigation in the Chapter 5.2.

2.2 Planetary systems

A planetary system is a set of gravitationally bound non-stellar objects around a single (or multiple) stellar type object. We consider the transition from the phase of protoplanetary to planetary system when the gas is mostly depleted and the dust, mostly dragged by the dynamics of the gas , is accreted into larger objects like planetary cores and planetesimals. The first and well known planetary system is, of course, our Solar System. It is composed by eight planets where the four smaller inner planets, called terrestrial, are Mercury, Venus, Earth and Mars, being primarily composed of rock and metal. The four outer planets are giant planets, being substantially more massive than the terrestrials. The two largest, Jupiter and Saturn, are gas giants, composed mainly of hydrogen and helium; the two outermost planets, Uranus and Neptune, are ice giants, being composed mostly of substances with relatively high melting points compared with hydrogen and helium, such as water, ammonia and methane. All eight planets have almost circular orbits that lie within a nearly flat disk called the ecliptic. However our planetary system is not the only one: beyond our Solar System, the tally of known extrasolar planets stands at 4118 (exoplanet.eu) with nearly 2498 more candidates waiting to be confirmed. The present number of exoplanetary systems, composed by at least two planets, is 877. The most part of these systems are discovered through "dynamical signatures", which signal the presence of a companion by the orbital motion of the host stars among the barycenter of the star-planet system (variation in radial velocities) and information coming from the direct measurement of the light of the star-planet system (transits). The motion of a single planet in a circular orbit around a star causes the star to undergo a reflex circular motion around the star-planet barycentre, with orbital semi-major axis $a_\star = a(M_p/M_\star)$ and period P. This results in the periodic perturbation of the stellar spectrophotometric information, which are detected in radial velocity and in time of arrival of some periodic reference signal.

Variation in radial velocities The velocity amplitude K of a star of mass $M_\star$ due to a companion with mass M_p sin$i$ with orbital period P and eccentricity e is (e.g. Cumming *et al.* (1999)):

$$K = \left(\frac{2\pi G}{P}\right)^{1/3} \frac{M_p sin(i)}{(M_p + M_\star)^{2/3}} \frac{1}{(1-e^2)^{1/2}} \tag{2.18}$$

In a circular orbit the velocity variations are sinusoidal, and for $M_p \ll M_\star$ the amplitude reduces to:

$$K = 28.84 \left(\frac{P}{1\ year}\right)^{-1/3} M_p\ sin(i) \left(\frac{M_\star}{M_\odot}\right)^{-2/3} m\ s^{-1} \tag{2.19}$$

where P and a are related by Kepler's Third Law:

$$P = \left(\frac{a}{1\ AU}\right)^{3/2} \left(\frac{M_\star}{M_\odot}\right)^{-1/2} year \tag{2.20}$$

The semi-amplitude of this radial velocity curve is about $K = 12.5$ m s^{-1} with a period of 11.9 yr in the case of Jupiter orbiting the Sun, and about 0.1 m s^{-1} for the Earth. The sin$i$ dependence means that orbital systems seen face on ($i = 0$ if seen by an observer on the ecliptic) result in no measurable radial velocity perturbation and that, conversely, radial velocity measurements can determine only M_p sin$i$ rather than M_p , and hence provide only a lower limit to the planet mass since the orbital inclination is generally unknown. Although the radial velocity amplitude is independent of the distance to the star, signal-to-noise considerations limit observations to the brighter stars. Equation 2.18 indicates that radial velocity measurements favour the detection of systems with massive planets, and with small a (and hence small P).

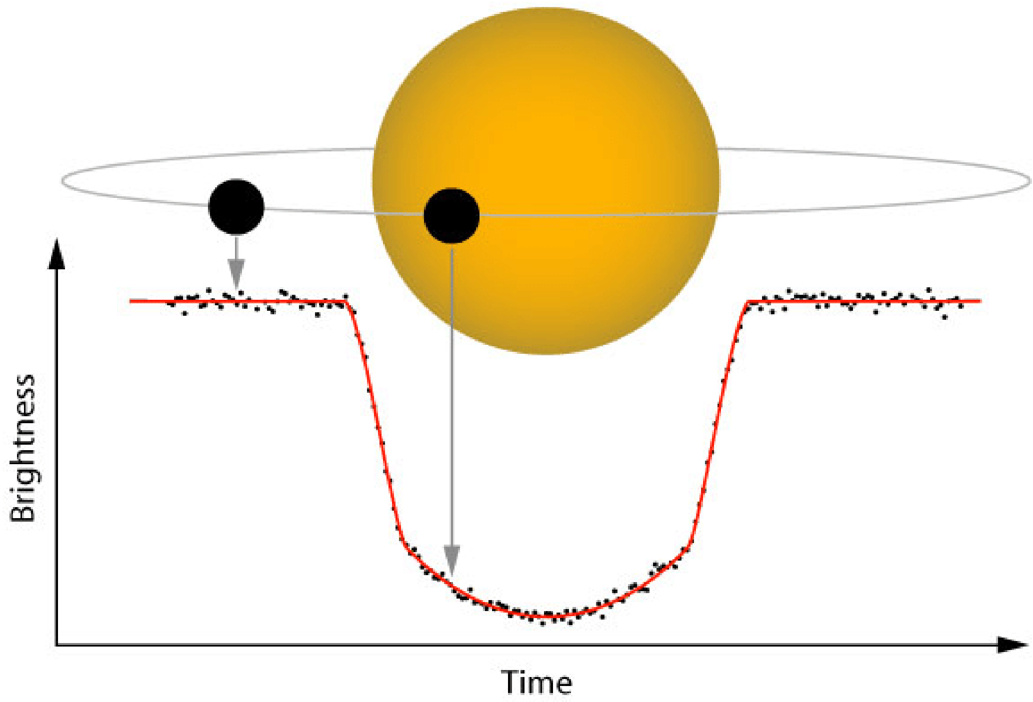

Figure 2.5: A light curve, showing the transit method of detecting exoplanets. This method of detection involves monitoring the brightness of stars to identify periodic drops caused by planets crossing in front and blocking a fraction of their light (Image credit: NASA).

Transit depth and probability The transit method aims at detecting the dimming of the stellar light by occultation due to an orbiting planet (see Fig 2.5). Transit experiments offer a relatively easy way to investigate the planet atmosphere, doing spectroscopy during the planet transit. Massive planets with short orbits, called Hot Jupiters (see Fig. 2.6) can be observed from the ground, while planets down to Earth-mass or below can be detected from space. The probability of viewing a planet to transit over the stellar disk at the right angle, depends on the ratio between the stellar radius, $R_{\star}$, and the planetary semi-major axis a. The transit amplitude depends primarily on the relative radii of the planets and stellar disk.

$$\frac{\Delta L}{L_\star} \simeq \left(\frac{R_p}{R_\star}\right)^2 \tag{2.21}$$

If the radius of the star can be estimated from spectral classification, then R_p can be estimated from equation 2.21. With knowledge of P and an estimate of $M_\star$ (also from spectral classification or via evolutionary models), the semi major axis of the orbit, a, can be derived from Kepler's law. Usually transiting planet orbit have very low eccentricities. With the approximation of circular orbit, other observational parameters are given, to first order, by simple geometry (Deeg (1998)). Thus the duration of the transit is:

$$\tau = \frac{P}{\pi}\left(\frac{R_\star cos\delta + R_p}{a}\right) \simeq 13\left(\frac{M_\star}{M_\odot}\right)^{-1/2}\left(\frac{1}{1AU}\right)^{1/2}\left(\frac{R_\star}{R_\odot}\right) hours \tag{2.22}$$

where δ is the latitude of the transit on the stellar disk. With the other parameters estimated as above, δ can be derived from equation 2.22, and hence the orbital inclination from $cos(i) = (R_\star sin\delta)/a$. The minimum inclination where transits can occur is given by $i_{min} = cos^{-1}(R_\star/a)$, with the probability of observing transits for a randomly oriented system of $p = R_\star/a = cosi_{min}$. Evaluation of i and p for realistic cases demonstrates that i must be very close to 90° , while p is very small, implying that only a small fraction of planets can ever be detected or monitored using this technique.

Unfortunately these techniques are focused on the inner ($\leq$ 5AU) region of a planetary system: they are in fact biased towards planets in relatively close orbits and so the orbital separations larger than $\sim$ 5AU are currently not well sampled. Direct imaging surveys, which are typically more sensitive to planets at larger orbital separations, can fill this gap. However a direct detection of exoplanets is technically challenging due to the small angular separation of a very faint source (the planet) from a much brighter one (the host star) and it requires extraordinary efforts in order to overcome the barriers imposed by astrophysics (planet-star contrast), physics (diffraction), and engineering (scattering).

Planetesimal interactions Coming back to the structure of the planetary systems, after the depletion of the disk, we found several populations of small bodies with very different orbital structures and complex dynamics. In our Solar System, we have the asteroid belt, the Kuiper belt and the Trojans asteroids of Jupiter and Neptune; As reported in Davies *et al.* (2014), these populations show “excited” eccentricities and inclinations, contrary to that the planetesimal disks should have quasi-circular, coplanar orbits as expected from a formation in a proto-planetary disk. This kind of anomalies are a dynamical footprint suggesting a potential strong perturbation, such as close encounters with a passing-by massive object or resonant interactions with planets, some of which are possibly no longer belonging to the system. The interaction between planets and planetesimals can be neglected as long as there is a lot of gas in the system, but it becomes predominant once the gas-disk is substantially depleted (Capobianco *et al.* 2011). A single planet embedded in a pure planetesimal disk typically migrates inwards, improving the scattering of planetesimals in the outwards direction (Kirsh *et al.* 2009). However, two (or more) planets on nearby orbits typically migrate in divergent directions, the outer planet(s) moving outwards and the inner one inwards, because the outer planet acts as a conveyor belt, transferring planetesimals from the outer disk to the inner planet (Fernandez and Ip, 198a). If the planetesimal disk is far enough that the planets cannot scatter them, the secular planet-planetesimal interactions can still modify the resonant orbits of the planets and enhance their eccentricities until a global instability follows (Levison *et al.* 2011). In this frame the planetesimals still play a fundamental role: by exerting dynamical friction on the planets, they eventually damp the planetary eccentricities and inclinations,

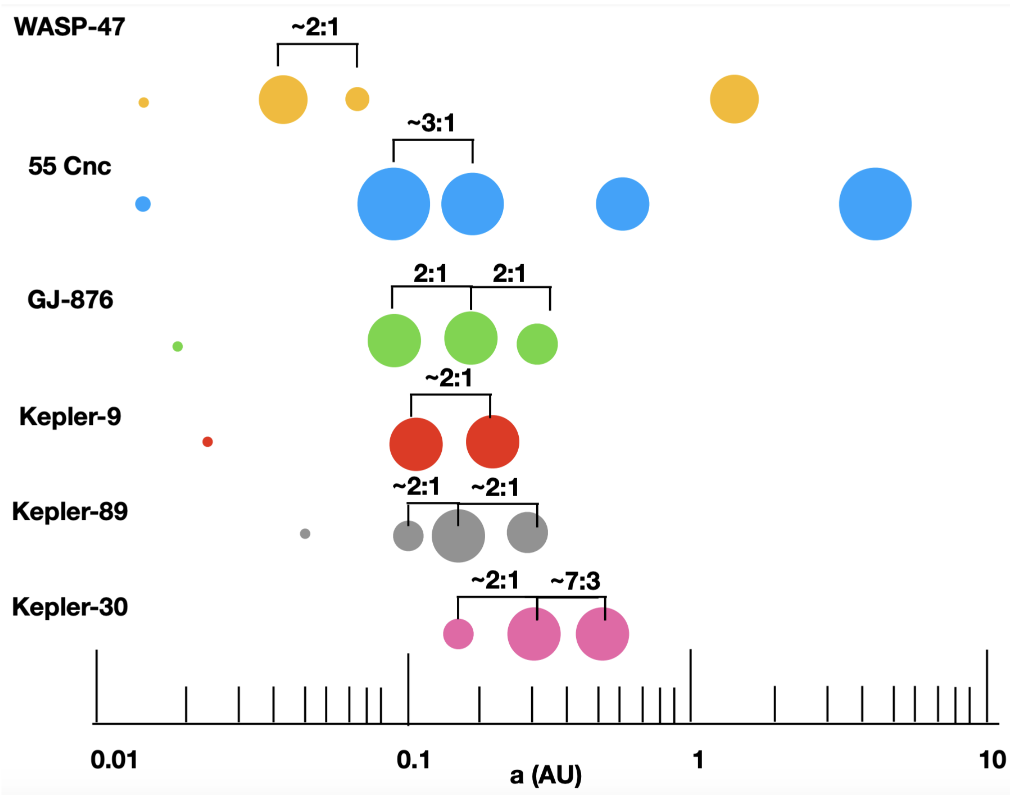

Figure 2.6: Warm and Hot Jupiters for which the companions have semi-major axes less than 1 AU. Orbital resonances are labeled and sizes scale approximately with log planet mass. Hot Jupiter WASP-47b (Becker *et al.* 2015) may be in the short period tail of a class of system featuring a close-in giant planet in orbital resonance with one or more neighbors. This architecture often also includes an ultra-short period super-Earth (Dawson & Johnson, 2018).

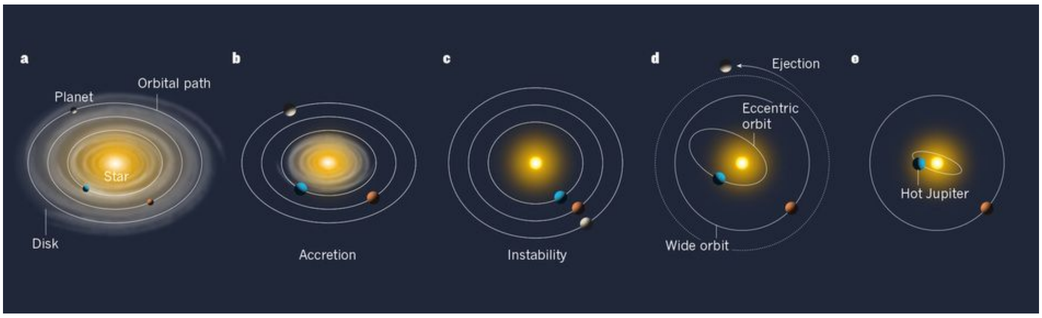

Figure 2.7: Brucalassi *et al.* show that the "hot Jupiters" may form from interactions with other celestial bodies. In (a), two or more planets form within a protoplanetary disk around a young star. In (b), the disk material accretes onto the star, but also onto the planets, whose masses become similar to that of Jupiter. In (c), at some point, a dynamical instability occurs, either as an inherent, unstable planetary configuration or as a result of a massive passing by star. In (d), one of the planets moves to a highly eccentric orbit, whereas the others either adopt wide orbits or are ejected. Finally in (e), when the eccentrically orbiting planet passes close to the star, tidal forces cause its orbit to shrink and become more circular. The final result is a large gaseous planet with a short orbital period (from Triaud, 2016).

allowing the planets to recover a stable configuration with moderately excited orbits (Tsiganis *et al.* 2005; Morbidelli *et al.* 2007; Nesvorny & Morbidelli, 2012). In this process the planetesimals are violently dispersed and only those landing in stable niches of the orbital space survive. Thus, reproducing the current orbital structure of the surviving planetesimal populations is a crucial diagnostic of an instability model, possibly more than the final orbits of the planets themselves.

Chapter 3

Dynamical evolution of planetary systems

Very likely, many of detected exoplanetary systems did not form in their present planetary configuration, but, rather, their dynamical evolution forged their current architecture. Processes like planet migration, resonant trapping, planet-planet scattering and interactions with a stellar environment have thus shaped the structure of the planetary systems since the formation of the planets. Empirically, the detection of many short-period giant planets(the “hot Jupiters”), such as 51 Peg b (Mayor & Queloz, 1995) or V830 Tauri b (Donati *et al.*, 2016) shows how the dynamical evolution may indeed affect the orbital configuration of a giant planet (see Fig. 2.7).

When the planetary systems are still in the protoplanetary phase, low-mass planets (Earth-mass protoplanets) totally embedded in gaseous disks, would undergo rapid inward migration (type I migration), reaching the central star within $\sim 10^5$ yr. Moreover we know that giant planets form gaps in their disks, and migrate inward on their viscous evolution times (typically 10^5 yr) (Lin & Papaloizou, 1986). Planetary migrations in a low-mass disk ($\sim 1/100$ the mass of the central star) can be divided into two types:

- Type I: migration of low-mass embedded planets
- Type II: migration and gap formation by massive planets

Further evidences for planetary migration are from observations of giant planets in mean motion resonance, such as the two giant planets orbiting the M-type star GJ 876 (Marcy *et al.* 2001), or the two Saturn mass planets in the Kepler-9 system (Holman *et al.* 2010). Recent discoveries of resonant or near-resonant multiple systems of transiting planets by the Kepler mission, such as the Kepler-11 system (Lissauer *et al.* 2011), point to an origin in a highly flattened and dissipative environment.

3.1 Low-mass embedded planets

We define *low-mass embedded planets* the proto-planets or the planetary seeds that induce only small perturbations in the disk such that the angular momentum exchange between disk and planet can be determined from a linear analysis of the perturbed flow. The unperturbed disk is assumed to be axisymmetric and in a state of Keplerian rotation with angular velocity $\Omega(r) = \sqrt{GM\star/r^3}$ around the star, and the planet, with angular velocity $\Omega_p \equiv \Omega(r_p)$, is on a circular orbit with radius r$_p$. As reported in Kley & Nelson (2012), neglecting in first approximation the pressure of the gaseous disk, resonances occur when:

$$m(\Omega(r) - \Omega_p) = 0 \tag{3.1}$$

$$m(\Omega(r) - \Omega_p) = \pm\kappa(r) \tag{3.2}$$

where:

- $\kappa(r)$ is the epicyclic frequency in the disk, that is the oscillation frequency for a particle in the disk subject to a small radial displacement.
- m is the azimuthal mode number of each coefficient of the gravitational potential expressed in Fourier series.

The first case refers to the corotation resonance where the local disk and planet orbital speeds are equal, $\Omega(r) = \Omega_p$. The second resonance condition applies to Lindblad resonances where the plus sign, $\Omega(r) = \Omega_p + \kappa(r)/m$, refers to inner Lindblad resonances (interior to r$_p$), where the disk rotates faster than the planet. The minus sign refers to the outer Lindblad resonances, $\Omega = m(\Omega(r) = \Omega_p - \kappa(r)/m$ (exterior to r$_p$ and the corotation region). The radial locations of the Lindblad resonances, r$_L$, are obtained by the condition of a Keplerian disks, $\kappa = \Omega$, which leads to

$$r_L = \left(\frac{m}{m \pm 1}\right)^{(2/3)} r_p; \tag{3.3}$$

Where pressure in a disk can not be neglected, the modified Lindblad resonance condition is:

$$m(\Omega(r) - \Omega_p) = \sqrt{\kappa^2(r)(1+\xi^2)} \tag{3.4}$$

where $\xi^2 = mc_s/\Omega(r)$ and c$_s$ is the isothermal sound speed in the disk. To the limit $m \to \infty$, and $c_s = H\Omega(r)$ where H is the local disk scale height, the Lindblad resonance positions are:

$$r_L = r_p + \frac{2H}{3}, \tag{3.5}$$

showing that the Lindblad resonances, for $m \gg 1$, accumulate at a distance equal to $2H/3$ from the planet. This mechanism prevents the divergence of the planetary torque experienced by the planet from the disk, giving rise to the phenomenon known as the *torque cut-off* (Goldreich & Tremaine, 1980).

3.1.1 Type I planetary migration

Considering low-mass planets, the combined effect of Lindblad and corotation torques can be calculated using the previous linear analysis. Due to the complexity of considering heat generation and transport in disks, these linear studies consider an isothermal disk model, where the disk has a fixed radial temperature structure, $T(r)$. The temperature varies radially but it is constant in the vertical direction. Linear calculations have been performed for 2D (flat disks) and full 3D configurations. Comprehensive 3D linear calculations have been presented by Tanaka, Takeuchi & Ward (2002), and for a vertically isothermal disk, they yield the following expressions for the Lindblad and corotation torques acting on the planet:

$$\Gamma^{L}_{lin} = -(2.34 - 0.1\beta_{\Sigma})\Gamma_0 \tag{3.6}$$

$$\Gamma^{C}_{lin} = 0.64(\frac{3}{2} - \beta_{\Sigma})\Gamma_0 \tag{3.7}$$

where the surface density profile varies with radius on the disk plane as $\Sigma(r) \propto r^{\beta_{\Sigma}}$ and the torque normalization Γ_0 is given by:

$$\Gamma_0 = \left(\frac{m_p}{M_{\star}}\right)^2 \left(\frac{H}{r_p}\right)^{-2} \Sigma_p r_p^4 \Omega_p^2 \tag{3.8}$$

which it depends on planet location (as indicated by the index p). The total torque, Γ^{tot}_{lin}, is given as the sum of the Lindblad and corotation torques (Ward, 1986):

$$\Gamma^{tot}_{lin} = \Gamma^{L}_{lin} + \Gamma^{C}_{lin} \tag{3.9}$$

The magnitude of the type I torque scales as the inverse square of the disk aspect ratio (H/r_p), quadratically with the planetary mass m_p and linearly with the surface density of the disk. In recent years, the linear studies are replaced by many numerical studies in 2D and 3D. The disk is modeled as a viscous gas and the full nonlinear Navier-Stokes equations are solved, typically using grid-based hydrodynamic codes. Moreover, numerical improvements have led to increased computational efficiency and accuracy that allow longer and higher resolution simulations to be performed. Worthy of mention are the FARGO method (Masset, 2000), which overcomes restrictions on the time-step due to the differentially rotating disk, and a conservative treatment of the Coriolis force (Kley, 1998). To increase spatial resolution around the planet, nested-grid structures have been employed successfully in 2D (D'Angelo, Henning & Kley, 2002) and 3D (D'Angelo, Kley & Henning, 2003). The 3D simulations gave a good agreement with the 3D linear results, considering the influence of radial temperature gradients in the disk, such that $T(r) = T_0\, r^{-\beta_T}$. Moreover, D'Angelo & Ludow (2010) calculations yield the following form for the total (Lindblad and corotation) torque acting on planets with masses below about 10 $M_\oplus$:

$$\Gamma_{tot} = -(1.36 + 0.62\beta_\Sigma + 0.43\beta_T)\Gamma_0 \tag{3.10}$$

where β_Σ is the exponent of the surface density radial profile $\Sigma(r)$, and β_T is the exponent of the temperature radial profile $T(r)$. The torques, acting on the planet, change its angular momentum J_p according to:

$$\frac{dJ_p}{dt} = \Gamma_{tot} \tag{3.11}$$

For circular orbits, the angular momentum J_p depends only on the planet's distance a_p (semi-major axis) from the star:

$$J_p = m_p\sqrt{GM_\star a_p} \tag{3.12}$$

Introducing the planetary migration rate $\dot{a}_p$, the migration timescale is:

$$\tau_{mig} = \frac{a_p}{\dot{a}_p} = \frac{1}{2}\frac{J_p}{\Gamma_{tot}} \tag{3.13}$$

As reported by Kley & Nelson (2012), for an Earth-mass planet around a solar-mass star, at 1 AU, embedded in the Minimum Mass Solar Nebula ($\Sigma = 1700\, g\, cm^{-3}$, $H/r = 0.05$), they found $\tau_{mig} \approx 10^5$yr. However, in the well known theoretical investigation of Pollack *et al.* (1996) for the planetary formation, planetary cores of a few Earth-masses, initially located at 5 AU, migrate in a timescale shorter than the gas accretion time onto the core, which is typically few Myr. These considerations point up a serious bottleneck in the timescales of the planetary formation and migration, stimulating potential suggestions to solve this excessively rapid type I migration:

- Strong corotation torques operating in regions where there are steep positive surface density gradients ("planet-traps") (Masset *et al.* 2006)

- Reductions in the differential Lindblad torque in regions of sharp opacity transition (Menou & Goodman, 2004)

- Magnetic resonances in disks with strong toroidal magnetic fields (Terquem, 2003)

- Torque reversals for planets on eccentric orbits (Cresswell & Nelson, 2006)

- Torque reductions from disk shadowing and illumination variations in the presence of a planet (Jang-Condell & Sasselov, 2005)

- Stochastic migration induced by disk turbulence (Laughlin, Steinacker & Adams, 2004)

- Corotation torques in radiative disks (Paardekooper & Mellema, 2006)

3.2 Massive embedded planets

We define *massive planet* a bound object to central star, embedded in the disk, with a mass dynamically able to change significantly the disk's original structure. When the planetary mass increases, the strength of the gravitational interaction and the corresponding angular momentum transfer to the disk become stronger. Moreover this kind of interaction becomes increasingly non-linear and more observables of the disk like the density profile are modified. As described in Kley & Nelson (2012), if the angular momentum can be deposited locally in the disk and is not carried away by the spiral waves, which may occur through viscous dissipation or shock waves, the material inside (outside) the planet loses (gains) angular momentum and recedes from the planet. Consequently, the material appears to be *pushed* away from the location of the planet and a gap begins to open in the disk. The depth and width of the gap that the growing planet carves out will depend on the disk physics (viscosity and pressure), and on the mass of the planet. The planet's transfer of angular momentum to the disk can be obtained by summing over the Lindblad resonances (Goldreich & Tremaine, 1980) or by using the impulse approximation, where one considers the momentum change between a planet and individual disk particles shearing past (Lin & Papaloizou, 1979), however both approaches yield similar results. Lin & Papaloizou (1986) give the following expression for the rate of angular momentum transfer from the planet to the disk:

$$\dot{J}_{tid} \;\propto\; q^2 \Sigma_p \, a_p^2 \, \Omega_p^2 \left(\frac{a_p}{\Delta}\right)^3 \tag{3.14}$$

where quantities with index p are evaluated at the planet's position, q is the mass ratio $\mathrm{m}_p/\mathrm{M}_\star$ and $\Delta = |a_p - r|$ is the impact parameter between the fluid particle's unperturbed trajectory and the planet. The viscosity damps the rate of angular momentum transfer and tries to close the gap; therefore the corresponding viscous torque is (Lynden-Bell & Pringle, 1974):

$$\dot{J}_{visc} = 3\pi\Sigma_p \nu a_p^2 \Omega_p \tag{3.15}$$

where ν is the vertically integrated kinematic viscosity. Gap formation implies that the effect of gravity (the tidal torque) overwhelms that of viscosity:

$$\dot{J}_{tid} \geq \dot{J}_{visc} \tag{3.16}$$

The gap should have a minimum width at least equal to the size of the planet's Hill sphere (i.e. $\Delta \approx R_H$), this being R$_H$ $= (q/3)^{(1/3)} a_p$. The viscous criterion for a gap formation is then given by (Lin & Papaloizou, 1993):

$$q \geq \frac{40\nu}{a_p^2 \Omega_p} \tag{3.17}$$

For the disk response to be non-linear near the planet, so that the spiral waves form shocks and deposit their angular momentum flux locally in the disk, we require that the planet's Hill sphere size exceeds the disk thickness, leading to the thermal gap opening criterion, R$_H$ $\geq H$ (Ward, 1997). When the planet's Hill sphere size exceeds the disk thickness, R$_H$ $\geq H$, spiral waves form shocks and deposit their angular momentum flux locally in the disk creating the *thermal gap* (Ward, 1997). Crida, Morbidelli & Masset (2006) investigated the combined action of viscosity and pressure suggesting the following criterion for the formation of a gap:

$$\frac{3}{4}\frac{H}{R_H} + \frac{50\nu}{q a_p^2 \Omega_p} \leq 1; \tag{3.18}$$

As reported in Kley & Nelson (2012), for solar nebula-type conditions, a Saturn mass planet begins to open visible gaps in the disk, but it should be kept in mind that gap formation is a continuous process. The process of gap formation has been analyzed analytically and numerically by a number of researchers (Takeuchi, Miyama & Lin, 1996; Bryden *et al.* 1999; Kley, 1999).

3.2.1 Type II planetary migration

When a massive planet is formed, it opens a gap in disk, so the Lindblad torques are reduced, resulting in a slowing down of the planet migration. In this case, the planet is coupled to the viscous evolution of the disk (Lin & Papaloizou, 1986) and the migration timescale is given by the viscous diffusion time of the disk, $\tau_{visc} \propto r_p^2/\nu$. This non-linear regime of disk-planet interaction in which gap opening planets are locked to the viscous evolution is known as type II migration (Ward, 1997). Using the previous descriptions for the tidal and viscous torque Lin & Papaloizou (1986) modeled the migration of a gap opening massive planet simultaneously with the viscous disk evolution utilizing the time dependent diffusion equation for the disk surface density, $\Sigma(r,t)$, (Pringle, 1981). Later, fully 2D hydrodynamical simulations of moving and accreting planets were performed by Nelson *et al.* (2000), who showed that a Jupiter-mass planet starting from ~ 5 AU migrates, on a timescale $\sim 10^5$ yrs, inwards to the planetary system. In this planetary migration, the planet accreates its mass until to $4-5$ M$_{Jup}$ and its inertia starts to be important: it *resists* the viscous driving, following a further reduction in the speed of migration (Syer & Clarke, 1995; Ivanov, Papaloizou & Polnarev, 1999). These studies on Type II planetary migration might indicate a possible scenario to justify the observed population of hot Jupiters (Lin, Bodenheimer & Richardson, 1996; Armitage *et al.* 2002); however, the presence of additional massive planets in these systems can lead to quite different dynamical evolution considering gravitational interactions and scattering processes between the planets. Finally, a potential contribution to a Type II planetary migrations is suspected from exogenous gravitational perturbations when the planetary system forms and evolves in a young stellar cluster. These gravitational perturbations affect the planetary migration reducing the timescale and, depending on the mass and the orbital parameters of the stellar perturber, change significantly the orbital architecture of the planetary system.

3.3 Dynamical evolution of planetary systems in stellar clusters

In this section we introduce the dynamical interaction between the members of young stellar clusters with the consequent effects on the dynamical evolution of a young and forming planetary systems. Most stars form within some type of cluster or association. About 10% of the stellar population is born within clusters that are sufficiently robust to become open clusters, which live for 100 Myr to 1 Gyr. The remaining 90% of the stellar population is born within shorter-lived cluster systems called embedded clusters. Embedded clusters become unbound and fall apart when residual gas is ejected through the effects of stellar winds and/or supernovae. This dispersal occurs on a timescale of $\sim$ 10 Myr. As reported in Davies *et al.* (2014), considering the cluster distribution function f$_{cl} \sim 1/N^2$ over a range from N = 1 (single stars) to N= 10^6, the probability that a star is born within a cluster of size N scales as $P = Nf_{cl} \sim 1/N$, so that the cumulative probability scales as $logN$. Hence, stars are equally likely to be born within clusters in each decade of stellar membership size N. Clusters have typical radii of order $R = 1pc$, and the cluster radius scales as $R \approx 1pc(N/300)^{1/2}$, so that the clusters have (approximately) constant column density (Lada and Lada 2003; Adams *et al.*, 2006). A typical mean density is ~ 100 stars/pc^3 and a typical velocity dispersion is $\sim$ 1km/s. Dynamical interactions within clusters are the close encounters. A close encounters becomes important when the orbit of the first passing by star is significantly affected by the gravitational interaction of the second star. As reported in Davies *et al.* (2014), for a typical velocity dispersion of 1 km/s, and for solar-type stars, this critical distance is about 1000 AU.

Timescale of a stellar flyby The timescale of a close encounter with another star within a distance r$_{min}$ can be approximated by (Binney and Tremaine 1987):

$$\tau_{enc} \simeq 3.3 \times 10^7 yr \left(\frac{100\ pc^{-3}}{n}\right)\left(\frac{v_\infty}{1km/s}\right)\left(\frac{10^3 AU}{r_{min}}\right)\left(\frac{M_\odot}{M}\right) \tag{3.19}$$

Here n is the stellar number density in the cluster, v_∞ is the mean relative speed at infinity of the stars in the cluster, r$_{min}$ is the encounter distance, and M is the total mass of the stars involved in the encounter. Planetary systems are affected by passing stars and binaries in a variety of ways (e.g., Laughlin and Adams 1998; Adams and Laughlin 2001; Bonnell *et al.* 2001; Davies and Sigurdsson 2001; Adams *et al.* 2006; Malmberg *et al.* 2007b; Malmberg and Davies 2009; Spurzem *et al.* 2009; Malmberg *et al.* 2011; Hao *et al.* 2013).

Number of stellar flybys Another way to estimate the characteristic time τ_{enc} on which an encounter occurs is considering the mean-free-path of a star inside the cluster (Jiménez-Torres *et al.*, 2013). The mean-free-path is $\lambda = \frac{\sigma}{n}$, where n is the stellar density per number and σ the cross section $\sigma = \pi(2R)^2$ with R the radius of the circumstellar structure. Dividing λ by the velocity dispersion v of the cluster, we obtain the characteristic time τ_{enc}. Dividing τ_{enc} by the age of the stellar cluster T_e, the number of encounters is given by:

$$N_{enc} = 4\pi\ n\ vT_e\ R^2 \tag{3.20}$$

Jiménez-Torres *et al.* (2013) calculated the effect of stellar encounters in different Galactic environments on a 100 AU planetary disk. They present in Figure 3.1 a log-log plot of density versus velocity dispersion and they show with level curves the number of encounters for a given combination of these two parameters in different Galactic environments. The Galactic environments are marked with elliptical regions approximately where they correspond according to their physical characteristics. Straight lines represent the number of encounters 3.20, given a density and velocity dispersion for a total integration time T_e of 5 Gyr. The green shadow covers the Galactic regions that sustained in their history less than one stellar encounter. They consider these regions potentially habitable from the stellar encounter dynamics point of view.

Planetary ejection An individual sufficiently close encounter can eject planets. The cross section for a planet ejection can be written in the form (from Adams *et al.* 2006):

$$\Sigma_{ej} \simeq 1350\;(AU)^2 \left(\frac{M_\star}{1M_\odot}\right)^{-1/2} \left(\frac{a_p}{1\;AU}\right) \tag{3.21}$$

where $M_\star$ is the mass of the planet hosting star and a_p is the initial semi-major axis of the planet.

However another class of encounters leads to indirect ejection as well: the flyby event perturbs the orbits of planets in a multiple planet system, and planetary interactions later lead to the ejection of a planet (see Fig. 3.2) . Typical instability timescales are in the range $1 - 100$ Myr. Similarly, the ejection of the Earth from our Solar System is more likely to occur indirectly through previous perturbations of Jupiter's orbit, rather than via direct ejection from a passing star (Laughlin & Adams, 2000). Planetary systems residing in wide stellar binaries in the field of the Galaxy are also vulnerable to external perturbations. Passing stars and the Galactic tidal field can change the stellar orbits of wide binaries, making them eccentric, leading to strong interactions with planetary systems (Kaib *et al.* 2013).

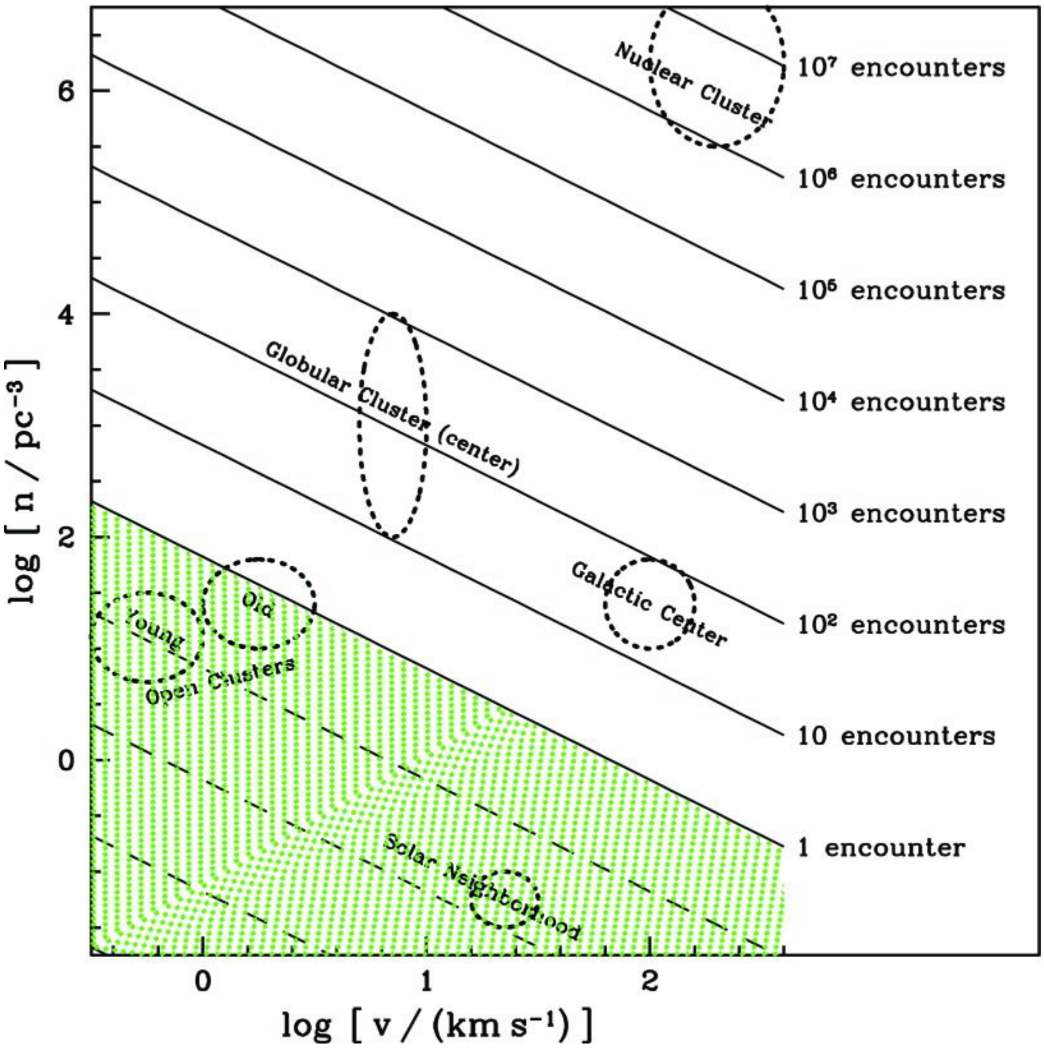

Figure 3.1: Log-log diagram of density as a function of the velocity dispersion in different Galactic environments (black-dash line). Straight black lines represent the number of encounters given a density and velocity dispersion for a total integration time T_e for all environments of 5 Gyr. The green shadow covers the galactic regions where less than one stellar encounter occurred in its history (from Jiménez-Torres *et al.*, 2013).

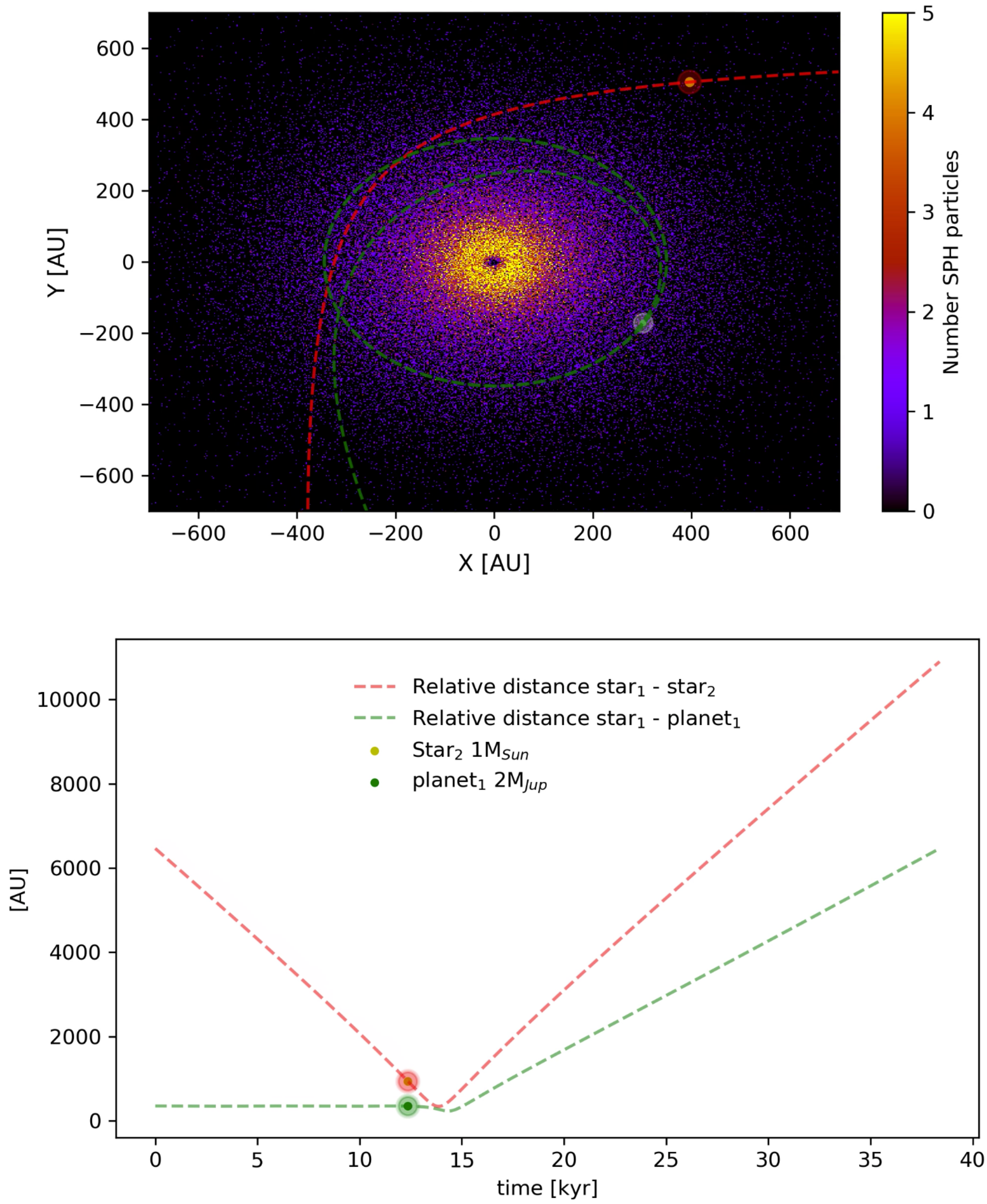

Figure 3.2: The dynamical evolution of a young planetary system around a central star 1 M$_\odot$ with a single planet 2 M_{Jup} (green dot), fully embedded in a gaseous disk $0.01\ M_\odot$ in presence of a stellar perturber 1 M$_\odot$ (red dot). The Jovian planet (green dash line), after the stellar flyby (red dash line), is completely ejected from the planetary system. We used, for this numerical simulation, the GaSPH hydrodynamical code.

However, planets are often ejected as the cumulative result of several weak scattering events. During fly-by encounters, stellar perturbers can also capture planets from the planetary system (Malmberg *et al.* 2011). In this way, stellar clusters not only provide to shape the forming planetary systems but, if the stellar perturber possesses its own planetary system, an extra planet may enrich and destabilize the system.

Chapter 4

Simulations of the dynamics of circumstellar structures

4.1 Numerical simulations: generalities

Many young stellar systems contains stars surrounded by circumstellar gaseous disks during their early evolution. Several evidences of their existence were obtained in the late 1980s and, increasing the accuracy of the observations, interesting structures were identified in the disk images, such as spiral arms (Grady *et al.* 2001; Hashimoto *et al.* 2011; Christiaens *et al.* 2014; Takakuwa *et al.* 2014) and ring-shaped gaps (Weinberger *et al.* 1999). The formation of spiral arms and gaps might be a consequence of the dynamical interactions of young systems with external perturbers in a stellar environment. It is well known that many structures are affected by gravitational perturbations of passing-by massive objects such as galaxy-galaxy encounters or perturbations of protoplanetary disks, debris disks and planetary systems by passing stars (Farouki & Shapiro 1981; Clarke & Pringle 1993; Heller 1995; Hall 1997; Kobayashi & Ida 2001; Melita *et*

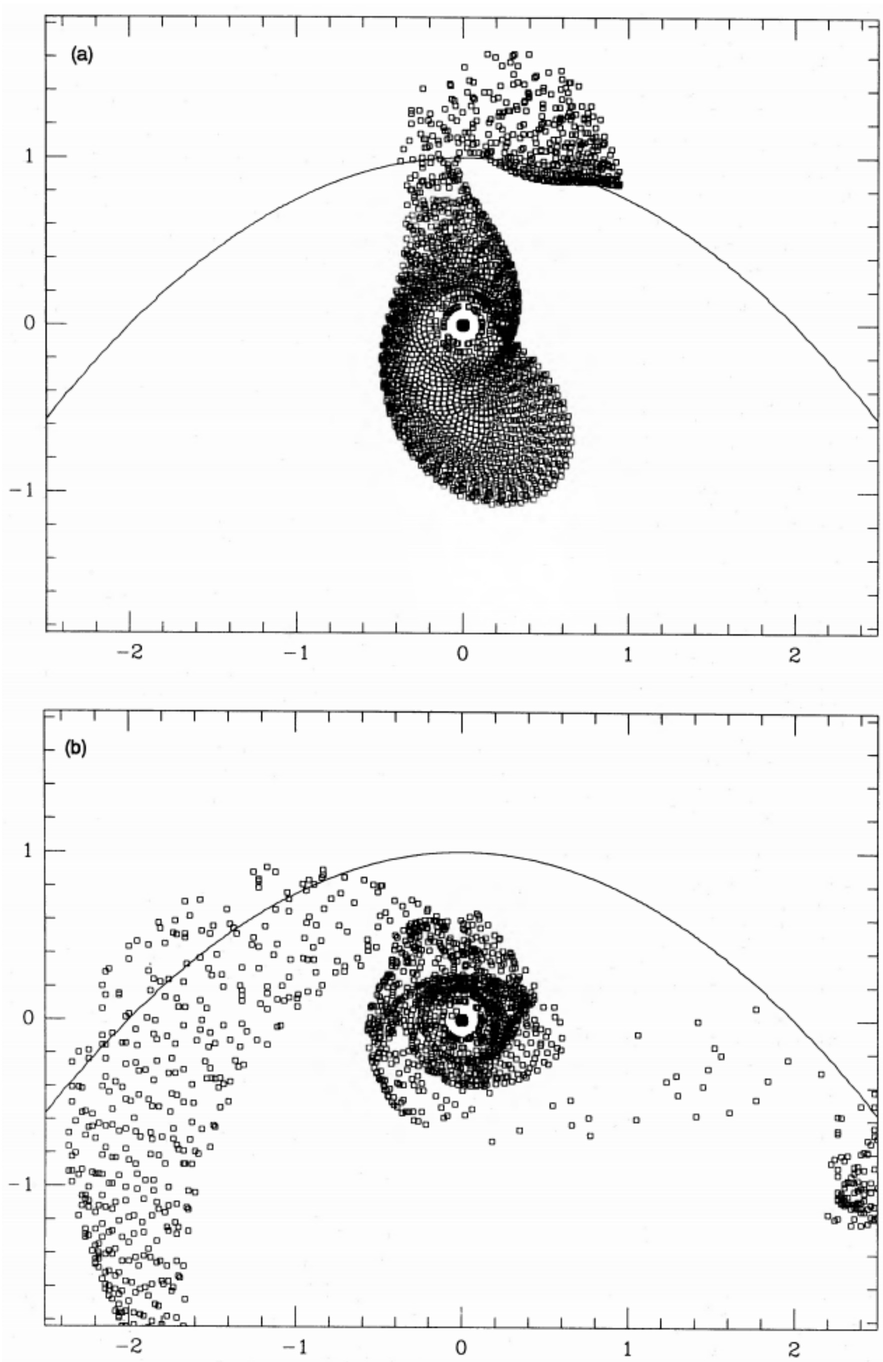

Figure 4.1: Dynamical evolution of a circumstellar disk by Clarke & Pringle, 1993. The units of length in the plot (a) and (b) are in terms of the periastron separation r_{per}. The stellar perturber is on a coplanar prograde orbit. The disk initially has outer radius 0.8 r_{per} and uniform surface density. In (a) the perturber is at periastron r_{per} and in (b) it is out of the frame. The disk, after the stellar flyby, is strongly perturbed and some particles are captured by the perturber (from Clarke & Pringle, 1993).

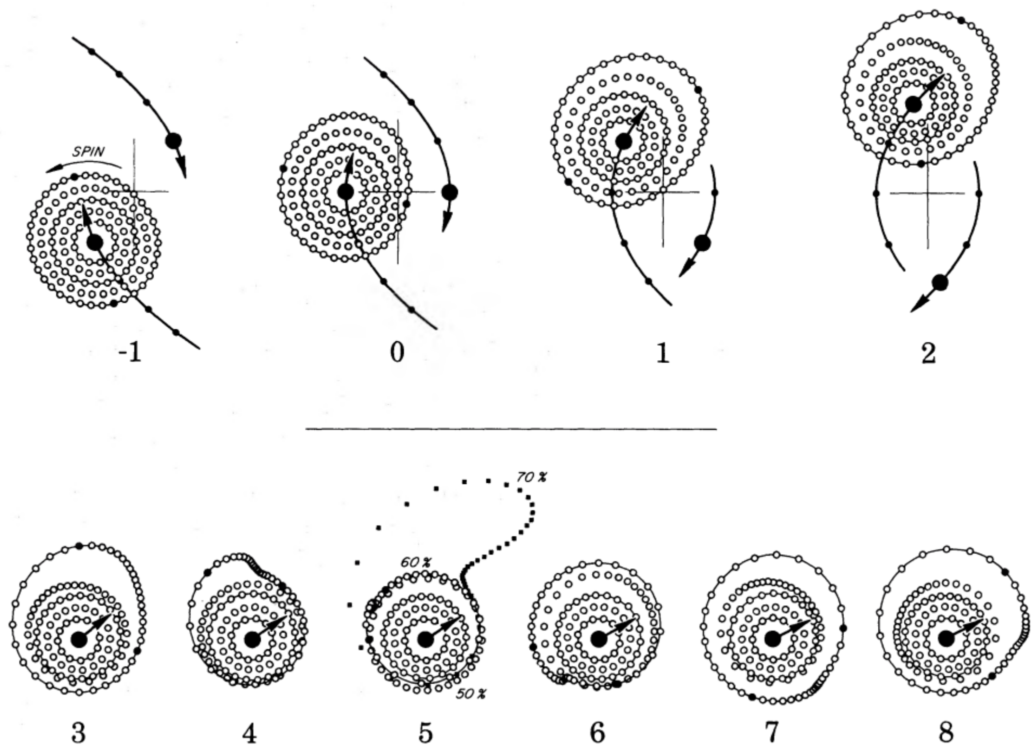

Figure 4.2: Dynamical evolution of a circumgalactic disk by Toomre & Toomre, 1993, during a coplanar retrograde encounter of a companion of equal mass. The two small black filled circles are test particles located at 0.6 r_{per}. The filled squares at time = 5, are additional test particles at 0.7 r_{per} (from Toomre & Toomre, 1993).

al. 2002; Levison *et al.* 2004; Pfalzner *et al.* 2005; Olczak et al.2006; Scharwächter *et al.* 2007; Malmberg *et al.* 2011; Craig & Krumholz 2013; Punzo *et al.* 2014). In some works (Toomre & Toomre (1972), Hall *et al.* (1996), Kobayashi & Ida (2001), Pfalzner *et al.* (2005)) the perturbed disk is investigated neglecting the self interaction of the disk material such as self-gravity or viscosity, approximating all these cases as a subset of the "restricted" three-body problem. Toomre & Toomre (1972) performed simulations of galaxy perturbations with non-interacting low-mass disk particles (see Fig. 4.2). Since they modelled the gravitational potential of the galaxies as point masses, their results are comparable to the simulations of low-mass disks around stars. Clarke & Pringle (1993) and Hall *et al.* (1996) investigated the perturbation of protoplanetary disks in equal-mass encounters and presented the probability for a disk particle to have a certain fate (remaining bound, being captured by the perturber, left unbound) depending on its initial distance from the parent star. In particular Clarke & Pringle (1993) (see Fig. 4.1) investigate the effect on an accretion disk around one target star after a parabolic stellar fly-by. In the coplanar prograde encounter, the disk is tidally stripped down, when the perturber is on its orbital periastron, and a substantial fraction of the stripped material is captured by the perturber. In the coplanar retrograde configuration of the orbit of the stellar perturber, the disk is essentially unperturbed. They consider the evolution of a disk, made of 2500 particles. In order to avoid excessive viscous evolution of the disk close to periastron of the orbit of the stellar perturber, they neglect the viscosity until the stellar perturber approaches enough its orbital periastron. A more detailed study of such stellar fly-by requires the use of hydrodynamic codes. For example, three-dimensional (3D) hydrodynamical simulations of circumstellar structures were performed by Bate & Bonnell (1997); Larwood & Papaloizou (1997) using the Smoothed Particle Hydrodynamics (SPH) method. Their numerical simulations show evidences of spiral waves in a circumstellar gas disk when it interacts with a planet (Nelson 2000; Kley & Nelson 2008; Paardekooper *et al.* 2008; Marzari *et al.* 2009; Picogna & Marzari 2013). If the planet's orbit is inclined respect to the disk plane, then a vertical warp is formed in its central parts (Grinin *et al.* 2010; Demidova & Sotnikova 2013; Xiang-Gruess & Papaloizou 2013). The investigation of the dynamical evolution of a planetary and protoplanetary system is a hard work and the modelization of each astrophysical structure represents a careful compromise between the physical details and the computational effort needed to simulate it.

4.2 Numerical simulations via Smoothed Particles Hydrodynamics

In this section, we discuss the basic theoretical formulation of the Smoothed Particle Hydrodynamics (hereafter SPH) formalism. It represents an introduction to the GaSPH code (Pinto *et al.* 2019) used to investigate the evolution of a self-gravitating systems in Chapter 5. Introduced for the first time contemporary by Lucy (1977) and Gingold & Monaghan (1977), the SPH scheme has been widely adopted to investigate a huge set of astronomical problems involving fluid systems. SPH is a Lagrangian method which is based on representing the fluid as a system of smooth 'pseudo-particles'. For each particle, a set of fundamental quantities (such as density, ρ, pressure, P, internal energy density u, velocity $\mathbf{v}$) are calculated by means of an interpolation with a proper kernel function over a suitable neighbour. Actually, the interpolations are performed with a continuous kernel function $W(r;h)$, whose spread scale is defined by a characteristic length, h, called "smoothing length". Monaghan & Lattanzio (1985) used, as kernel function, a cubic spline, which has the form:

$$W(r;h) = \frac{1}{\pi h^3} \cdot \begin{cases} 1 - \frac{3}{2}\left(\frac{r}{h}\right)^2 + \frac{3}{4}\left(\frac{r}{h}\right)^3, & 0 \leq r < h \\ \\ \frac{1}{4}\left(2 - \frac{r}{h}\right)^3, & h \leq r < 2h \\ \\ 0\,, & r \geq 2h \end{cases} \tag{4.1}$$

The SPH interpolation involves only a limited set of N' neighbours particles that are enclosed within the range of distances $r < 2h$, thus the relative computational effort scales linearly with the total particle number N. However, when long-range interactions, such as gravity, are considered, the computational effort grows up because each particle interacts with the whole system. A classical direct N-Body code would, hence, require a computational weight scaling as N^2. To fix this problem, Barnes & Hut 1986 introduced a suitable gravitational "tree-based" scheme to evaluate efficiently the Newtonian force by approximating the potential with a harmonic expansion. For each particle, only the contribution given by a local neighbourhood is calculated through a direct particle-particle summation, while the contribution from farther particles is, indeed, suitably approximated. The following expressions represent the approximated potential $\Phi(\vec{r})$ and the force (per unit mass) $(\vec{a}) = -\nabla\Phi(\vec{r})$ given by a far *cluster* of particles:

$$\Phi(\vec{r}) = -\frac{GM}{r} - \frac{1}{2}\frac{G\,\vec{r}\vec{\overline{\overline{Q}}}\vec{r}}{r^5} \tag{4.2}$$

$$\vec{a}(\vec{r}) = -\frac{GM}{r^3}\vec{r} + \frac{G\vec{\overline{\overline{Q}}}\cdot\vec{r}}{r^5}\vec{r} - \frac{5}{2}\frac{G\,\vec{r}\vec{\overline{\overline{Q}}}\vec{r}}{r^7}\vec{r} \tag{4.3}$$

where M is the total mass of this ensemble, $r = |\vec{r}|$ is the distance of the particle under study to the center of mass of the cluster. The symbol $\vec{\overline{\overline{Q}}}$ represents the so-called quadrupole tensor, which is associated with the specific cluster. In indexed form, it is given by

$$Q_{ij} = \sum_{k=1}^{N_C}\left(3x_i^{(k)}x_j^{(k)} - r_k^2\delta_{ij}\right)m_k, \tag{4.4}$$

where $x_i^{(k)}$ and $x_j^{(k)}$, with $i, j = 1, 2, 3$, refer to the Cartesian coordinates of the k^{th} particle of mass m_k. For a generic i^{th} particle, the acceleration $\vec{a_i}$ is computed by adding both the SPH terms and the Newtonian terms in the same iteration. Particles can be considered as point sources of the Newtonian field as far as their mutual distance is larger than $2h$. Otherwise, their Newtonian interaction is, in consistency with the assumed kernel function (Gingold & Monaghan, 1977), such that it vanishes at inter-particle distance approaching to zero. Using the cubic spline kernel, a different form of the Newtonian interaction between two particles can be obtained, such that the classical term is softened if the particles approach within a distance of the order of a *softening length* defined as $\epsilon = 2h$. Springel & Hernquist (2002)used the Hamiltonian formalism for the hydrodynamical interactions, further developed by Price & Monaghan (2007) for the gravitational field. The SPH equations assume, thus, the following form:

$$\begin{aligned}\frac{d\vec{v}_i}{dt} = -\sum_j \frac{1}{2}\left(g_{\text{soft}}(r_{ij},h_i) + g_{\text{soft}}(r_{ij},h_j)\right)\frac{\vec{r_{ij}}}{r_{ij}} + \\ -\sum_j m_j \frac{G}{2}\left(\frac{\zeta_i}{\Omega_i}\nabla_i W(r_{ij},h_i) + \frac{\zeta_j}{\Omega_j}\nabla_i W(r_{ij},h_j)\right) + \\ -\sum_j m_j \left(\frac{P_i}{\rho_i^2\Omega_i}\nabla_i W(r_{ij},h_i) + \frac{P_j}{\rho_j^2\Omega_j}\nabla_i W(r_{ij},h_j)\right) + \\ -\sum_j m_j \Pi_{ij}\left[\frac{\nabla_i W(r_{ij},h_i) + \nabla_i W(r_{ij},h_j)}{2}\right] + \frac{d\vec{v}_i}{dt}^{[stars]},\end{aligned} \tag{4.5}$$

$$\frac{du_i}{dt} = \sum_j m_j \left(\frac{P_i}{\rho_i^2\Omega_i} + \frac{1}{2}\Pi_{ij}\right)\vec{v_{ij}}\cdot\nabla_i W(h_i), \tag{4.6}$$

where the index i refers to a generic i^{th} particle and the index j in the sums refers to the j^{th} particle that is enclosed within the range $2h = 2\cdot\max(h_i,h_j)$. The term g_{soft} represents the softened gravitational force per unit mass: it is a function only of the mutual particle distance r_{ij} and of the smoothing length h. The operator ∇_i represents the gradient with respect to the coordinates of the i^{th} particle. The gradient is performed over two different expressions of the Kernel $W(r;h)$, with two different lengths h_i and h_j. The terms ζ_i, and Ω_i are suitable functions which account for the variation of the smoothed Newtonian potential with respect to the softening length. They assume, for a generic particle of index i, the following form:

$$\Omega_i = 1 + \frac{h_i}{3\rho_i} \sum_j m_j \vec{\nabla}_i W(r_{ij}, h_i) \tag{4.7}$$

$$\zeta_i = -\frac{h_i}{3\rho_i} \sum_j m_j \frac{\partial\, \phi_{\text{soft}}(r_{ij}, h_i)}{\partial h_i}, \tag{4.8}$$

where the sum extends over the particles enclosed within the range 2h$_i$. The function ϕ_{soft} represents the softenend gravitational potential, such that $\nabla\phi_{soft} = -g_{soft}\ \vec{r_{ij}}/r_{ij}$. The potential reaches a constant value as $r_{ij} \to 0$ and becomes equal to the Newtonian potential for $r_{ij} \geq 2h$ (Price & Monaghan, 2007). If the gas interacts with stars, in the equation (4.5) the last term $d\vec{v_i}^{\ [stars]}/dt$ represents the acceleration accounting for the Newtonian interaction between particle i and the stars.

Artificial viscosity

In high compression regions, such as shock wave fronts, the velocity gradient may be so strong that two layers may permeate and the hydrodynamical equations may not be integrated correctly, generating non-physical effects. Monaghan (1989) added an artificial pressure term, which derives from the introduction of a suitable "artificial" viscosity, aimed to damp the velocity gradient when two particles approach. Consequently, it derives a viscous-pressure term Π_{ij} as:

$$\Pi_{ij} = \begin{cases} \dfrac{-\alpha\bar{c}\mu_{ij} + \beta\mu_{ij}^2}{\bar{\rho}_{ij}} & , \text{ if } \quad \vec{v_{ij}} \cdot \vec{r_{ij}} < 0, \\ 0 & , \text{ if } \quad \vec{v_{ij}} \cdot \vec{r_{ij}} > 0, \end{cases} \tag{4.9}$$

where $\mu_{ij} = \dfrac{h\vec{v_{ij}} \cdot \vec{r_{ij}}}{r_{ij}^2 + \eta^2\bar{h}^2}$. The dot product $\vec{v_{ij}} \cdot \vec{r_{ij}}$ involves the relative velocity and the distance of a pair of particles i and j. Only the pair of particles which approach, for which $\vec{v_{ij}} \cdot \vec{r_{ij}} < 0$, give a contribution to the artificial viscosity. The parameter η is a suitable term to prevent singularities when two particles get very close. The terms $\bar{h}$, $\bar{\rho}$ and $\bar{c}$ represent respectively the average values of the smoothing length $\frac{1}{2}(h_i + h_j)$, the density $\frac{1}{2}(\rho_i + \rho_j)$ and the speed of sound $\frac{1}{2}((c_s)_i + (c_s)_j)$. α, called $bulk$ viscosity, is responsible to damp the non-physical velocity oscillations contributing with a diffusive effect, while $\beta = 2\alpha$ is the $Von\ Neuman$-$Richtmyer$ viscosity which contributes to a pressure term. Artificial viscosity must be damped in regions where shear dominates, and where the velocity gradient is low. Considering two shearing layers of fluid, the relative velocity, between the particles, leads to an approach which is *interpreted* by the artificial viscosity as a compression. Such wrong interpretation may lead to a computational overestimation of the strength of the viscous interaction. To prevent false compressions, Balsara (1995) multiplied the term μ_{ij} by a proper switching coefficient:

$$f = \frac{|\vec{\nabla} \cdot \vec{v}|}{|\vec{\nabla} \cdot \vec{v}| + |\vec{\nabla} \times \vec{v}| + 10^{-4} c_s h^{-1}}, \tag{4.10}$$

with the divergence of velocity and the velocity curl evaluated, for a particle of index i, as:

$$\begin{cases} \left(\vec{\nabla} \cdot \vec{v}\right)_i = \rho_i^{-1} \sum_j m_j\, \vec{v}_{ij} \cdot \vec{\nabla}_i W(r, h_i) \\ \left(\vec{\nabla} \times \vec{v}\right)_i = \rho_i^{-1} \sum_j m_j\, \vec{v}_{ij} \times \vec{\nabla}_i W(r, h_i) \end{cases} \tag{4.11}$$

Further problems may arise far away from high compression regions. In the classical formulation of Π_{ij}, $\alpha = 1 = cost.$ (Monaghan, 1992). In such scheme, the viscosity uniformly acts in every region but we would expect the artificial term to be efficient close to the shock fronts. To solve such issue, Morris & Monaghan (1997) used a formalism considering, for each particle, an individual α_i which follows the time variation equation:

$$\frac{d\alpha_i}{dt} = -\frac{(\alpha_i - \alpha_{\text{min}})}{\tau_\alpha} + S_i, \tag{4.12}$$

where $S_i = \max(-(\vec{\nabla} \cdot \vec{v})_i, 0)\ (\alpha_{\text{max}} - \alpha_{\text{min}})$ represents a *source* term that increases in the proximity of the shock front; α_{min} represents a minimum threshold value for α, and α_{max} represents its maximum. The rate of the viscosity coefficient is driven by a characteristic timescale $\tau_\alpha = h_i/bc_s$ which depends on how the fluid lets the perturbations propagate through the resolution length. The individual viscosity coefficients, α_i and α_j, when referred to a generic $i-j$ particle pairing, are averaged in the same way as done with the other quantities.

Chapter 5

Young planetary systems in stellar environments

5.1 Dynamical evolution of a young planetary system

GaSPH (Pinto *et al.* 2019) is an optimized SPH code which deals with self gravity by means of a tree-based scheme. According to the classical Flared-Disk model, the disk revolves around the central object with a Keplerian frequency $\Omega_k \approx \sqrt{M_s G/R^3}$ where R is the cylindrical coordinate $R = \sqrt{(x^2 + y^2)}$ in the reference frame centered in the central object.
According to the α-disk model (Shakura & Sunyaev 1973), the internal disk turbulence is schematized by means of a pseudo viscosity of the form:

$$\nu = \alpha_{SS}\, c_s\, H \tag{5.1}$$

Such a kinematic viscosity leads to a net transport of matter inward and a contemporary outward flux of angular momentum. In the above expression, α_{SS}

represents a characteristic efficiency coefficient for the momentum transport, while $H = c_s/\Omega_k$ represents a vertical pressure disk scale height. When the disk self-gravity is stronger enough some gravitational perturbations arise. Mayer *et al.* (2002) and Boss *et al.* (2003), gave a numerical estimation of the gravitational timescales in a protoplanetary disk. They have shown that, under certain conditions, matter can undergo instabilities and eventually condense forming clumps (in $\sim 10^4$ yr). It can been shown that a disk keeps its equilibrium state against collapse according to the Toomre's criterion:

$$Q = \frac{c_s \Omega_e}{\pi G \Sigma} > 1.5, \tag{5.2}$$

where Ω_e represents the epicyclic frequency, which is approximately equal to Ω_k for Keplerian disks. The Toomre's factor is a parameter which quantifies the role of gravitational processes over the typical thermal and dynamical actions. The disk revolves with an azimuthal velocity: $v_\phi(R) = \sqrt{\frac{G(M_s+M(R))}{R}}$ which depends both on the mass of the central star M$_s$ and on the projected internal mass of the disk itself, $M(R) = \int_0^R \Sigma(R) 2\pi R dR$. However the mass $M(R)$ can be neglected in the case of low disk masses $M_D \ll M_S$. The vertical shape of the disk depends on the vertical pressure scale height H, such that pressure and density scale with a gaussian profile $exp(-z^2/2H^2)$. Here a local vertically isothermal approximation is used, assuming that any radiative input energy from the star is efficiently dissipated away: the cooling times are far shorter than the dynamical time-scales. The disk is thus vertically isothermal and the temperature depends only on the radial distance from the central star. Hence, according to the flared disk model, the disk termal profile, for which the ratio $H(R)/R$ increases with R, is:

$$T = T_0 \left(\frac{R}{R_0}\right)^{-q}, \tag{5.3}$$

and which is commonly used by setting $q = 1/2$ where R_0 is a scale length. Pinto *et al.* (2019) use a slightly different slope $q = 3/7$, adopted by D'Alessio *et al.* (1999) making the assumption that the thermal processes in the inner layers of the disk do not affect its dynamical stability. The effects of the Shakura-Sunyaev viscosity associated to Keplerian disks can be represented by means of the SPH artificial viscosity. Meglicki *et al.* (1993) found that the SPH viscosity coefficient α provides a viscous acceleration containing a similar form with shear component plus a bulk viscosity. Considering a cubic spline as kernel function, they have shown that the pseudo viscosity, ν, assumes the following form:

$$\nu \propto \alpha \, c_s \, h. \tag{5.4}$$

Where h is the smoothing length and c_s the sound speed. Hence, the law which connects the Shakura-Sunyaev viscosity coefficient to the α parameter used in SPH is:

$$\alpha_{SS} = \frac{\alpha \, h}{10 \, H}. \tag{5.5}$$

Such modification of the SPH formalism provides a more realistic prediction of the effect given by a kinematic viscosity since it acts both under compression and under gas expansion. Such a prescription is reliable as far as we have to deal with strong velocity gradients (i.e. shock waves). However, this is not a limitations because the protoplanetary disks are usually modeled as quiet systems and are not expected to undergo such huge compressions to let strong shock waves arise.

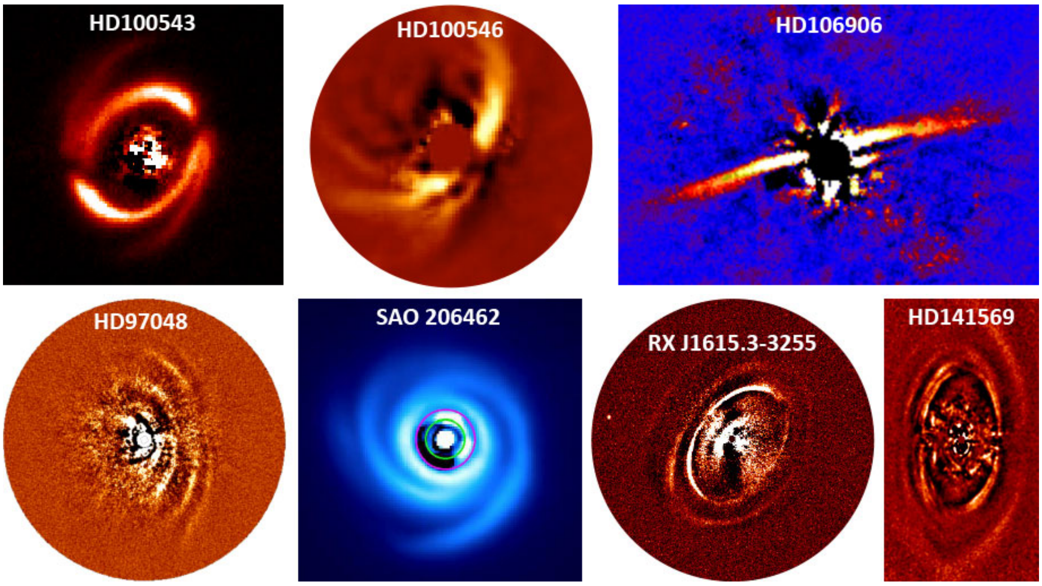

Figure 5.1: Gallery of protoplanetary and debris disks obtained with SPHERE (Spectro-Polarimetric High-contrast Exoplanet REsearch) in the SHINE (SpHere INfrared survey for Exoplanets) survey. These protoplanetary disk images, obtained with a resolution less than 10.8 arc-seconds per pixel, may provide clues as to the planets forming inside them (from http://astro.vigan.fr/shine).

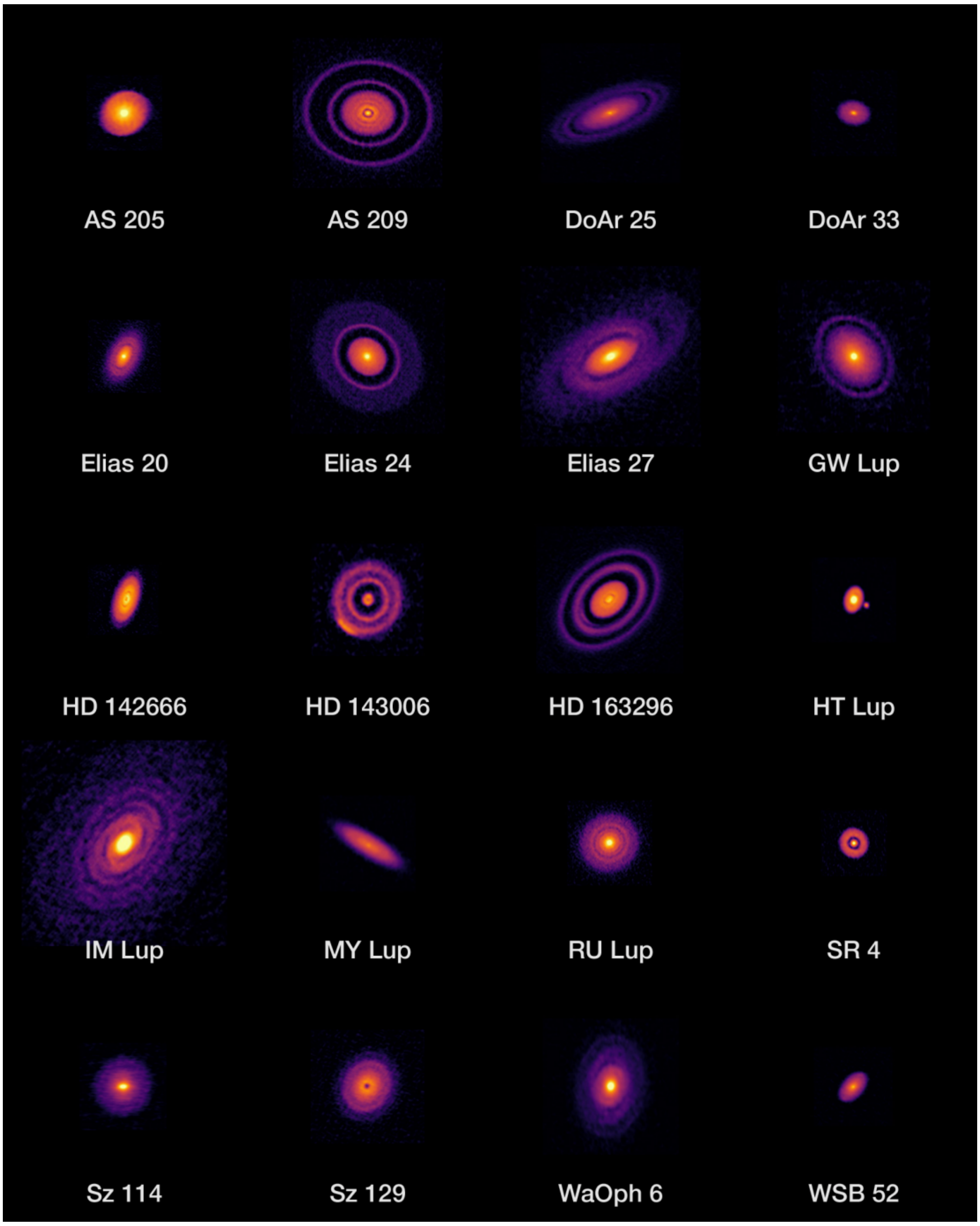

Figure 5.2: Protoplanetary disks imaged by DSHARP (Disk Substructures at High Angular Resolution Project) with ALMA (Atacama Large Millimeter/submillimeter Array) (from Andrews S. M. *et al.*, 2018)

5.2 Young planetary systems in an open stellar cluster

Most stars form in stellar cluster (Hillenbrand *et al.* 1998; Palla & Stahler 2000) even our Sun (Dukes & Krumholz 2012), therefore their planetary architectures are suspected to be affected by several stellar gravitational interactions (Picogna & Marzari 2014, Rosotti *et al.* 2014, Cuello *et al.* 2018). If the planetary system is aged in the interval 3 - 12 Myr, it may still show a circumstellar disk (Haisch *et al.* 2001), and a coexistence between a young forming planet and the gaseous disk is predicted both by theoretical models (Pollack *et al.* 1996) and observations as given by several surveys obtained by instruments like SPHERE (Beuzit J. L., *et al.*, 2019) and see Fig. 5.1), through a direct imaging in the near-infrared, or in radio bands by ALMA (Andrews *et al.* 2018 and see the Fig 5.2).

Several studies have simulated circumstellar disks using different approaches, starting from a clump of "test particles" to a full hydrodynamical approach. A pure N-body simulation test particles approach represents only a rough approximation, although computationally useful, of the dynamics of a real circumstellar disk: no viscosity and no pressure forces are taken in account.
Rosotti *et al.* (2014) considered the evolution of a circumstellar disks in a stellar environment combining N-body simulations for the stellar cluster and an hydrodynamic code to model the gaseous disk. However, these authors do not include any planet or protoplanet inside the circumstellar disk; moreover each disk is simulated with a very large stellar accretion radius (from 1 AU to 20 AU) so that the dynamics in the inner regions of the disk is essentially neglected. Breslau *et al.* (2017) used an N-body calculation to study tidal truncation of the circumstellar disk. Assuming prograde coplanar parabolic encounters, they find that

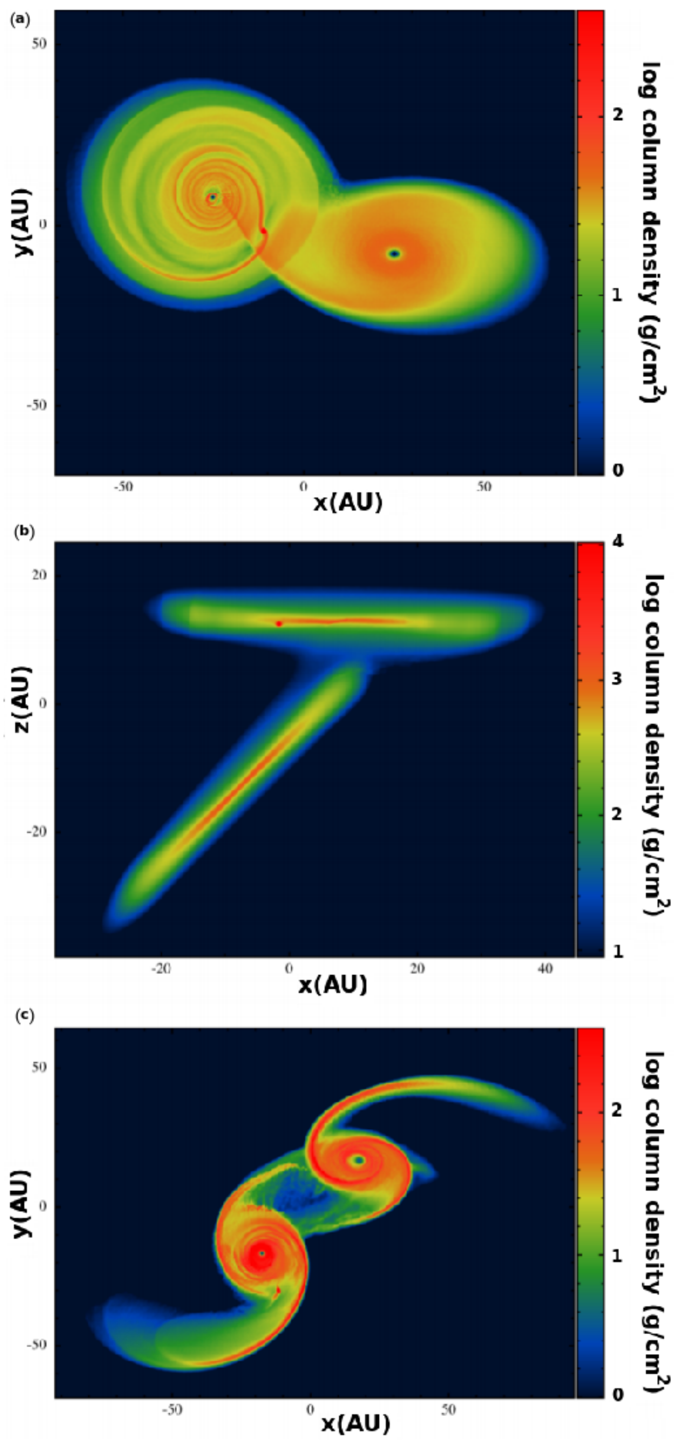

Figure 5.3: Logarithm of the superficial density (column integrated) of the circumstellar disks during a stellar flyby. The two top plots (a) and (b) show the disks when the stellar perturber is close to its orbital periastron, while the bottom plot (c) shows the stellar perturber 60 yrs after the close encounter (from Picogna&Marzari, 2014)

.

the final disk size is a function of the periastron and the mass ratio. They also estimated the portions of unbound, captured, and remaining material around the primary star after the flyby, finding that the prograde encounters are the most destructive. By contrast, retrograde encounters were found to leave the disk almost intact. However they did not consider any planet or protoplanet in their simulations.

Picogna&Marzari (2014) proposed a study on the effects of the disk on the dynamics of planets after a stellar encounter. They confirm that if the circumstellar disk is still present during (and after) a stellar flyby, a planetary system returns to a non excited state on a short timescale (see Fig. 5.3). Using a 3D hydrodynamical modeling of the circumstellar disk, they explored different inclinations between the disk, planet orbit and stellar trajectory. Both the perturber and the central system are equipped by a low density disk.

They set the initial distance of the stellar perturber at 450 AU (roughly 8 times the Pluto's aphelion) unfortunately too small in order to simulate a realistic dynamics of a stellar flyby.

5.2.1 Initial set-up

The dynamical evolution of the whole system is followed by 3D simulations using the code GaSPH (Pinto et al. 2019). The environment, where our disk and planet are embedded in, is that of a young open stellar cluster, which typically contains up to 10^3 stars and 1 pc as typical half mass radius.

For the stellar perturber, we chose five different values of the mass: 0.5, 0.8, $1, 3$ and $8\ \mathrm{M}_{\odot}$. These values cover sufficiently the range of star masses in an open cluster. The initial speed, v_∞, of the stellar perturber is assumed 2 km/s, compatible with the typical star speed in a young open clusters. We studied interactions of a flyby star moving on tilted orbits respect the plane of the target disk around the primary star. The inclinations i of the orbits of the stellar perturber are assumed: $0°$, $45°$, $90°$, $135°$ and $180°$. The angles $0°$ and $45°$ are the inclinations of the *prograde* orbits (co-rotating respect to the planet revolution around the primary) while the angles $135°$ and $180°$ are the inclinations of the retrograde (counter-rotating) orbits. Finally, $i = 90°$ represents a flyby motion orthogonal to the disk containing the planet. For each stellar perturber mass and inclination, we selected the following periastron distances (r_p): 100, 200, 300, 400, 500 AU. Starting from the above given periastron distance, we calculated the impact parameter, p, of the incoming stellar perturber by the relation:

$$p = r_p \sqrt{1 + 2\frac{GM_{tot}}{r_p {v_\infty}^2}}, \tag{5.6}$$

where M_{tot} is the total mass of the system (central star + stellar perturber + disk + Jovian planet).

For our orbital integrations a relevant role is played by the starting position of the stellar perturber. In our investigation we choose as starting distance that at which the tidal perturbation on the disk+star+planet system gives a fractional amplitude:

$$\delta = \frac{F_{tid}}{F_{rel}} = 10^{-4}$$

where F_{tid} and F_{rel} are the initial tidal force between the planetary system and the stellar perturber, and the initial relative force between each component of the planetary system (Fregeau *et al.* 2004). The time length of each simulation is obtained by considering twice the time interval from the initial position of stellar perturber to the periastron of the orbit of the perturber. We simulated the gaseous disk using 2×10^4 SPH particles; this number represents a good compromise between the computational effort and the realistic simulation of the dynamics. Actually, we checked that $N \sim 2 \times 10^4$ guarantees a good convergence of the relevant outputs of the simulations. The initial mass of the disk is assumed 0.009 M$_{Sun}$, which is, basically, the Solar Minimum Mass Nebula 0.01 M$_{Sun}$ (Hayashi *et al.* 1981) minus the embedded Jovian planet mass. The initial inner cut-off of the disk, R$_{in}$, is set to 1 AU and the external cut-off, R$_{out}$, of the disk is set to 70 AU.

The feedback on the disk of the external perturbation can be quantified, for instance, by the time variation of its Lagrangian radii. A this scope, we follow Bate (2018) considering as “radius” of the SPH disk radius the Lagrangian radius 63.2% of its total mass. We consider a fully formed giant planet with a mass of 1M$_{Jup} \simeq \frac{1}{1000} M_{\odot}$.

Its initial circular, and coplanar to the disk, orbit was set at a 10 AU radius, well beyond the typical solar-like snow line (~ 2.7 AU). We consider the possibility of mass accretion of the planet, whose mass grows whenever an SPH particle falls inside the planetary sink radius. In order to simulate a realistic accretion we set, as suggested in Bate & Ayliffe, a planetary sink radius $\frac{r_H}{50}$ where r$_H$ is the initial Hill radius of the planet:

$$r_H = a \left(\frac{M_{p0}}{3M_{\star 0}} \right)^{1/3}; \tag{5.7}$$

where a is the initial distance of the planet with initial mass M$_{p0}$ revolving around a star with initial mass M$_{\star_0}$.

5.2.2 Results

To measure the response of the Jovian planet to the perturbation, we consider proper averages of the planetary distance from the central star as well as its orbital eccentricity and mass accretion. At the scope of a quantitative analysis of

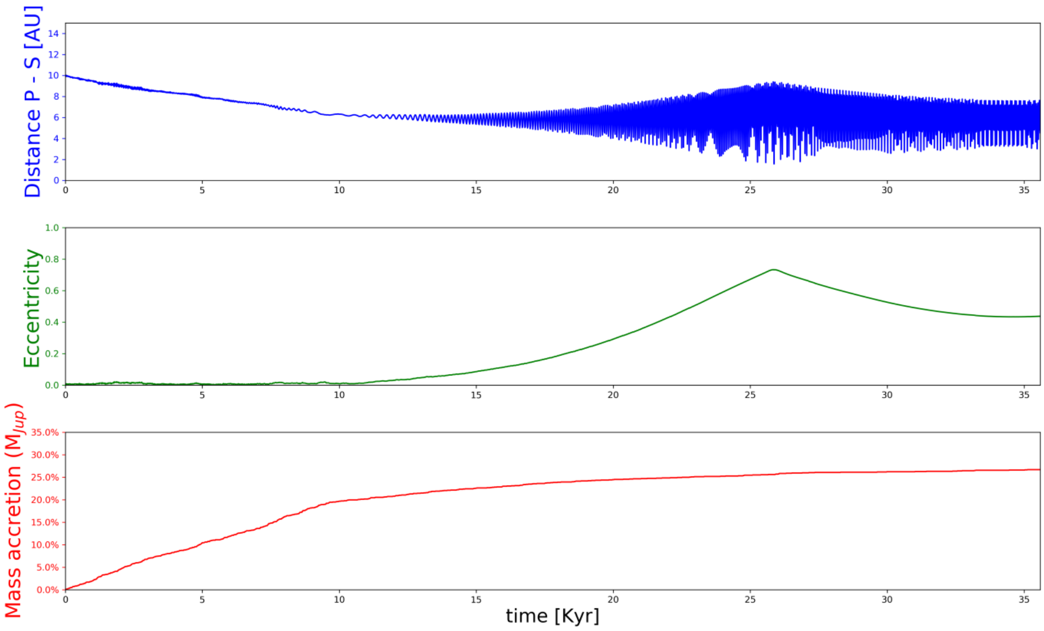

Figure 5.4: Dynamical evolution of the distance (blue-solid line) between the Jovian planet (P) and the central star (S), the planetary eccentricity (green solid line) and the planetary mass accretion (red solid-line). In this model, the Jovian planet experiences a pure planet-disk interaction without any external gravitational perturbation.

the feedback of the disk to the external perturbation, we followed Bate (2018) and consider as "radius" of the SPH disk the Lagrangian radius of 63.2% of its total mass. The value of each measurement at the end of the simulation is evaluated making an average over a time interval of 10 times the initial planetary orbital period which is 31.60 yr.

Disk feedback

The final $r_{63.2}$ of the disk, after different encounters, show several cases of truncation and diffusion. We define a *disk truncation* when the final $r_{63.2}$ of the disk is lower than the final $r_{63.2}$ of the disk in the unperturbed model and a *disk dif-*

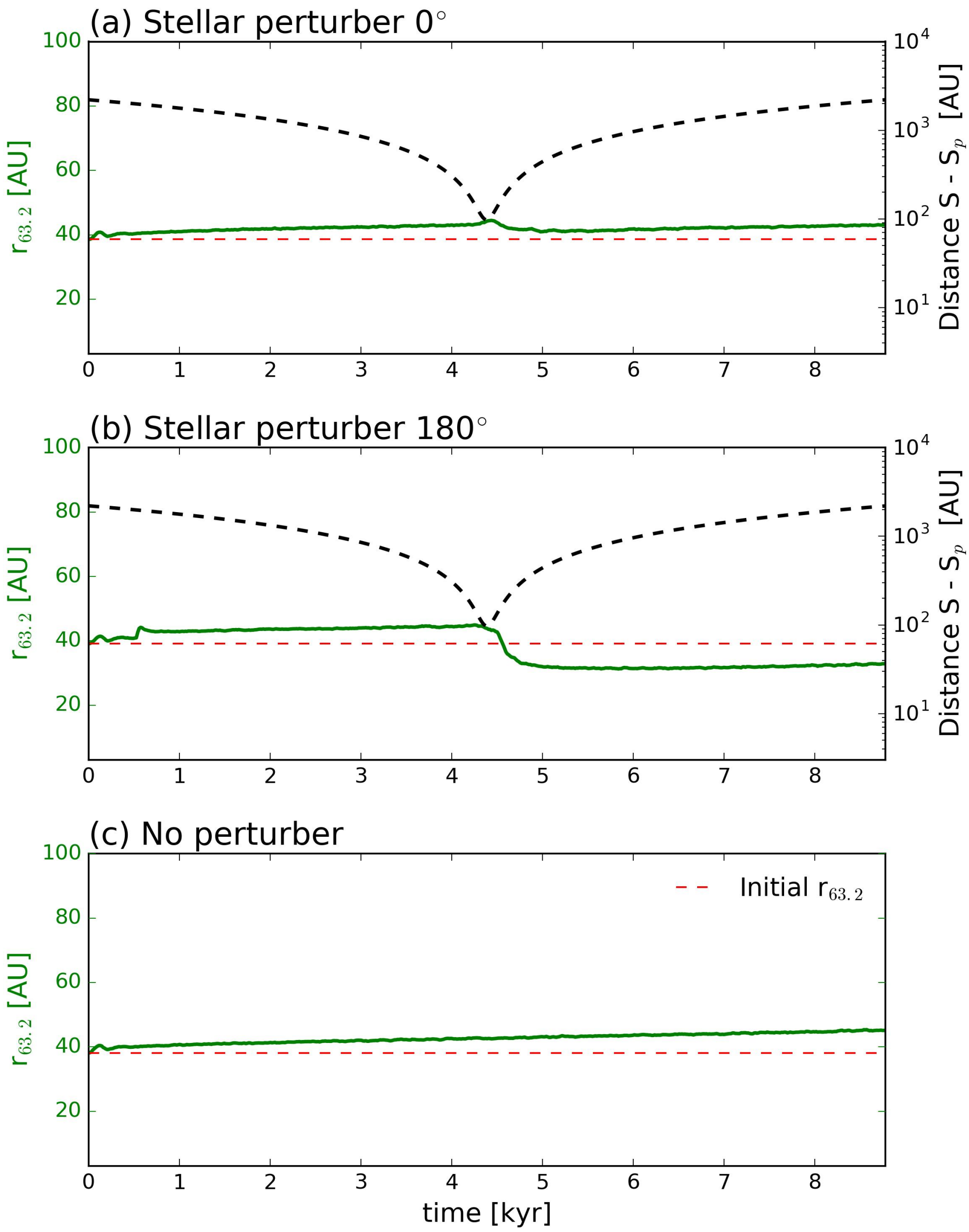

Figure 5.5: Dynamical evolution of the Lagrangian radius of 63.2% of the total mass of the gaseous disk (green solid-line) during a stellar flyby of a perturber of 0.5 $M_\odot$ (black dash-line) in a prograde (a) and retrograde (b) configuration. In (c) the model without stellar perturber.

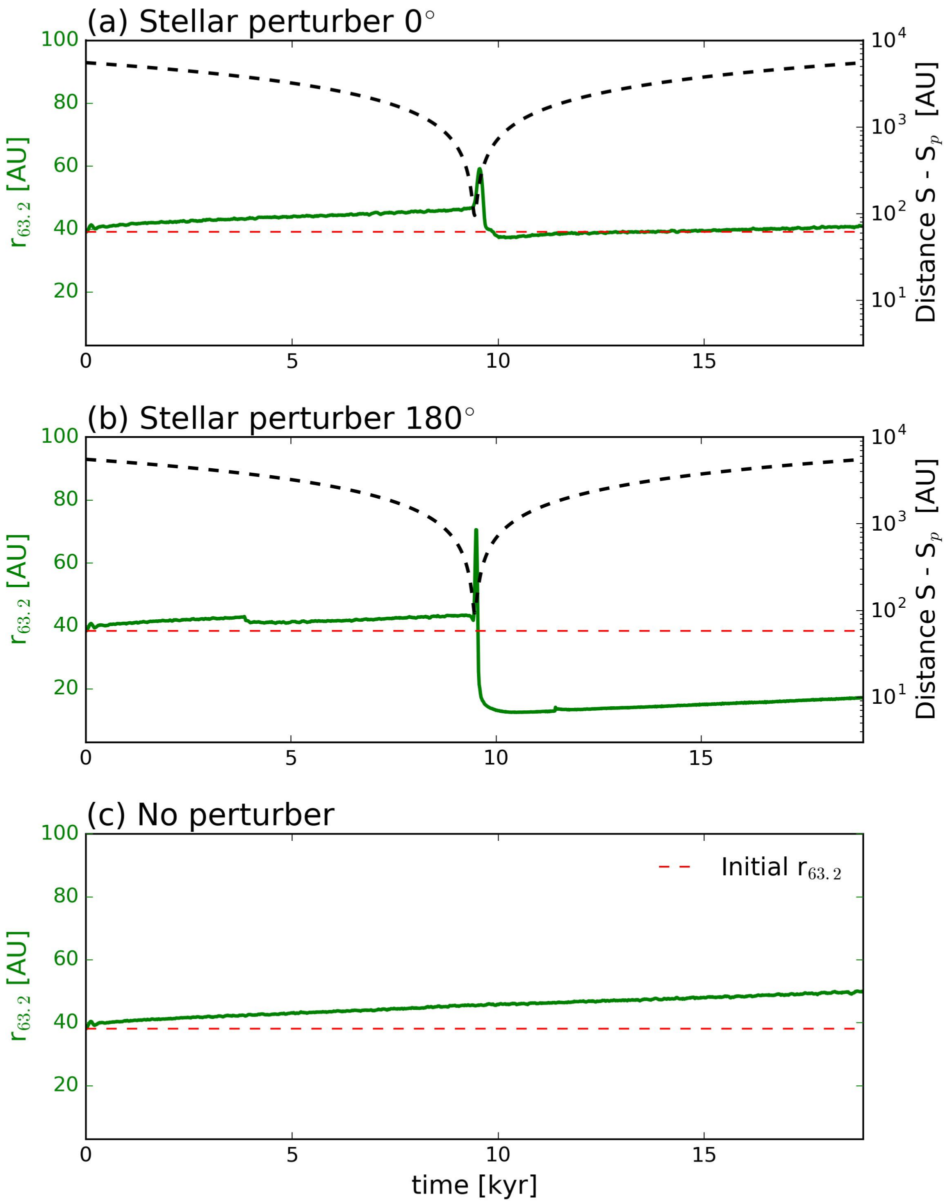

Figure 5.6: Dynamical evolution of the Lagrangian radius of 63.2% of the total mass of the gaseous disk (green solid-line) during a stellar flyby of a perturber of 8 $M_{\odot}$ (black dash-line) in a prograde (a) and retrograde (b) configuration. In (c) the model without stellar perturber.

fusion when it overcomes the final $r_{63.2}$ of the disk of the unperturbed model. In the whole set of our experiments, the 80% of the simulated systems show a final disk truncation after a single close encounter while the remaining 20% show a final diffused disk. Considering the systems with the stellar perturber on prograde orbit ($0°$ and $45°$), the 80% experiences a final disk truncation. The same systems, but with the stellar perturber in retrograde configuration ($135°$ and $180°$), show a final disk truncation in the 86% of the cases. The case when the orbit of the stellar perturber is orthogonal to the planetary system shows that 64% of systems experiences a disk truncation and the remaining 36% a disk diffusion. Although the retrograde case represents the orbital configuration with the smallest interaction time with the planetary system, it shows, in some cases, a more perturbative performance than the prograde case. That's, for instance, the case of the model with a stellar perturber of 0.5 M$_{\odot}$ with the r$_{per}$ 100 AU. As shown in Fig.5.5, the final $r_{63.2}$ of the retrograde case is 37.73% lower than the final $r_{63.2}$ of the unperturbed case and 18.7% lower than the prograde one (see Fig.5.5a). The disk truncation is slightly larger than the periastron of the orbit of the stellar perturber (100 AU) and it slightly increase following a sort of adiabatic expansion. In our experiments, the sharpest disk truncation is in the model with a stellar perturber of 8 M$_{\odot}$ and with the r$_{per}$ $= 100$ AU, in retrograde configuration. As shown in Fig.5.6, its final $r_{63.2}$ is 62.5% lower than the final $r_{63.2}$ of the unperturbed case and it is 50.1% lower than the prograde one. Even with a high mass of the stellar perturber and a close distance to the system at the periastron, the disk is not totally disrupted but just severely truncated.

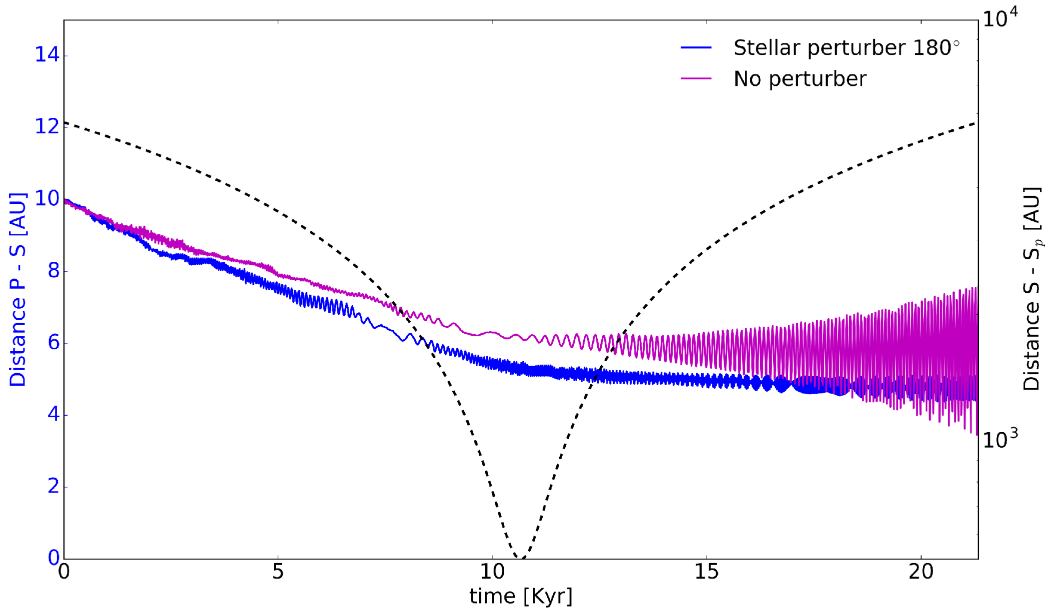

Figure 5.7: Time evolution of the distance between the Jovian planet (P) and the central star (S) of the planetary system (blue solid-line) during a stellar flyby of a perturber of $8\ M_\odot$ (S_p) with $r_{per} = 500$ AU in retrograde orbit (black dash-line). The magenta solid-line represents the unperturbed case.

Jovian planet feedback

The final mean distance $<r>$ of the Jovian planet from the central star and its final mean orbital eccentricity $<e>$ represent the two orbital planetary elements we investigated in our analysis. The 96% of the systems shows a final $<r>$ smaller than the unperturbed case. The dynamical evolution of the unperturbed case is shown in the Fig. 5.4. The 96% of the systems with the stellar perturber in prograde orbit experiences a final decrease of the $<r>$ respect to the unperturbed case; considering the same systems, but in retrograde configuration, the 92% shows a final decrease $<r>$ respect to the unperturbed model. Finally, the 96% of the systems with the orbit of the perturber orthogonal to the planetary system, shows a final decrease of $<r>$ respect to the unperturbed model. This decrease of the $<r>$ indicates a clear planetary migration inward of the Jovian planet, in particular a type II planetary migration as discussed in Chapter 3.2. The longest *migratory journey* in our experiments is in the model with the perturber of 8 $M_{\odot}$ (see fig.5.7) for $r_{per} = 500$ AU, in retrograde configuration: a migration from the initial position of 10 AU to 4.72 AU requires 697 initial orbital periods. Compared to the case without stellar perturber (magenta solid-line in Fig.5.7) we see that both the cases show an initial pure planet-disk interaction but, in the model with the stellar perturber, the perturbed system shows more resiliency then the unperturbed one. Considering the planetary eccentricity, 100% of the systems shows a final eccentricity $<e>$ lower than the value in the model without stellar perturber, regardless if the stellar perturber is in prograde, retrograde or orthogonal configuration. However the orbits of the Jovian planet in the model with massive perturbers, of 3 or 8 $M_{\odot}$, show a final eccentricity slightly greater than the model with a low-mass perturber (0.5, 0.8 or 1 $M_{\odot}$).

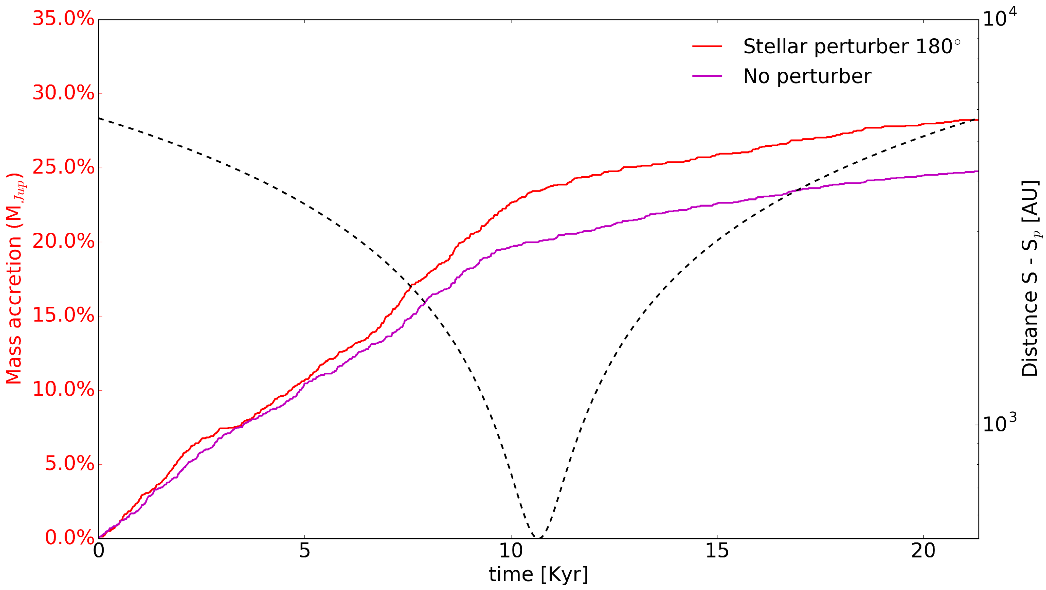

Figure 5.8: Dynamical evolution of the planetary mass accretion of the Jovian planet (red solid-line) during a stellar flyby (black dash-line) of a perturber 8 $M_{\odot}$ (S_p) with a r_{per} 500 AU, in retrograde configuration. The magenta solid-line represents the unperturbed case.

Planetary mass accretion

The planetary mass accretion of the Jovian planet is expressed in % of its initial mass. In our experiments, 14% of the perturbed systems show a final mass accretion more efficient than in the non-perturbed case. The 16% of the systems with the perturber in prograde configuration, the 18% of the systems with the perturber in retrograde configuration and the 28% of the systems with the perturber in orthogonal configuration show a final mass accretion larger than the unperturbed case. The increase of the planetary mass accretion is more evident in the models with massive stellar perturbers, 3 $M_{\odot}$ and 8 $M_{\odot}$ (see Fig. 5.10) than in the models with a low-mass stellar perturber 0.5, 0.8 and 1 $M_{\odot}$ (see Fig.5.9). In the model with the stellar perturber of 8 $M_{\odot}$ (see fig.5.8), for the r_{per} 500 AU we

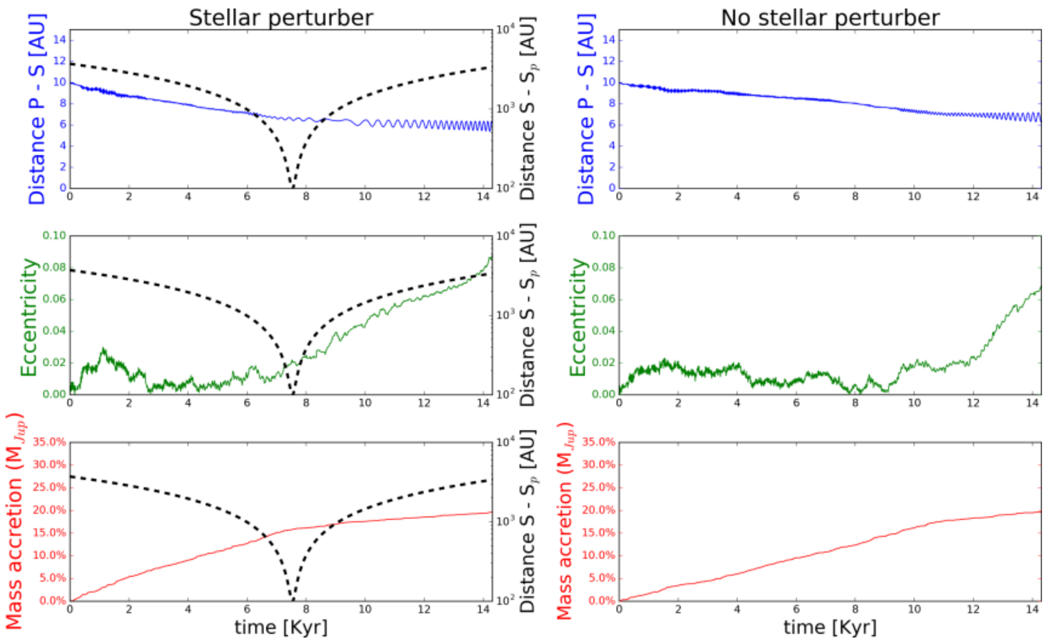

Figure 5.9: Dynamical evolution of the distance (blue-solid line) between the Jovian planet (P) and the central star (S), the planetary eccentricity (green solid line) and the planetary mass accretion (red solid-line) during a stellar flyby of a perturber $0.8\ M_\odot$ (S_p) with a r_{per} 100 AU in retrograde configuration (black dash-line).

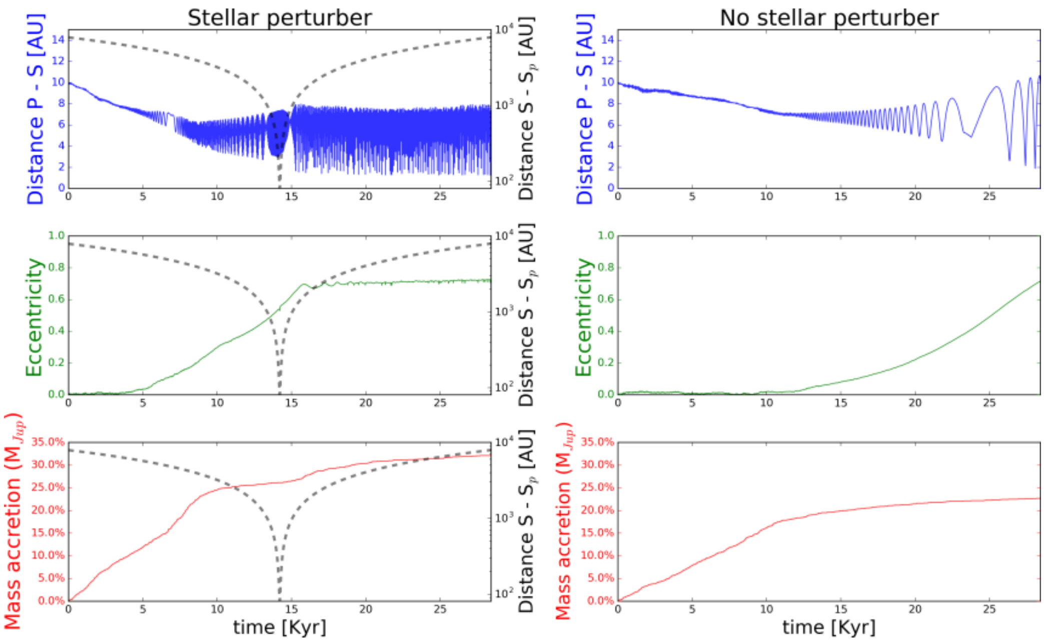

Figure 5.10: Dynamical evolution of the distance (blue-solid line) between the Jovian planet (P) and the central star (S), the planetary eccentricity (green solid line) and the planetary mass accretion (red solid-line) during a stellar flyby of a perturber 8 $M_\odot$ (S_p) with a r_{per} 100 AU in retrograde configuration (black dash-line).

find the final maximum mass planetary accretion in our experiments: 28.23% of the initial mass in M_{Jup}. Before the periastron of the orbit of the stellar perturber (black dash-line), the planetary mass accretion is purely from a planet-disk interaction. After the passage of the perturbing star at its orbital periastron, both for the perturbed case (red solid-line) and the unperturbed one (magenta solid-line), there is a shift of the trend of the evolution of the planetary accretion. In this model the final planetary mass accretion is 16.61% greater than the final unperturbed planetary mass accretion (23.54% of the initial mass in M_{Jup}).

5.2.3 Discussion

In our simulations we investigated stellar encounters towards a young planetary system in prograde, retrograde and orthogonal configurations of 5 stellar perturbers (0.5 $\mathrm{M}_{\odot}$, 0.8 $\mathrm{M}_{\odot}$, 1 $\mathrm{M}_{\odot}$, 3 $\mathrm{M}_{\odot}$, 8 $\mathrm{M}_{\odot}$). Previous works (e.g. Clarke & Pringle 1993, Dai *et al.* 2015, Xiang-Gruess 2016, Picogna & Marzari 2014), found that the final disk shapes are more perturbed by prograde coplanar encounters and found barely perturbed disks after retrograde encounters. In our experiments we obtained that the prograde orbits are not necessarily the most perturbative ones; on the contrary, we observe that relevant perturbations are randomly led by prograde and retrograde encounters. In all cases we see remarkable perturbations after the stellar flyby, regardless the orbital configuration of the stellar perturber. Anyway, we don't see, after the stellar flybys, evidence of spirals or warps as in Cuello *et al.* (2018), but, at the most, a diffuse gaseous halo localized at the edge of the disk. However, we note that Cuello *et al.* (2018), Clarke & Pringle (1993), Dai *et al.* (2015) and Xiang-Gruess (2016) simulated a pure gaseous disks or a gaseous disk with a dusty component: they do not set any planet inside the disk. Possible explanations are both structural (our system is a more compact system due to the presence of a fully formed Jovian planet) and dynamical (we set the same initial velocity of our stellar perturbers for each model we simulated). In Cuello *et al.* (2018) the initial velocity of the stellar perturber is a function of the periastron r_{per} inducing a sort of model dependence of the final outputs in each model simulated.

In future investigations we will set different values of v_∞ for the perturber basing on proper dynamical considerations of the stellar environment. The Jovian planet, initially placed at 10 AU, shows a significant dynamical perturbation at the end of all our simulations, regardless the configuration of the orbit and the mass of the stellar perturber. It moves inward the system and this planetary migration, compared to the model without stellar perturber, is clearly enhanced. We observe a fast migration followed by a slight increase of the final eccentricity. In addition, the final eccentricity is damped more efficiently in the perturbed disk than in the isolated case. The planetary accretion of a Jovian planet in the perturbed system, regardless the orbital configuration of the stellar perturber, is generally lower than the unperturbed case: the perturbed disk slowly accretes the mass of the Jovian planet, although its faster movement inwards. However we do not find any clear correlation between the final planetary parameters and the orbital parameters of the stellar perturber. Regardless the strength of the perturbation, all the systems we simulated remains bound after the gravitational interaction. We experienced, in our hydrodynamic simulations, a resilient disk where the action of the perturbation doesn't affect directly the planet: the disk catalyzes the gravitational perturbation converting the almost impulsive action of the stellar flyby to a softer planet-disk interaction over a timescale longer than the typical time of the single stellar flyby.

These results demonstrate so far that the effects of a stellar flybys shouldn't be considered as impulsive and destructive: when the disk is still present the young planetary system is "protected" by the gaseous disk, remaining bound after the passage of the perturbing star.

Chapter 6

Future perspectives

Focusing the attention on the habitable zone of a planetary system, we might explain potential dynamical constraints about its dynamical evolution, not completely investigated so far. The classical habitable zone (HZ), under careful approximations, can be easily determined using different models (Müller & Haghighipour (2014), Kopparapu *et al.* (2014), Kopparapu *et al.* (2013), Haghighipour & Kaltenegger (2013), Selsis et al.(2007) and Kasting *et al.* (1993)). However, after its definition, crucial questions arise when considering the HZ evolution:

- What's the long-time dynamical evolution of the HZ around single, binary or multiple stellar systems?
- How many planets are expected in the HZ?
- Might a stellar environment affect this delicate strip?
- What's probability to find at least one terrestrial habitable planet inside the HZ taking into account the environmental feedback?

Starting from the theoretical HZs around several and different planetary systems, we may investigate its destiny and the dynamical evolution of their inhabitants (the rocky planets). For each value of the central stellar mass, inside the HZ, we may simulate synthetic populations of habitable rocky planets following, for the initial conditions, the prescriptions in Mordasini *et al.* (2012). In order to consider the influence of the planetary migrations of the giants, a synthetic population of gaseous giant planets will be set in the neighborhood of the snow-line in each planetary system. In addition, for each value of the central stellar mass, we may simulate planetary systems in different ages:

- Young protoplanetary system (gaseous-dusty disk + N planetary seeds)
  - Might the planetary migrations of the giants, in a young planetary system, affect the planetary architecture of the HZ?
  - Does the planet-disk interaction drag materials inward the planetary system perturbing the dynamics of the HZ?
- Middle-aged planetary system (debris disk + formed N planets)
- Evolved planetary system (fully formed N planets e.g. our Solar System).

For each simulated planetary system, the dynamical evolution of the HZ might be studied in isolation, binary and triple stellar systems as shown in the preliminary scheme in Fig. 6.1:

- How does the accretion disc, from the binary companion, affect the dynamics of the planetary HZ?
- How does a circumbinary HZ evolve during the evolution of the binary (or triple) system?

The main outcome in this future perspective will be to extract a final probability P to find at least one terrestrial habitable planet inside the HZ:

$$P(p_{HZ}, p_{pl}) \tag{6.1}$$

where:

- p_{HZ} is the survival rate of the HZ in the range:
  - 0 disrupted HZ
  - 1 unperturbed HZ
- p_{pl} is the survival rate of N initial rocky terrestrial planets inside the final HZ

In the statistical analysis of the arguments p_{HZ} and p_{pl} a new probabilistic argument is considered: the interaction rate with the stellar environment p_{env}:

- 0 Isolated case
- 1 Dense stellar environments

The probability to find at least one terrestrial habitable planet inside the HZ is as important as useful to select, a priori, target lists in sky-surveys aimed to discover habitable planets throughout our Galaxy. Finally, we may integrate our theoretical analysis to the famous and controversial *Drake Equation* where our relation 6.1 represents the fraction of planets that could support life.

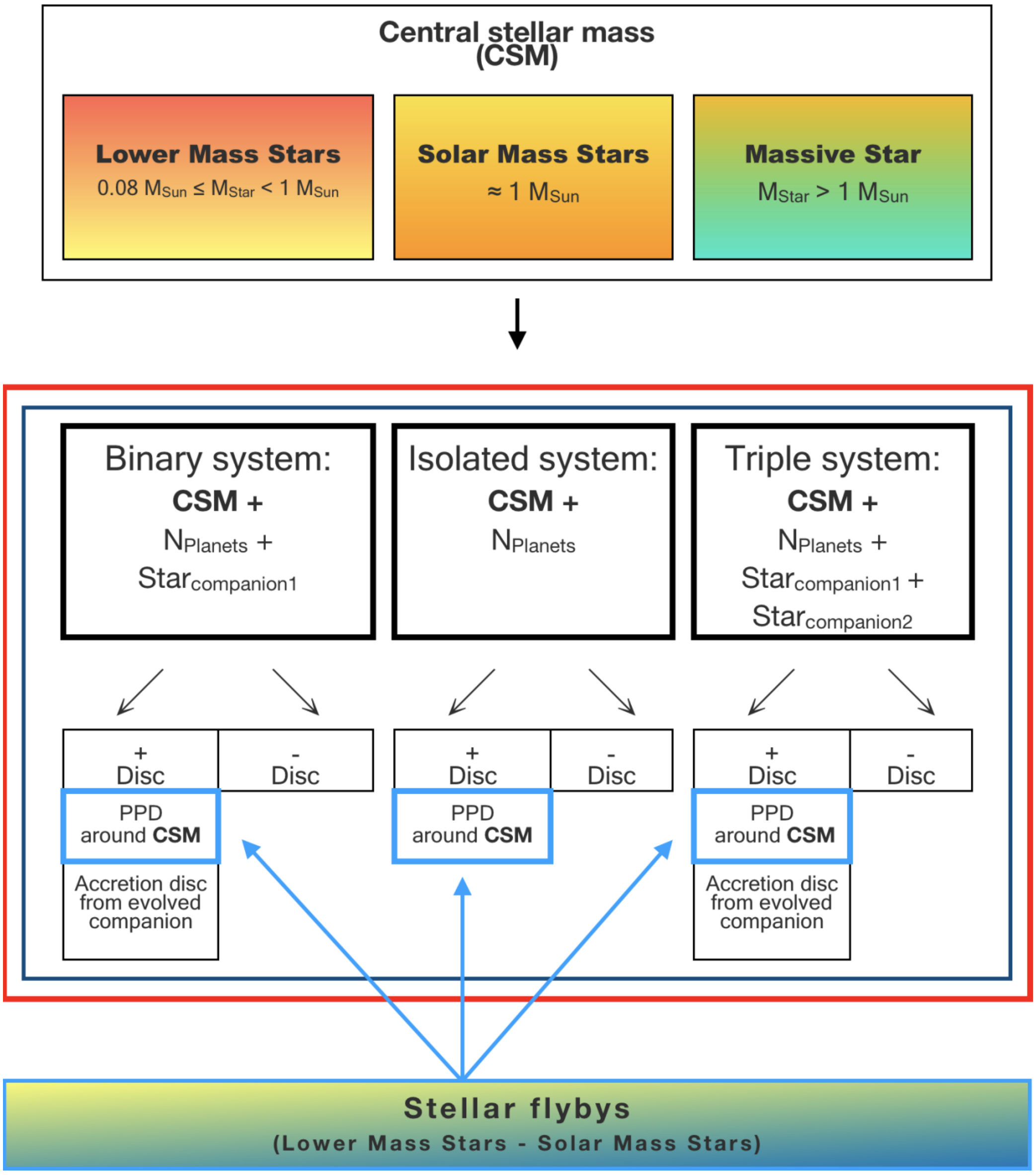

Figure 6.1: Preliminary scheme of the set of numerical simulations. We simulate, around each star in the list of central stellar masses, a planetary system. Each planetary system may evolve in isolation as well as in a more complex structure: binary and/or triple system. In order to simulate both young and evolved planetary systems, we consider the gaseous/dusty component for young protoplanetary disc (PPD) and the pure gaseous component of the accretion disc from evolved companion in binary or triple systems. Finally, for each young PPD we simulate a surrounding stellar environment, typically an open stellar cluster.

Chapter 7

Conclusions

In this thesis I presented the results of our research aimed to the investigation of the dynamical evolution of a young planetary system in a stellar environment. The work is divided into four parts. In the first one we summarize the structures of protoplanetary and planetary systems. The second part describes the dynamical evolution of planetary systems in presence of a low-mass disk and the role of a stellar environment. In the third part we describe the state of the art of numerical simulations of circumstellar structures, focusing on the advantages of the SPH hydrodynamical approach. The last part is dedicated to present our hydrodynamical simulations via the GaSPH code. In this part we study the dynamical evolution of a young planetary system affected by a single stellar flyby as it would happen in a typical open stellar cluster. We consider a system composed by a central star of $1 M_{\odot}$, a gaseous disk (0.009 $M_{\odot}$) containing a completely embedded Jovian planet set on 10 AU circular orbit. We chose 5 stellar perturbators with masses 0.5 $M_{\odot}$, 0.8 $M_{\odot}$, 1 $M_{\odot}$, 3 $M_{\odot}$ and 8 $M_{\odot}$. For each perturber, we changed the distance of the closest approach starting from 100 AU until to 500 AU. We simulated 125 stellar flybys in prograde, retrograde and orthogonal orbital configurations tilting the inclination of each stellar encounter respectively of $0°$, $45°$, $90°$, $135°$ and $180°$. All the systems remain bound after the stellar flyby and we do not report any correlations between the final orbital parameters of the Jovian planet and the orbital parameters of the stellar perturber. However we observe in such experiments that the behaviour of the disk is that of catalyzing the interaction between the planet and the stellar perturber, regardless the orbital configuration of the stellar perturber. It tends to damp the eccentricity reducing the probability of ejection of the planet and, finally, it improves an inwards planetary migration of the Jovian planet.

The first part of this thesis project has been done in collaboration with the Racah Institute of Physics at The Hebrew University of Jerusalem (Israel). In this international collaboration, I studied the initial conditions of the initial set-up of the whole set of our hydrodynamical simulations. It was a crucial phase: the inputs had to be the best compromise between the computational analysis and what really happens in the Universe. The last part of this project has been done in collaboration with the Department of Astrophysics in the Rose Center for Earth and Space at the American Museum of Natural History (USA). I analyzed the out-puts of the simulations of the dynamical evolution of the Jovian planet, investigating the evolution of its planetary distance from the central star, its orbital eccentricity and, finally its mass accretion. Finally, I proposed a potential application of our theoretical investigation on the dynamical evolution of habitable zones in young and evolved planetary system.

Bibliography

[1] Adams F. C., Proszkow E. M., Fatuzzo M., *et al.* , 2006, *Early Evolution of Stellar Groups and Clusters: Environmental Effects on Forming Planetary Systems*, The Astrophysical Journal, 641, 504.

[2] Andrews, S. M., Williams, J. P., 2005, *Circumstellar Dust Disks in Taurus-Auriga: The Submillimeter Perspective*, The Astrophysical Journal, 631, 1134-1160.

[3] Andrews, S. M., Huang, J., Pérez, L. M., *et al.* 2018, *The Disk Substructures at High Angular Resolution Project (DSHARP). I. Motivation, Sample, Calibration, and Overview*, The Astrophysical Journal Letters, 869, L41.

[4] Armitage, J. P., 2010, *Astrophysics of Planet Formation*, Cambridge University Press, ISBN 9780521887458.

[5] Ayliffe B. A., Bate M. R., 2009, *Gas accretion on to planetary cores: three-dimensional self-gravitating radiation hydrodynamical calculations*, Monthly Notices of the Royal Astronomical Society, 393, 49–64.

[6] Barnes, J., Hut, P., 1986, *A hierarchical O(N log N) force-calculation algorithm*, Nature, 324, 446-449.

[7] Barnes, J. E., 1986, *The Use of Supercomputers in Stellar Dynamics*, Springer, 175-180.

[8] Bate, M. R., 2018, *On the diversity and statistical properties of protostellar discs*, Monthly Notices of the Royal Astronomical Society, 475, 5618.

[9] Bate, M. R., Bonnell, I. A., 1997, *Accretion during binary star formation - II. Gaseous accretion and disc formation*, Monthly Notices of the Royal Astronomical Society, 285, 33-48.

[10] Bate, M. R., Bonnell, I. A., Price, N. M., 1995, *Modelling accretion in protobinary systems*, Monthly Notices of the Royal Astronomical Society, 277, 362-376.

[11] Beuzit J. L., Vigan A., Mouillet D., 2019, *SPHERE: the exoplanet imager for the Very Large Telescope*, Astronomy & Astrophysics, Accepted.

[12] Binney, J., Tremaine, S., 1987, *Galactic dynamics*, Princeton University Press.

[13] Boss, A. P., 2003, *Rapid Formation of Outer Giant Planets by Disk Instability*, The Astrophysical Journal, 599, 577-581.

[14] Brasser R., Morbidelli A., 2013, *Oort cloud and Scattered Disk formation during a late dynamical instability in the Solar System*, Icarus, 225, 40-49.

[15] Breslau A., Vincke K., Pfalzner S., 2017, *From star-disc encounters to numerical solutions for a subset of the restricted three-body problem*, Astronomy & Astrophysics, 599, A91.

[16] Brucalassi, A. , Pasquini, L., Saglia, R., *et al.* 2016, *Search for giant planets in M67, III. Excess of hot Jupiters in dense open clusters*, Astronomy & Astrophysics, 592, L1.

[17] Capobianco C. C., Duncan M., Levison H. F., 2011, *Planetesimal-driven planet migration in the presence of a gas disk*, Icarus, 211, 819-831.

[18] Christiaens, V., Casassus, S., Perez, S., van der Plas, G., & Menard, F. 2014, *Spiral Arms in the Disk of HD 142527*, The Astrophysical Journal Letters, 785, L12.

[19] Clarke C. J., Pringle J. E., 1993, *Accretion disc response to a stellar fly-by*, Monthly Notices of the Royal Astronomical Society, 261, 190-202.

[20] Craig, J., & Krumholz, M. R. 2013, *Close Stellar Encounters in Young, Substructured, Dissolving Star Clusters: Statistics and Effects on Planetary Systems*, The Astrophysical Journal, 769, 150.

[21] Cresswell P., Nelson R. P., 2006, *On the evolution of multiple protoplanets embedded in a protostellar disc*, Astronomy & Astrophysics, 450, 833-853.

[22] Cuello, N., Dipierro, G., *et al.* 2019, *Flybys in protoplanetary discs: I. Gas and dust dynamics*, Monthly Notices of the Royal Astronomical Society, 483, 4114 - 4139.

[23] Cumming, A., Marcy, G. W., & Butler, R. P. 1999, *The Lick Planet Search: Detectability and Mass Thresholds*, The Astrophysical Journal, 526, 890-915.

[24] D'Alessio, P., Calvet, N., Hartmann, L., *et al.* 1999, *Accretion Disks around Young Objects. II. Tests of Well-mixed Models with ISM Dust*, The Astrophysical Journal, 527, 893-909.

[25] D'Angelo, G., Henning, T., Kley, W., 2002, *Nested-grid calculations of disk-planet interaction*, Astronomy & Astrophysics, 385, 647-670.

[26] D'Angelo, G., Kley, W., Henning T., 2003, *Orbital Migration and Mass Accretion of Protoplanets in Three-dimensional Global Computations with Nested Grids*, The Astrophysical Journal, 586, 540-561.

[27] D'Angelo, G., Lubow, S. H. , 2010, *Three-dimensional Disk-Planet Torques in a Locally Isothermal Disk*, The Astrophysical Journal, 724, 730-747.

[28] Dai F., Facchini S., Clarke C. J., Haworth T. J., 2015, *A tidal encounter caught in the act: modelling a star-disc fly-by in the young RW Aurigae system*, Monthly Notices of the Royal Astronomical Society, 449, 1996-2009.

[29] Davies, M. B., Adams, F. C., Armitage, P., *et al.*, 2014, *The Long-Term Dynamical Evolution of Planetary Systems*, Protostars and Planets VI, Henrik Beuther, Ralf S. Klessen, Cornelis P. Dullemond, and Thomas Henning (eds.), University of Arizona Press, Tucson, 914, 787-808.

[30] Dawson, R. I., Johnson, J. A. 2018, *Origins of Hot Jupiters*, Annual Review Astronomy & Astrophysics, 56, 175-221.

[31] Deeg, H., 1998, *Photometric Detection of Extrasolar Planets by the Transit-Method*, Brown dwarfs and extrasolar planets, Proceedings of a Workshop held in Puerto de la Cruz, Tenerife, Spain, 17-21 March 1997, ASP Conference Series, 134.

[32] Deienno R., Morbidelli A., Gomes R.S., Nesvorny D., 2017, *Constraining the Giant Planets: Initial Configuration from Their Evolution: Implications for the Timing of the Planetary Instability*, The Astronomical Journal, 153, 153.

[33] Demidova, T. V., Sotnikova, N. Y., Grinin, V. P., 2010, *Bimodal Brightness Oscillations in Models of Young Binary Systems*, Astronomy Letters, 2010, 36, 6, 422-29.

[34] Donati, J. F., *et al.* 2016, *A hot Jupiter orbiting a 2-million-year-old solar-mass T Tauri star*, Nature, 534, 662.

[35] Dukes, D., Krumholz, M. R., 2012, *Was the Sun Born in a Massive Cluster?* The Astrophysical Journal, 754, 56.

[36] Dullemond, C. P., Hollenbach, D., Kamp, I., D'Alessio, P. 2007, *Models of the Structure and Evolution of Protoplanetary Disk*, Protostars and Planets V, B. Reipurth, D. Jewitt, and K. Keil (eds.), University of Arizona Press, Tucson, 951, 555-572.

[37] Duquennoy, A., Mayor, M., 1991, *Multiplicity among solar-type stars in the solar neighbourhood. II - Distribution of the orbital elements in an unbiased sample*, Astronomy & Astrophysics, 248, 485-524.

[38] Farouki, R., Shapiro, S. L. 1981, *Computer simulations of environmental influences on galaxy evolution in dense clusters. II - Rapid tidal encounters*, The Astrophysical Journal, 243, 32-41.

[39] Fernandez J.A., Ip W.H., 1984, *Some dynamical aspects of the accretion of Uranus and Neptune - The exchange of orbital angular momentum with planetesimals*, Icarus, 58, 109-120.

[40] Fregeau J. M., Cheung P., Portegies Zwart S. F., Rasio F. A., 2004, *Stellar collisions during binary-binary and binary-single star interactions*, Monthly Notices of the Royal Astronomical Society, 352, 1.

[41] Garcia, P. J. V., 2011, *Physical Processes in Circumstellar Disks around Young Stars*, University of Chicago Press, ISBN 9780226282282.

[42] Gingold, R. A., Monaghan, J. J., 1977, *Smoothed particle hydrodynamics - Theory and application to non-spherical stars*, Monthly Notices of the Royal Astronomical Society, 181, 375-389.

[43] Goldreich, P., Tremaine, S., 1980, *Disk-satellite interactions*, The Astrophysical Journal, 241, 425-44.

[44] Grady, C. A., Polomski, E. F., Henning, T., *et al.* 2001, *The Disk and Environment of the Herbig Be Star HD 100546*, The Astrophysical Journal, 122, 3396-3406.

[45] Grinin, V. P., Demidova, T. V., & Sotnikova, N. Y., 2010, *Modulation of Circumstellar Extinction in a Young Binary System with a Low-Mass Companion in a Noncoplanar Orbit*, Astronomy Letters, 2010, 36, 11, 808-815.

[46] Gullbring, E., Hartmann, L., *et al.* 1998, *Disk Accretion Rates for T Tauri Stars*, The Astrophysical Journal, 492, 323-341.

[47] Haghighipour, N., Kaltenegger, L., 2013, *Calculating the Habitable Zone of Binary Star Systems II: P-Type Binaries*, The Astrophysical Journal, 777, 166.

[48] Haisch, Jr., K. E., Lada, E. A., Lada, C. J. 2001, *Disk Frequencies and Lifetimes in Young Clusters*, The Astrophysical Journal, 553, L153-L156.

[49] Hall, S. M., 1997, *Circumstellar disc density profiles: a dynamic approach*, Monthly Notices of the Royal Astronomical Society, 287, 148-154

[50] Hartmann, W. K., Davis, D. R. 1975, *Satellite-sized planetesimals and lunar origin*, Icarus, 24, 504-514.

[51] Hartmann, L., Hewett, R., Calvet, N., 1994, *Magnetospheric accretion models for T Tauri stars*, Astrophysical Journal, 426, 669-687.

[52] Hartmann, L., Calvet, N., *et al.* 1998, *Accretion and the Evolution of T Tauri Disks*, The Astrophysical Journal, 495, 385-400.

[53] Hashimoto, J., Tamura, M., Muto, T., *et al.* 2011, *Direct Imaging of Fine Structures in Giant Planet Forming Regions of the Protoplanetary Disk around AB Aurigae*, The Astrophysical Journal Letters, 729, L17.

[54] Hayashi C., 1981, *Structure of the Solar Nebula, Growth and Decay of Magnetic Fields and Effects of Magnetic and Turbulent Viscosities on the Nebula*, Progress of Theoretical Physics Supplement, 70, 35-53.

[55] Heller, C. H., 1995, *Encounters with Protostellar Disks. II. Disruption and Binary Formation*, The Astrophysical Journal, 455, 252-259.

[56] Hernquist, L., Katz, N. 1989, *TREESPH - A unification of SPH with the hierarchical tree method*, The Astrophysical Journal Supplement Series, 70, 419-446.

[57] Hernquist, L. 1987, *Performance characteristics of tree codes*, Astrophysical Journal Supplement Series, 64, 715-734.

[58] Hillenbrand, L. A., 1997, *On the Stellar Population and Star-Forming History of the Orion Nebula Cluster*, Astronomical Journal, 113, 1733-1768.

[59] Ida, S., Lin, D. N. C. 2005, *Toward a Deterministic Model of Planetary Formation. III. Mass Distribution of Short-Period Planets around Stars of Various Masses*, The Astrophysical Journal, 626, 1045-1060.

[60] Jang-Condell H., Sasselov D. D., 2005, *Type I Migration in a Nonisothermal Protoplanetary Disk* The Astrophysical Journal, 619, 1123-1131.

[61] Jiménez-Torres, J.J., Pichardo, B., Lake, G., *et al.* 2013, *Habitability in different Milky Way stellar environments: a stellar interaction dynamical approach*, Astrobiology, 13, 491-509.

[62] Kasting, J. F., Whitmire, D. P., *et al.* 1993, *Habitable zones around main sequence stars*, Icarus, 101, 108-128.

[63] Kenyon, S. J., Hartmann, L., 1987, *Spectral Energy Distributions of T-Tauri Stars: Disk Flaring and Limits on Accretion*, The Astrophysical Journal, 323, 714-733.

[64] Kirsh D.R., Duncan M., Brasser R., Levison H.F. , 2009, *Simulations of planet migration driven by planetesimal scattering*, Icarus, 199, 197-209.

[65] Kley, W., Nelson, R. P., L., 2012, *Planet-Disk Interaction and Orbital Evolution*, Annual Review of Astronomy and Astrophysics, 50, 211-249.

[66] Kley, W., Nelson, R. P. 2008, *Planet formation in binary stars: the case of γ Cephei*, Astronomy & Astrophysics, 486, 617-628.

[67] Kobayashi, H., Ida, S. 2001, *The Effects of a Stellar Encounter on a Planetesimal Disk*, Icarus, 153, 416-429.

[68] Kopparapu, R. K., Ramirez, R., et. al, 2013, *Habitable Zones around Main-sequence Stars: New Estimates*, The Astrophysical Journal, 765, 131.

[69] Kopparapu, R. K., Ramirez, R., et. al, 2014, *Habitable Zones around Main-sequence Stars: Dependence on Planetary Mass*, The Astrophysical Journal Letters, 787, L29.

[70] Larwood, J. D., Papaloizou, J. C. B.,1997, *The hydrodynamical response of a tilted circumbinary disc: linear theory and non-linear numerical simulations*, Monthly Notices of the Royal Astronomical Society, 285, 288-302.

[71] Laughlin G., Steinacker A., Adams F. C., 2004, *Type I Planetary Migration with MHD Turbulence* The Astrophysical Journal, 608, 489-496

[72] Laughlin G., Adams F. C., 2000, *The Frozen Earth: Binary Scattering Events and the Fate of the Solar System*, Icarus, 145, 614.

[73] Levison H.F., Morbidelli A., Tsiganis K., *et al.* 2011, *Late Orbital Instabilities in the Outer Planets Induced by Interaction with a Selfgravitating Planetesimal Disk*, The Astronomical Journal, 142, 152.

[74] Levison, H. F., Morbidelli, A., Dones, L., 2004, *Sculpting the Kuiper Belt by a Stellar Encounter: Constraints from the Oort Cloud and Scattered Disk*, The Astronomical Journal, 128, 2553-2563.

[75] Lin, D. N. C., Papaloizou, J., 1986, *On the tidal interaction between protoplanets and the primordial solar nebula. II - Self-consistent nonlinear interaction*, The Astrophysical Journal, 307, 395-409.

[76] Lin, D. N. C., Papaloizou, J., 1979, *Tidal torques on accretion discs in binary systems with extreme mass ratios*, Monthly Notices of the Royal Astronomical Society, 186, 799-812.

[77] Lucy, L. B. 1977, *A numerical approach to the testing of the fission hypothesis*, The Astrophysical Journal, 82, 1013-1024.

[78] Lynden-Bell, D. & Pringle, J. E., 1974, *The evolution of viscous discs and the*

origin of the nebular variables, Monthly Notices of the Royal Astronomical Society, 168, 603-637.

[79] Malmberg, D., Davies, M. B., & Heggie, D. C. 2011, *The effects of fly-bys on planetary systems,* Monthly Notices of the Royal Astronomical Society, 411, 859-877.

[80] Marzari, F., Scholl, H., Thebault, P., Baruteau, C. 2009, *On the eccentricity of self-gravitating circumstellar disks in eccentric binary systems*, Astronomy & Astrophysics, 508, 1493-1502.

[81] Masset F. S., D'Angelo G., Kley W., 2006, *On the migration of protogiant solid cores* The Astrophysical Journal, 652, 730-745.

[82] Mayer, L., Quinn, T., *et al.* 2002, *Formation of giant planets by fragmentation of protoplanetary disks*, Science, 298, 1756-1759.

[83] Mayor M., Queloz D., 1995, *A Jupiter-mass companion to a solar-type star*, Nature, 378, 355.

[84] Meglicki, D. Wickramasinghe, Bicknell, G. V., 1993, *Three-Dimensional Structure of Truncated Accretion Discs in Close Binaries*, Monthly Notices of the Royal Astronomical Society, 264, 691.

[85] Melita, M. D., Larwood, J., Collander-Brown, S., *et al.* 2002, *Proceedings of Asteroids, Comets, Meteors - ACM 2002,* International Conference, 29 July - 2 August 2002, Berlin, Germany, ISBN 9290928107.

[86] Menou K., Goodman J., 2004 *Low-Mass Protoplanet Migration in T Tauri α-Disks* The Astrophysical Journal, 606, 520-531.

[87] Monaghan, J. J. & Lattanzio, J. C., 1985, *A refined particle method for astrophysical problems*, Astronomy & Astrophysics, 149,135-143.

[88] Monaghan, J. J., Gingold, R. A. 1983, *Shock Simulation by the Particle Method SPH*, Journal of Computational Physics, 52, 374-389.

[89] Monaghan, J. J. 1985, *Particle methods for hydrodynamics*, Computer Physics Reports, 3, 71-124.

[90] Monaghan, J. J. 1988, *An introduction to SPH*, Computer Physics Communications, 48, 89-96.

[91] Monaghan, J. J. 1989, *On the problem of penetration in particle methods*, Journal of Computational Physics, 82, 1-15.

[92] Monaghan, J. J. 1992, *Smoothed particle hydrodynamics*, Annual Review Astronomy & Astrophysics, 30, 543-574.

[93] Monaghan, J. J. 2005, *Smoothed particle hydrodynamics*, Reports on Progress in Physics, 68, 1703-1759.

[94] Morbidelli A., Tsiganis K., Crida A., Levison H.F., Gomes R., 2007, *Dynamics of the Giant Planets of the Solar System in the Gaseous Protoplanetary Disk and Their Relationship to the Current Orbital Architecture*, The Astronomical Journal, 134, 1790-1798.

[95] Morbidelli A., Brasser R., Gomes R., *et al.* 2010, *Evidence from the Asteroid Belt for a Violent Past Evolution of Jupiter's Orbit*, The Astronomical Journal, 140, 1391-1401.

[96] Mordasini, C., Alibert Y., Benz, *et al.* 2012, *Extrasolar planet population synthesis . IV. Correlations with disk metallicity, mass, and lifetime*, Astronomy & Astrophysics, 541, A97.

[97] Morris, J. P. & Monaghan, J. J. 1997, *A Switch to Reduce SPH Viscosity*, Journal of Computational Physics, 136, 41-50.

[98] Müller, T. W. A., Haghighipour, N., 2014, *Calculating the Habitable Zones of Multiple Star Systems with a New Interactive Web Site*, The Astrophysical Journal, 782, 26.

[99] Nelson, A. F., Benz, W., & Ruzmaikina, T. V. 2000, *Dynamics of Circumstellar Disks. II. Heating and Cooling*, The Astronomical Journal, 529, 357-390.

[100] Nelson, A. F., 2000, *Planet Formation is Unlikely in Equal-Mass Binary Systems with A $\sim$50 AU*, The Astrophysical Journal, 537, L65-L68.

[101] Nesvorny D., Vokrouhlicky D., Morbidelli A., 2007, *Capture of Irregular Satellites during Planetary Encounters*, The Astronomical Journal, 133, 1962-1976.

[102] Nesvorny D., Vokrouhlicky D., 2009, *Chaotic Capture of Neptune Trojans*, The Astronomical Journal, 137, 5003-5011.

[103] Nesvorny D., Morbidelli A., 2012, *Statistical Study of the Early Solar System's Instability with Four, Five, and Six Giant Planets*, The Astronomical Journal, 144, 117.

[104] Nesvorny D., Vokrouhlicky D., Morbidelli A., 2013, *Capture of Trojans by Jumping Jupiter*, The Astrophysical Journal, 768, 45.

[105] Nesvorny D., 2015, *Evidence for Slow Migration of Neptune from the Inclination Distribution of Kuiper Belt Objects*, The Astronomical Journal, 150, 73.

[106] Nesvorny D., 2015, *Jumping Neptune Can Explain the Kuiper Belt Kernel*, The Astronomical Journal, 150, 68.

[107] Nesvorny D., Vokrouhlicky D., Dones L., et al, 2017, *Origin and Evolution of Short-Period Comets*, The Astrophysical Journal, 845, 27.

[108] Olczak, C., Pfalzner, S., Spurzem, R., 2006, *Encounter-triggered Disk Mass Loss in the Orion Nebula Cluster*, The Astrophysical Journal, 642, 1140-1151.

[109] Paardekooper S. J., Mellema G., 2006, *Dust flow in gas disks in the presence of embedded planets*, Astronomy & Astrophysics, 453, 1129-1140.

[110] Paardekooper, S. J., Thébault, P., Mellema, G., 2008, *Planetesimal and gas dynamics in binaries*, Monthly Notices of the Royal Astronomical Society, 386, 973-988.

[111] Palla, F., Stahler, S. W., 2000, *Accelerating Star Formation in Clusters and Associations*, The Astrophysical Journal, 540, 255-270.

[112] Papaloizou, J. C. B., Pringle, J. E., 1984, *The dynamical stability of differentially rotating discs with constant specific angular momentum*, Monthly Notices of the Royal Astronomical Society, 208, 721-750.

[113] Pfalzner, S., Umbreit, S., Henning, T., 2005, *Disk-Disk Encounters between Low-Mass Protoplanetary Accretion Disks*, The Astrophysical Journal, 629, 526-534.

[114] Pfalzner, S., Vogel, P., Scharwächter, J., Olczak, C., 2005, *Parameter study of star-disc encounters*, Astronomy & Astrophysics, 437, 967-976.

[115] Picogna G., Marzari F., 2014, *Effects of stellar flybys on planetary systems: 3D modeling of the circumstellar disk's damping effects*, Astronomy & Astrophysics, 564, A28.

[116] Picogna, G. & Marzari, F., 2013, *Three-dimensional modeling of radiative disks in binaries*, Astronomy & Astrophysics, 556, A148, 15.

[117] Pinto, L. D., Capuzzo-Dolcetta, R., et al, 2019, *Self-gravitating disks in binary systems: an SPH approach, I. Implementation of the code and reliability tests*, Astronomy & Astrophysics, 628, A82

[118] Pollack J. B., Hubickyj O., Bodenheimer P., *et al.* 1996, *Formation of the Giant Planets by Concurrent Accretion of Solids and Gas*, Icarus, 124, 62-85.

[119] Price, D. J. & Monaghan, J. J. 2007, *An energy-conserving formalism for adaptive gravitational force softening in smoothed particle hydrodynamics and N-body codes*, Monthly Notices of the Royal Astronomical Society, 374, 1347-1358.

[120] Pringle, J. E., 1981, *Accretion discs in astrophysics*, Annual Review Astronomy & Astrophysics, 19, 137-162.

[121] Punzo, D., Capuzzo-Dolcetta, R., Portegies Zwart, S., 2014, *The secular evolution of the Kuiper belt after a close stellar encounter*, Monthly Notices of the Royal Astronomical Society, 444, 2808-2819.

[122] Rice, W. K. M., & Armitage P. J., 2009, *Time-dependent models of the structure and stability of self-gravitating protoplanetary discs*, Monthly Notices of the Royal Astronomical Society, 396, 2228-2236.

[123] Roig F., Nesvorny D., 2015, *The Evolution of Asteroids in the Jumping-Jupiter Migration Model*,
The Astronomical Journal, 150, 186.

[124] Rosotti, G. P., Dale, J. E., De Juan Ovelar, M., *et al.* 2014, *Protoplanetary disc evolution affected by star–disc interactions in young stellar clusters*, Monthly Notices of the Royal Astronomical Society, 441, 2094-2110.

[125] Rosswog, S., Davies, M. B., Thielemann, F.-K., Piran, T., 2000, *Merging neutron stars: asymmetric systems*, Astronomy & Astrophysics, 360, 171-184.

[126] Scharwächter, J., Eckart, A., Pfalzner, S., *et al.* 2007, *The nearby QSO host I Zw 1: the stellar disk and adjacent objects*, Astronomy & Astrophysics, 469, 913–923.

[127] Selsis, F., Kasting, J. F., *et al.* 2007, *Habitable planets around the star Gl 581?*, Astronomy & Astrophysics, 476, 1373 -1387.

[128] Shakura, N. I., Sunyaev, R. A., 1973, *Black holes in binary systems. Observational appearance*, Astronomy & Astrophysics, 24, 337-355.

[129] Skrutskie, M. F., Dutkevitch, D., Strom, S. E., *et al.* 1990, *A Sensitive 10-Micron Search for Emission Arising from Circumstellar Dust Associated with Solar-Type Pre-Main-Sequence Stars*, The Astrophysical Journal, 99, 1187-1195.

[130] Springel, V. & Hernquist, L., 2002, *Cosmological smoothed particle hydrodynamics simulations: the entropy equation*, Monthly Notices of the Royal Astronomical Society, 333, 649-664.

[131] Takakuwa, S., Saigo, K., Matsumoto, T., *et al.* 2014, *Spiral Arms, Infall, and*

Misalignment of the Circumbinary Disk from the Circumstellar Disks in the Protostellar Binary System L1551 NE, The Astrophysical Journal, 837, 86-100.

[132] Tanaka, H., Takeuchi T, Ward, W. R., 2002 *Three-Dimensional Interaction between a Planet and an Isothermal Gaseous Disk. I. Corotation and Lindblad Torques and Planet Migration*, The Astrophysical Journal, 565, 1257-1274.

[133] Terquem C. E. J. M. L. J., 2003, *Stopping inward planetary migration by a toroidal magnetic field*, Monthly Notices of the Royal Astronomical Society, 341, 1157-1173.

[134] Triaud, A., 2016, *Exoplanets: Migration of giants*, Nature, 537, 496-497.

[135] Toomre, A., Toomre, J., 1972, *Galactic Bridges and Tails*, The Astrophysical Journal, 178, 623-666.

[136] Toomre, A., 1964, *On the gravitational stability of a disk of stars*, The Astrophysical Journal, 139, 1217-1238.

[137] Tsiganis K., Gomes R., Morbidelli A., *et al.* 2005, *Origin of the orbital architecture of the giant planets of the Solar System*, Nature, 435, 459-461.

[138] Weinberger, A. J., Becklin, E. E., Schneider, G., *et al.* 1999, *The Circumstellar Disk of HD 141569 Imaged with NICMOS*, The Astrophysical Journal, 525, L53-L56.

[139] Wolk, S. J., Walter, F. M., 1996, *A Search for Protoplanetary Disks Around Naked T Tauri Stars*, The Astrophysical Journal, 111, 2066.

[140] Xiang-Gruess M., 2016, *Generation of highly inclined protoplanetary discs through single stellar flybys*, Monthly Notices of the Royal Astronomical Society, 455, 3086-3100.

[141] Xiang-Gruess, M., Papaloizou, J. C. B., 2013, *Interaction between massive planets on inclined orbits and circumstellar discs*, Monthly Notices of the Royal Astronomical Society, 431, 1320-1336.

Appendices

Appendix A

Stellar perturber of 1 $M_\odot$

Below we list the plots of the model of the stellar perturber of 1 $M_\odot$ and, on the right side of each figure, the plots of the unperturbed model. We plot, for each inclination and periastron of the orbit of the stellar perturber of 1 $M_\odot$:

- The time evolution of the distance between the Jovian planet and the central star.
- The time evolution of the planetary eccentricity.
- The time evolution of the planetary mass accretion.

The plots of the models of the stellar perturbers of 0.5 $M_\odot$, 0.8 $M_\odot$, 3 $M_\odot$ and 8 $M_\odot$ are available on this site: "On Dynamical Evolution of a young planetary system"

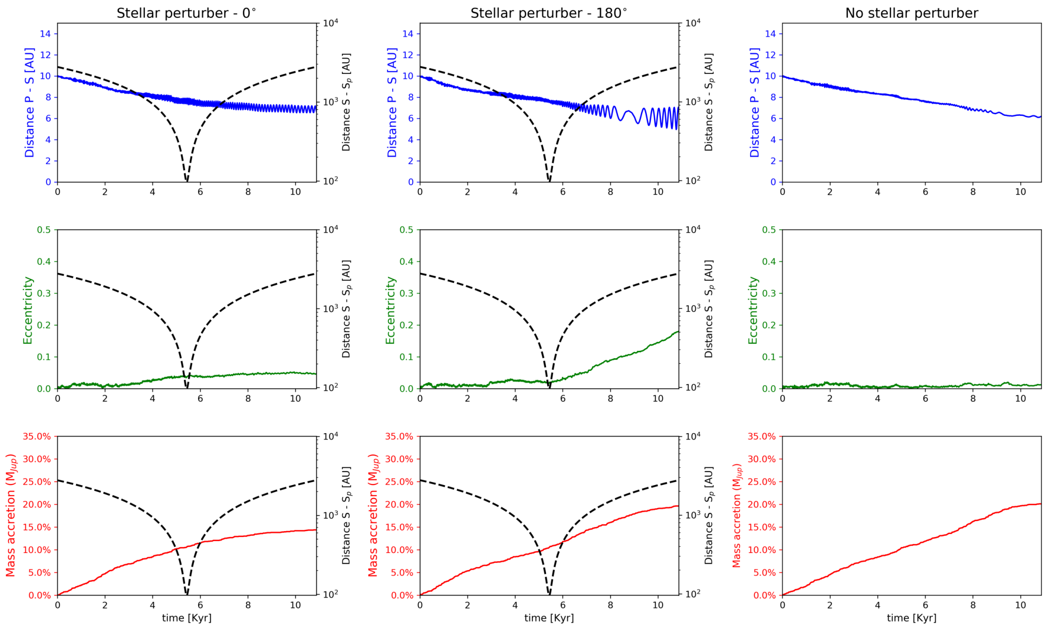

Figure A.1: Dynamical evolution of the distance (blue-solid line) between the Jovian planet (P) and the central star (S), the planetary eccentricity (green solid line) and the planetary mass accretion (red solid-line) during a stellar flyby of a perturber 1 $M_\odot$ (S_p) with a r_{per} 100 AU and orbital inclination $0°$ and $180°$ (black dash-line).

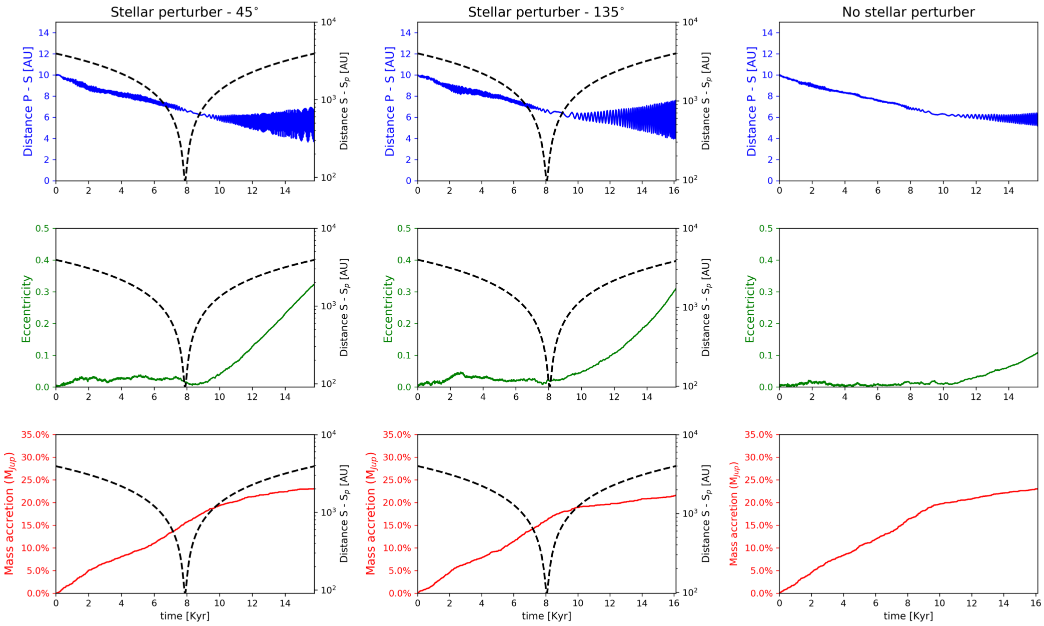

Figure A.2: Dynamical evolution of the distance (blue-solid line) between the Jovian planet (P) and the central star (S), the planetary eccentricity (green solid line) and the planetary mass accretion (red solid-line) during a stellar flyby of a perturber 1 $M_{\odot}$ (S_p) with a r_{per} 100 AU and orbital inclination $45°$ and $135°$ (black dash-line).

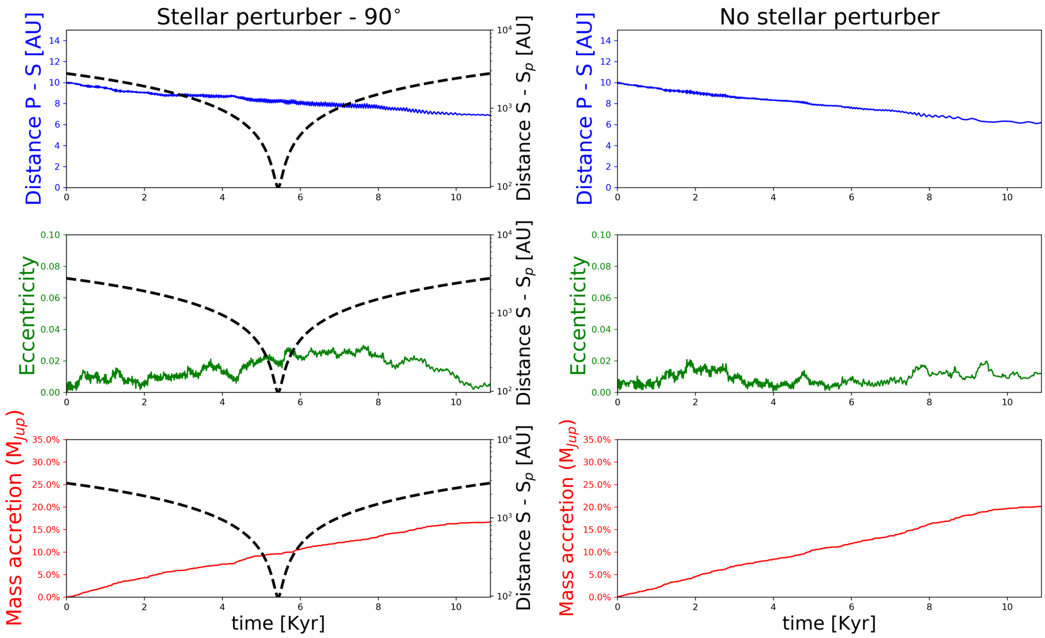

Figure A.3: Dynamical evolution of the distance (blue-solid line) between the Jovian planet (P) and the central star (S), the planetary eccentricity (green solid line) and the planetary mass accretion (red solid-line) during a stellar flyby of a perturber 1 M$_\odot$ (S_p) with a r_{per} 100 AU and orbital inclination $90°$ (black dash-line).

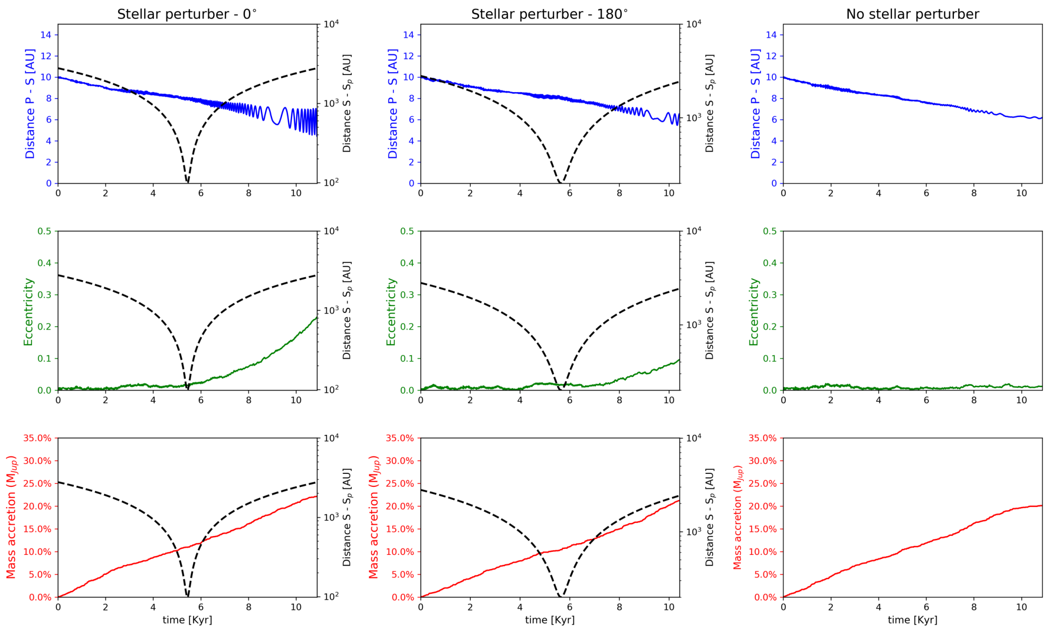

Figure A.4: Dynamical evolution of the distance (blue-solid line) between the Jovian planet (P) and the central star (S), the planetary eccentricity (green solid line) and the planetary mass accretion (red solid-line) during a stellar flyby of a perturber 1 $M_\odot$ (S_p) with a r_{per} 200 AU and orbital inclination 0° and 180° (black dash-line).

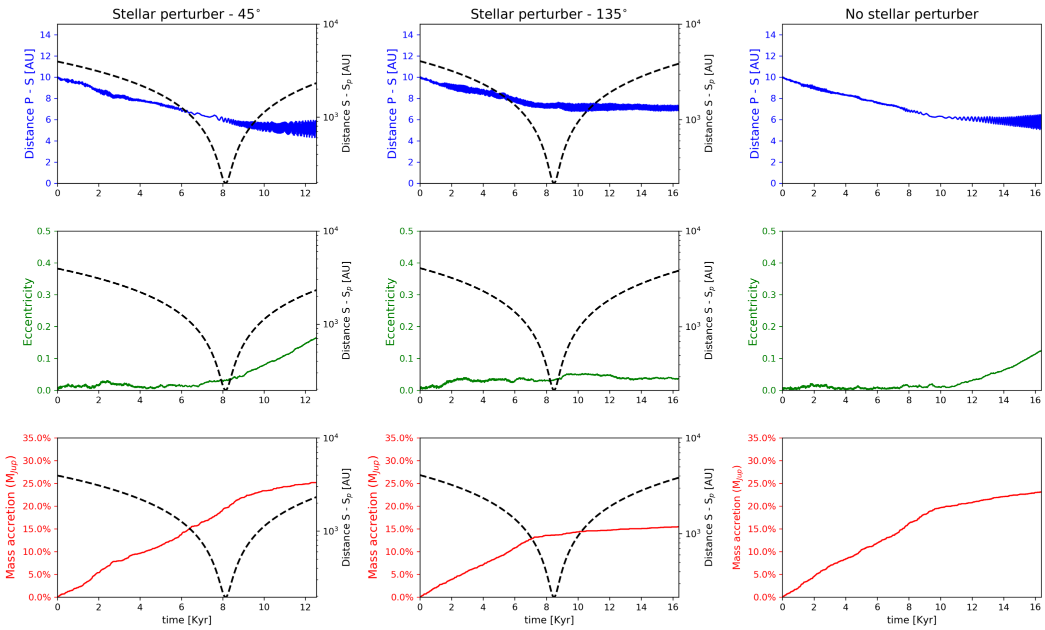

Figure A.5: Dynamical evolution of the distance (blue-solid line) between the Jovian planet (P) and the central star (S), the planetary eccentricity (green solid line) and the planetary mass accretion (red solid-line) during a stellar flyby of a perturber 1 $M_\odot$ (S_p) with a r_{per} 200 AU and orbital inclination 45° and 135° (black dash-line).

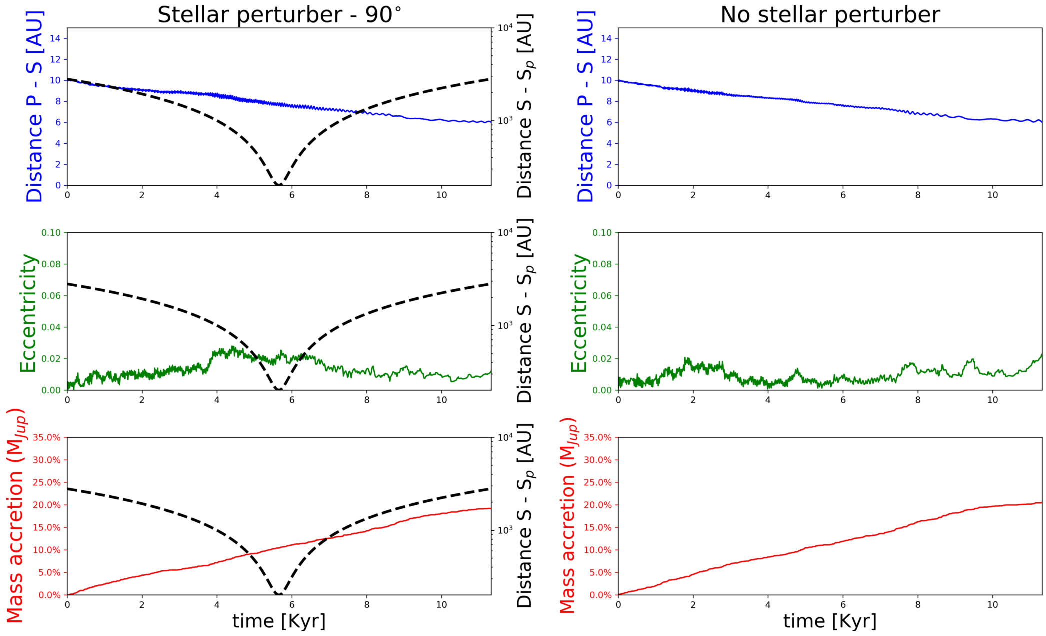

Figure A.6: Dynamical evolution of the distance (blue-solid line) between the Jovian planet (P) and the central star (S), the planetary eccentricity (green solid line) and the planetary mass accretion (red solid-line) during a stellar flyby of a perturber 1 $M_\odot$ (S_p) with a r_{per} 200 AU and orbital inclination $90°$ (black dash-line).

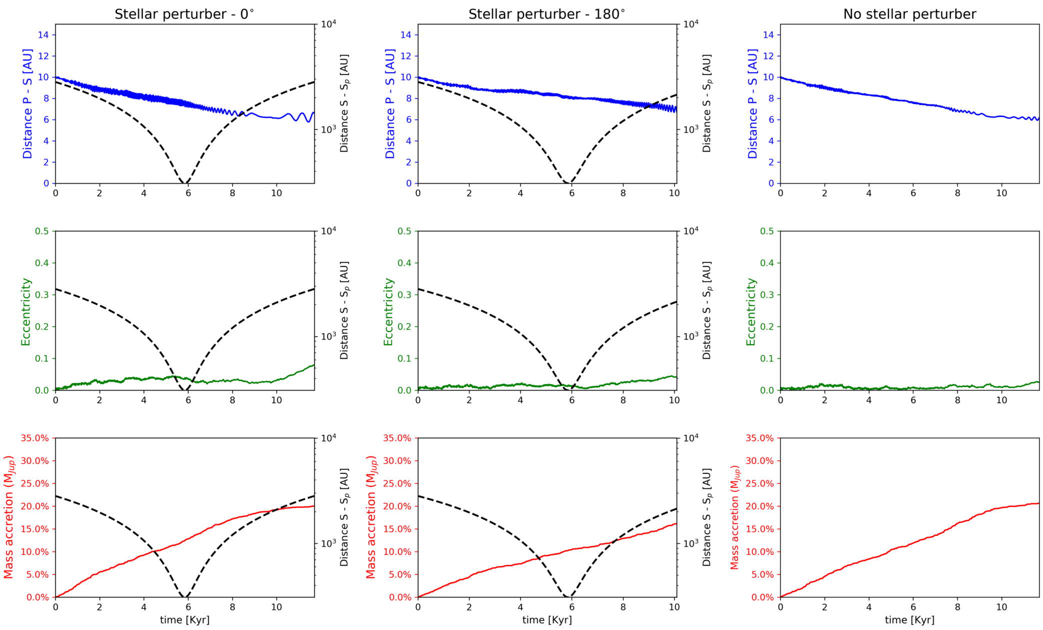

Figure A.7: Dynamical evolution of the distance (blue-solid line) between the Jovian planet (P) and the central star (S), the planetary eccentricity (green solid line) and the planetary mass accretion (red solid-line) during a stellar flyby of a perturber 1 $M_\odot$ (S_p) with a r_{per} 300 AU and orbital inclination $0°$ and $180°$ (black dash-line).

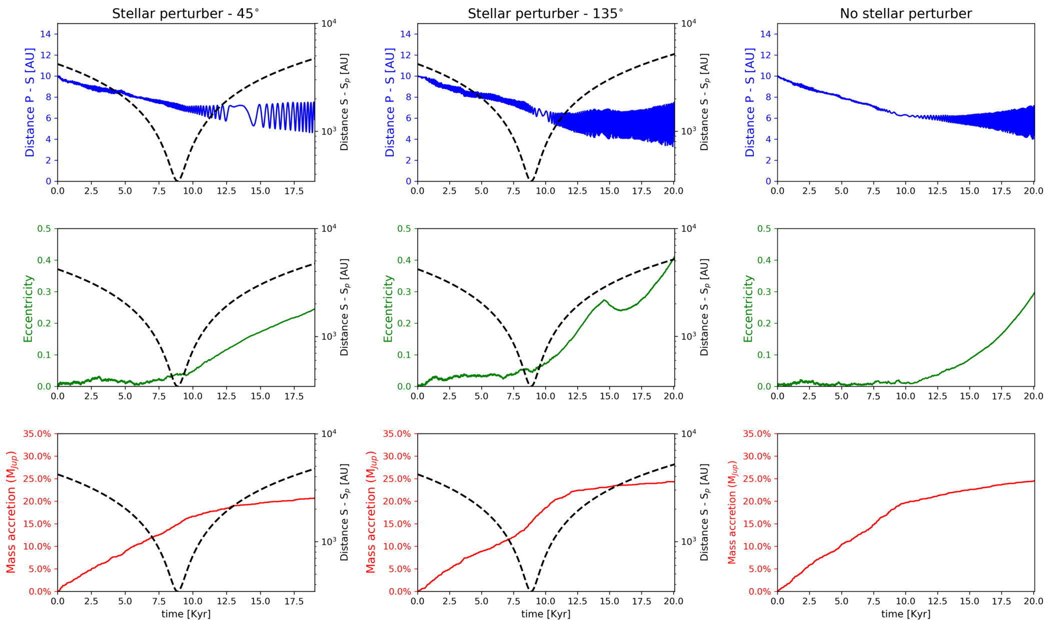

Figure A.8: Dynamical evolution of the distance (blue-solid line) between the Jovian planet (P) and the central star (S), the planetary eccentricity (green solid line) and the planetary mass accretion (red solid-line) during a stellar flyby of a perturber 1 $M_\odot$ (S_p) with a r_{per} 300 AU and orbital inclination $45°$ and $135°$ (black dash-line).

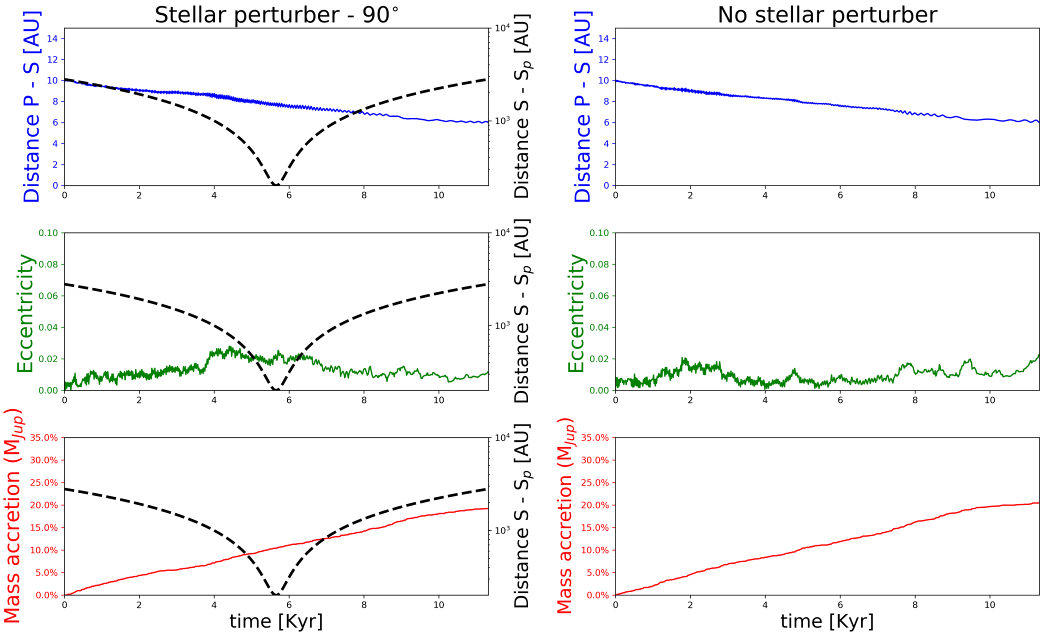

Figure A.9: Dynamical evolution of the distance (blue-solid line) between the Jovian planet (P) and the central star (S), the planetary eccentricity (green solid line) and the planetary mass accretion (red solid-line) during a stellar flyby of a perturber 1 M$_\odot$ (S$_p$) with a r$_{per}$ 300 AU and orbital inclination $90°$ (black dash-line).

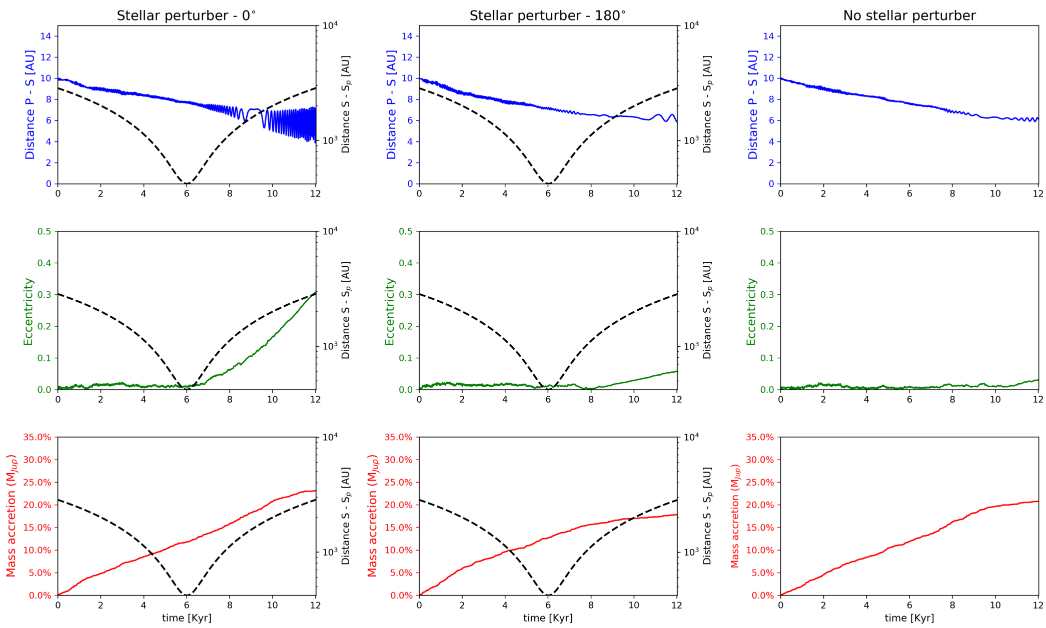

Figure A.10: Dynamical evolution of the distance (blue-solid line) between the Jovian planet (P) and the central star (S), the planetary eccentricity (green solid line) and the planetary mass accretion (red solid-line) during a stellar flyby of a perturber 1 $M_{\odot}$ (S_p) with a r_{per} 400 AU and orbital inclination $0°$ and $180°$ (black dash-line).

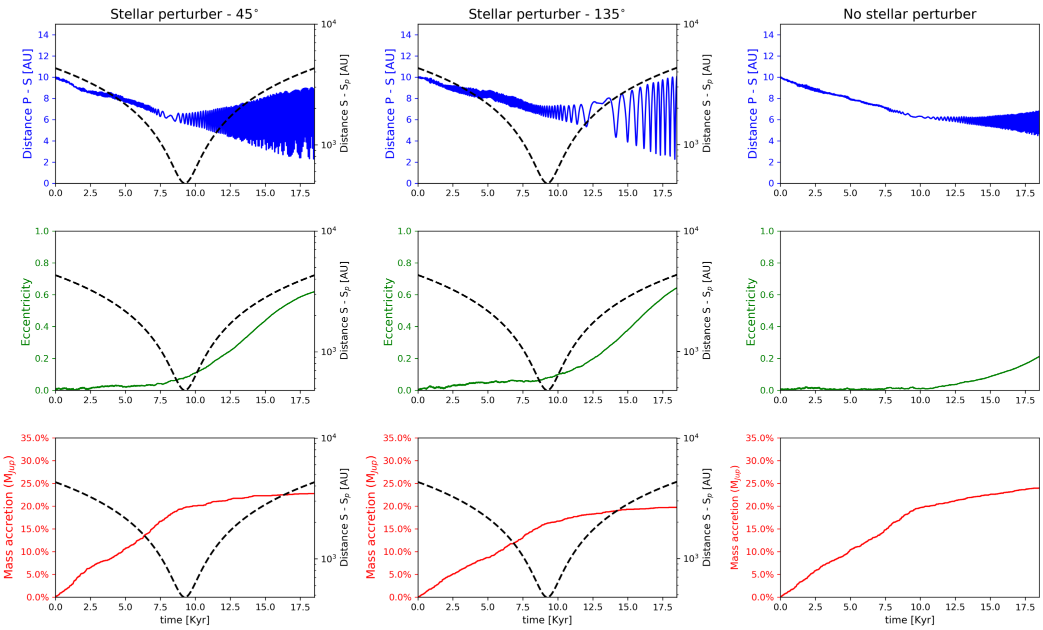

Figure A.11: Dynamical evolution of the distance (blue-solid line) between the Jovian planet (P) and the central star (S), the planetary eccentricity (green solid line) and the planetary mass accretion (red solid-line) during a stellar flyby of a perturber 1 M$_\odot$ (S$_p$) with a r$_{per}$ 400 AU and orbital inclination 45° and 135° (black dash-line).

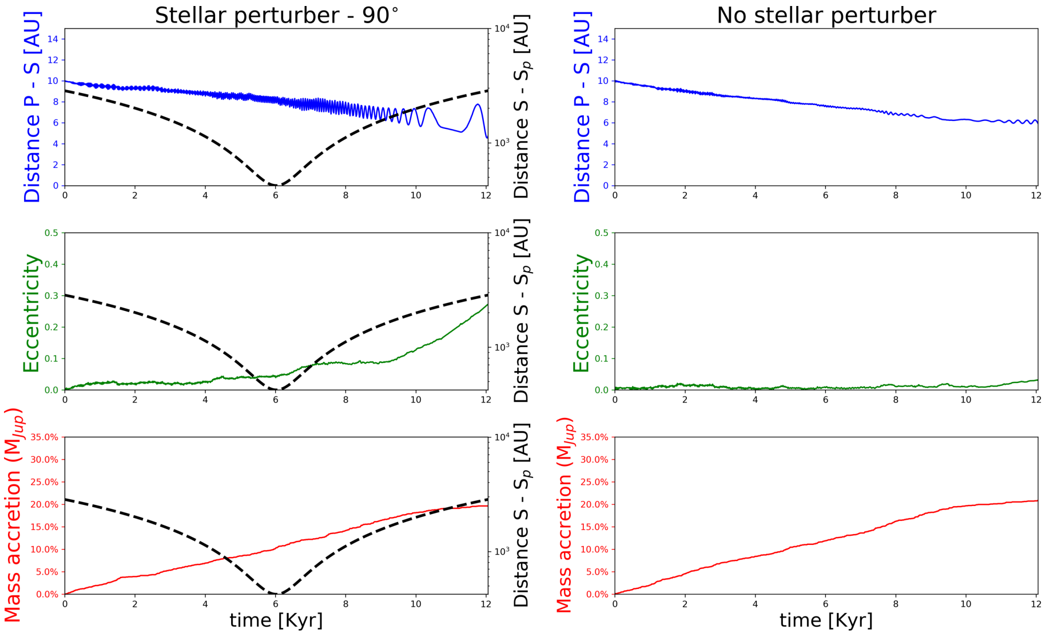

Figure A.12: Dynamical evolution of the distance (blue-solid line) between the Jovian planet (P) and the central star (S), the planetary eccentricity (green solid line) and the planetary mass accretion (red solid-line) during a stellar flyby of a perturber 1 $M_{\odot}$ (S_p) with a r_{per} 400 AU and orbital inclination $90°$ (black dash-line).

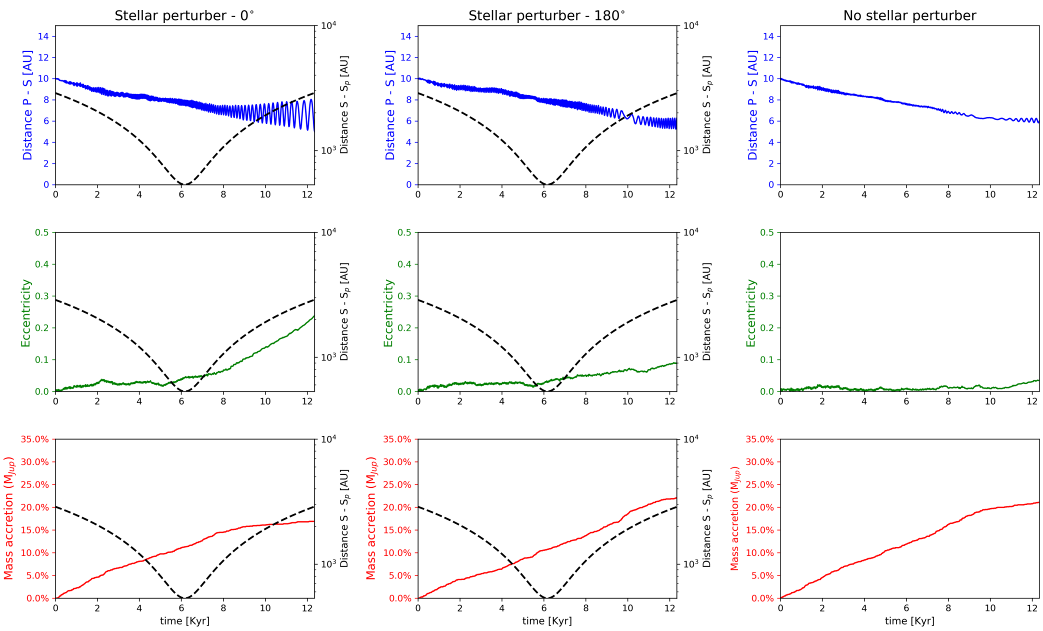

Figure A.13: Dynamical evolution of the distance (blue-solid line) between the Jovian planet (P) and the central star (S), the planetary eccentricity (green solid line) and the planetary mass accretion (red solid-line) during a stellar flyby of a perturber 1 $M_\odot$ (S_p) with a r_{per} 500 AU and orbital inclination $0°$ and $180°$ (black dash-line).

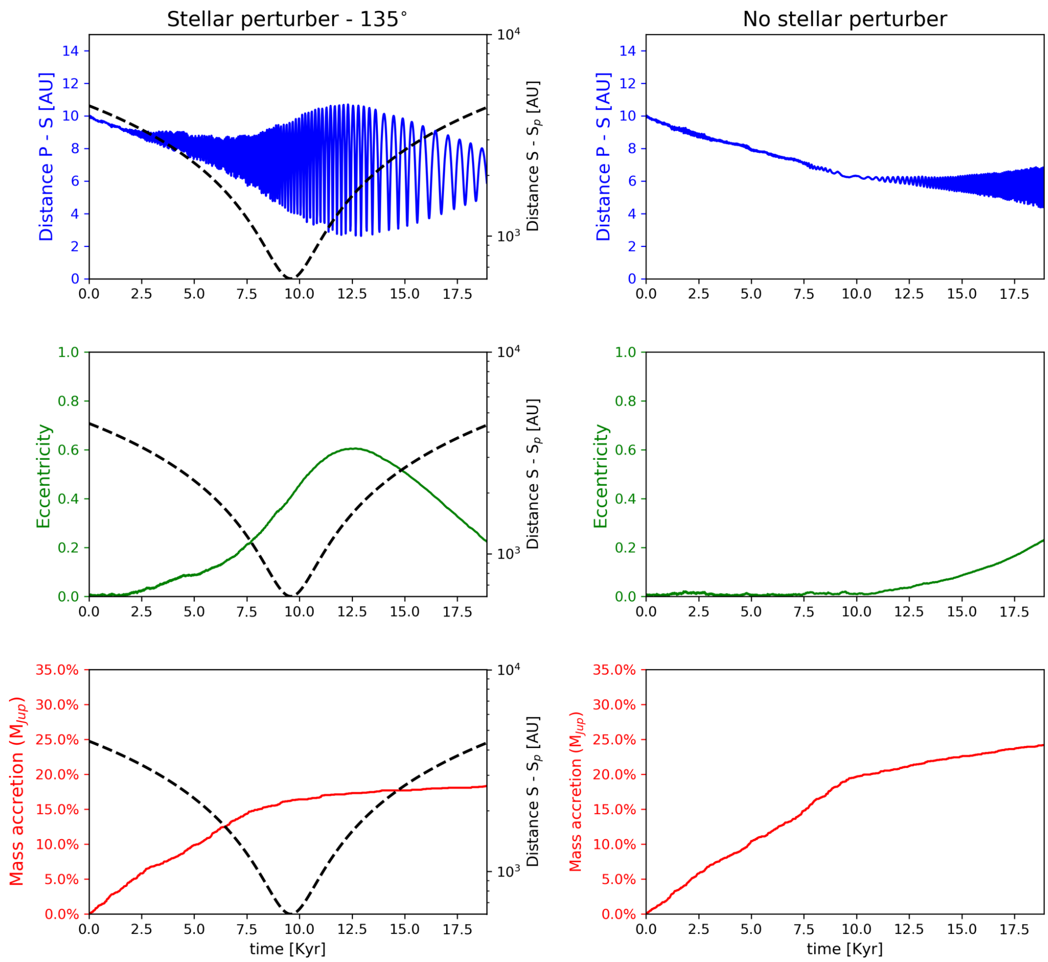

Figure A.14: Dynamical evolution of the distance (blue-solid line) between the Jovian planet (P) and the central star (S), the planetary eccentricity (green solid line) and the planetary mass accretion (red solid-line) during a stellar flyby of a perturber 1 $M_\odot$ (S_p) with a r_{per} 500 AU and orbital inclination 135° (black dash-line).

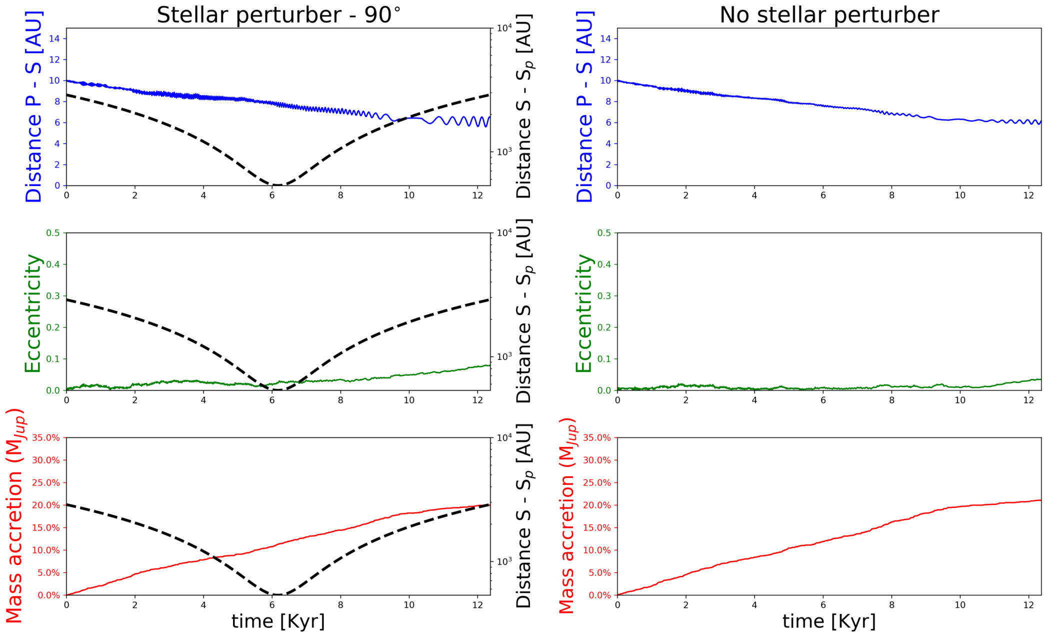

Figure A.15: Dynamical evolution of the distance (blue-solid line) between the Jovian planet (P) and the central star (S), the planetary eccentricity (green solid line) and the planetary mass accretion (red solid-line) during a stellar flyby of a perturber 1 $M_\odot$ (S_p) with a r_{per} 500 AU and orbital inclination $90°$ (black dash-line).

Appendix B

Tables of results

Below we list the tables of results for each stellar perturber 0.5 $M_{\odot}$, 0.8 $M_{\odot}$, 1 $M_{\odot}$, 3 $M_{\odot}$ and 8 $M_{\odot}$. We list, for each inclination and periastron of the orbit of the stellar perturber:

- The final Lagrangian radii 63.2% of the final total mass of the disk.
- The final mean distance, $<r>$, final mean eccentricity, $<e>$, and final mass accretion of the Jovian planet.

Table B.1: Final Lagrangian radii 63.2% of the final total mass of the disk for the model of the stellar perturber 0.5 $M_\odot$.

$r_{63.2\%}$					
r_{per}	$0°$	$45°$	$90°$	$135°$	$180°$
100 AU	**44.57** AU	**43.50** AU	**59.68** AU	**38.10** AU	**36.24** AU
200 AU	**46.66** AU	**54.73** AU	**42.63** AU	**46.50** AU	**61.02** AU
300 AU	**45.95** AU	**54.44** AU	**58.81** AU	**64.97** AU	**60.14** AU
400 AU	**50.07** AU	**48.60** AU	**49.40** AU	**49.54** AU	**48.23** AU
500 AU	**47.38** AU	**49.04** AU	**19.83** AU	**48.63** AU	**46.79** AU

Table B.2: Final mean distance $<r>$, final mean eccentricity $<e>$ and final mass accretion of the Jovian planet for each inclination and periastron of the orbit of the stellar perturber 0.5 M$_\odot$.

$0°$

	100 AU	200 AU	300 AU	400 AU	500 AU
$<r>$	**5.06** AU	**5.11** AU	**6.04** AU	**5.90** AU	**5.68** AU
$<e>$	**0.05**	**0.02**	**0.02**	**0.11**	**0.01**
M$_{Jup}$%	**22.21%**	**22.64%**	**19.30%**	**20.11%**	**20.38%**

$45°$

	100 AU	200 AU	300 AU	400 AU	500 AU
$<r>$	**6.34** AU	**6.53** AU	**6.37** AU	**5.44** AU	**6.00** AU
$<e>$	**0.09**	**0.25**	**0.57**	**0.39**	**0.19**
M$_{Jup}$%	**16.12**%	**20.27**%	**19.41**%	**26.57**%	**21.13**%

$90°$

	100 AU	200 AU	300 AU	400 AU	500 AU
$<r>$	**8.74** AU	**6.70** AU	**5.44** AU	**5.92** AU	**5.50** AU
$<e>$	**0.32**	**0.47**	**0.04**	**0.04**	**0.09**
M$_{Jup}$%	**13.20**%	**15.51**%	**19.51**%	**18.00**%	**21.65**%

$135°$

	100 AU	200 AU	300 AU	400 AU	500 AU
$<r>$	**5.71** AU	**5.68** AU	**6.82** AU	**5.01** AU	**5.64** AU
$<e>$	**0.11**	**0.04**	**0.12**	**0.43**	**0.10**
M$_{Jup}$%	**19.61**%	**20.41**%	**17.90**%	**26.29**%	**22.17**%

$180°$

	100 AU	200 AU	300 AU	400 AU	500 AU
$<r>$	**7.93** AU	**5.84** AU	**6.16** AU	**6.50** AU	**6.13** AU
$<e>$	**0.20**	**0.03**	**0.08**	**0.07**	**0.06**
M$_{Jup}$%	**12.82**%	**17.28**%	**19.33**%	**16.70**%	**18.22**%

Table B.3: Final Lagrangian radii 63.2% of the final total mass of the disk for the model of the stellar perturber 0.8 $M_\odot$.

$r_{63.2\%}$					
r_{per}	$0°$	$45°$	$90°$	$135°$	$180°$
100 AU	**42.64** AU	**40.89** AU	**46.92** AU	**32.81** AU	**45.75** AU
200 AU	**45.15** AU	**68.35** AU	**56.81** AU	**44.99** AU	**49.26** AU
300 AU	**47.53** AU	**73.85** AU	**57.63** AU	**53.59** AU	**46.12** AU
400 AU	**48.68** AU	**55.72** AU	**62.75** AU	**54.26** AU	**62.48** AU
500 AU	**45.64** AU	**52.24** AU	**55.62** AU	**53.17** AU	**45.81** AU

Table B.4: Final mean distance $<r>$, final mean eccentricity $<e>$ and final mass accretion of the Jovian planet for each inclination and periastron of the orbit of the stellar perturber 0.8 M$_\odot$.

0°					
	100 AU	200 AU	300 AU	400 AU	500 AU
$<r>$	**6.65** AU	**6.41** AU	**6.00** AU	**5.78** AU	**5.53** AU
$<e>$	**0.13**	**0.06**	**0.11**	**0.11**	**0.09**
M$_{Jup}$%	**16.84%**	**17.53%**	**18.14%**	**20.38%**	**22.22%**

45°					
	100 AU	200 AU	300 AU	400 AU	500 AU
$<r>$	**6.06** AU	**5.49** AU	**6.58** AU	**6.13** AU	**5.37** AU
$<e>$	**0.13**	**0.25**	**0.30**	**0.24**	**0.19**
M$_{Jup}$%	**20.30**%	**22.61**%	**17.43**%	**21.30**%	**25.24**%

90°					
	100 AU	200 AU	300 AU	400 AU	500 AU
$<r>$	**6.82** AU	**5.54** AU	**6.65** AU	**5.88** AU	**5.98** AU
$<e>$	**0.08**	**0.03**	**0.08**	**0.03**	**0.06**
M$_{Jup}$%	**14.82**%	**20.90**%	**16.38**%	**18.55**%	**20.32**%

135°					
	100 AU	200 AU	300 AU	400 AU	500 AU
$<r>$	**5.95** AU	**7.76** AU	**6.78** AU	**6.46** AU	**6.55** AU
$<e>$	**0.09**	**0.29**	**0.24**	**0.38**	**0.36**
M$_{Jup}$%	**19.62**%	**17.88**%	**20.75**%	**23.74**%	**19.47**%

180°					
	100 AU	200 AU	300 AU	400 AU	500 AU
$<r>$	**7.73** AU	**5.66** AU	**6.58** AU	**6.36** AU	**6.18** AU
$<e>$	**0.28**	**0.12**	**0.09**	**0.16**	**0.12**
M$_{Jup}$%	**12.22%**	**20.45%**	**16.25%**	**19.56%**	**17.76%**

Table B.5: Final Lagrangian radii 63.2% of the final total mass of the disk for the model of the stellar perturber 1 $M_{\odot}$.

			$r_{63.2\%}$		
r_{per}	$0°$	$45°$	$90°$	$135°$	$180°$
100 AU	**40.63** AU	**57.95** AU	**47.58** AU	**33.85** AU	**27.82** AU
200 AU	**44.71** AU	**48.54** AU	**52.10** AU	**38.12** AU	**41.21** AU
300 AU	**47.40** AU	**49.40** AU	**51.41** AU	**53.15** AU	**44.09** AU
400 AU	**48.28** AU	**52.84** AU	**57.41** AU	**51.98** AU	**62.26** AU
500 AU	**52.32** AU	**54.57** AU	**56.81** AU	**53.53** AU	**58.73** AU

Table B.6: Final mean distance $<r>$, final mean eccentricity $<e>$ and final mass accretion of the Jovian planet for each inclination and periastron of the orbit of the stellar perturber 1 $M_\odot$.

0°					
	100 AU	200 AU	300 AU	400 AU	500 AU
$<r>$	**6.74** AU	**5.89** AU	**6.16** AU	**5.85** AU	**7.55** AU
$<e>$	**0.05**	**0.23**	**0.08**	**0.31**	**0.24**
$M_{Jup}\%$	**14.40%**	**22.13%**	**20.03%**	**23.12%**	**16.91%**

45°					
	100 AU	200 AU	300 AU	400 AU	500 AU
$<r>$	**5.90** AU	**5.20** AU	**6.89** AU	**6.36** AU	**6.63** AU
$<e>$	**0.32**	**0.16**	**0.25**	**0.62**	**0.43**
$M_{Jup}\%$	**23.04%**	**25.20%**	**20.69%**	**22.78%**	**21.74%**

90°					
	100 AU	200 AU	300 AU	400 AU	500 AU
$<r>$	**6.54** AU	**5.70** AU	**6.81** AU	**6.55** AU	**6.24** AU
$<e>$	**0.01**	**0.01**	**0.08**	**0.27**	**0.08**
$M_{Jup}\%$	**16.64**%	**19.23**%	**14.45**%	**19.66**%	**19.99**%

135°					
	100 AU	200 AU	300 AU	400 AU	500 AU
$<r>$	**6.24** AU	**7.09** AU	**5.74** AU	**7.45** AU	**7.44** AU
$<e>$	**0.33**	**0.04**	**0.41**	**0.71**	**0.22**
$M_{Jup}\%$	**21.56**%	**15.49**%	**24.35**%	**20.13**%	**18.33**%

180°					
	100 AU	200 AU	300 AU	400 AU	500 AU
$<r>$	**6.06** AU	**5.70** AU	**7.02** AU	**5.96** AU	**6.12** AU
$<e>$	**0.18**	**0.10**	**0.04**	**0.06**	**0.09**
$M_{Jup}\%$	**19.66%**	**21.35%**	**16.14%**	**17.81%**	**22.04%**

Table B.7: Final Lagrangian radii 63.2% of the final total mass of the disk for the model of the stellar perturber 3 M$_{\odot}$.

			r$_{63.2\%}$		
r$_{per}$	$0°$	$45°$	$90°$	$135°$	$180°$
100 AU	**39.37** AU	**50.44** AU	**51.52** AU	**38.85** AU	**26.11** AU
200 AU	**48.23** AU	**65.53** AU	**54.78** AU	**40.40** AU	**35.14** AU
300 AU	**48.73** AU	**68.18** AU	**60.56** AU	**53.23** AU	**55.12** AU
400 AU	**46.28** AU	**70.23** AU	**68.23** AU	**65.96** AU	**54.58** AU
500 AU	**53.27** AU	**53.56** AU	**53.85** AU	**52.59** AU	**51.96** AU

Table B.8: Final mean distance $<r>$, final mean eccentricity $<e>$ and final mass accretion of the Jovian planet for each inclination and periastron of the orbit of the stellar perturber 3 $M_\odot$.

0°					
	100 AU	200 AU	300 AU	400 AU	500 AU
$<r>$	**5.55** AU	**6.05** AU	**4.61** AU	**5.82** AU	**5.40** AU
$<e>$	**0.06**	**0.42**	**0.27**	**0.12**	**0.12**
M_{Jup}%	**19.23%**	**21.34%**	**30.19%**	**21.52%**	**22.17%**

45°					
	100 AU	200 AU	300 AU	400 AU	500 AU
$<r>$	**6.07** AU	**7.06** AU	**5.74** AU	**6.97** AU	**6.92** AU
$<e>$	**0.58**	**0.43**	**0.38**	**0.25**	**0.31**
M_{Jup}%	**23.26%**	**19.54%**	**21.16%**	**21.22%**	**21.20%**

90°					
	100 AU	200 AU	300 AU	400 AU	500 AU
$<r>$	**6.19** AU	**6.39** AU	**6.12** AU	**6.73** AU	**5.12** AU
$<e>$	**0.15**	**0.22**	**0.11**	**0.13**	**0.04**
M_{Jup}%	**20.13%**	**20.37%**	**20.84%**	**21.13%**	**24.84%**

135°					
	100 AU	200 AU	300 AU	400 AU	500 AU
$<r>$	**4.45** AU	**5.20** AU	**6.34** AU	**6.35** AU	**6.26** AU
$<e>$	**0.46**	**0.15**	**0.64**	**0.28**	**0.66**
M_{Jup}%	**27.09%**	**23.21%**	**23.45%**	**23.35%**	**25.48%**

180°					
	100 AU	200 AU	300 AU	400 AU	500 AU
$<r>$	**5.61** AU	**7.62** AU	**5.66** AU	**6.12** AU	**6.23** AU
$<e>$	**0.10**	**0.62**	**0.12**	**0.20**	**0.18**
M_{Jup}%	**20.67%**	**17.19%**	**24.63%**	**20.65%**	**20.32%**

Table B.9: Final Lagrangian radii 63.2% of the final total mass of the disk for the model of the stellar perturber 8 $M_{\odot}$.

$r_{63.2\%}$					
r_{per}	$0°$	$45°$	$90°$	$135°$	$180°$
100 AU	**47.55** AU	**26.89** AU	**27.28** AU	**28.02** AU	**21.83** AU
200 AU	**66.35** AU	**45.83** AU	**46.98** AU	**35.48** AU	**30.20** AU
300 AU	**60.59** AU	**55.85** AU	**53.01** AU	**43.03** AU	**39.98** AU
400 AU	**53.30** AU	**52.44** AU	**49.69** AU	**48.79** AU	**45.61** AU
500 AU	**52.87** AU	**55.63** AU	**58.38** AU	**53.32** AU	**48.25** AU

Table B.10: Final mean distance, $<r>$, final mean eccentricity, $<e>$ and final mass accretion of the Jovian planet, $M_{Jup}\%$, for each inclination and periastron of the orbit of the stellar perturber 8 $M_{\odot}$.

0°					
	100 AU	200 AU	300 AU	400 AU	500 AU
$<r>$	**7.42** AU	**7.06** AU	**5.97** AU	**5.55** AU	**5.93** AU
$<e>$	**0.27**	**0.42**	**0.24**	**0.46**	**0.24**
$M_{Jup}\%$	**17.48%**	**19.94%**	**24.28%**	**27.19%**	**22.59%**

45°					
	100 AU	200 AU	300 AU	400 AU	500 AU
$<r>$	**6.46** AU	**4.53** AU	**6.30** AU	**8.14** AU	**7.22** AU
$<e>$	**0.70**	**0.19**	**0.70**	**0.42**	**0.58**
$M_{Jup}\%$	**23.42**%	**29.89**%	**22.97**%	**19.70**%	**18.96**%

90°					
	100 AU	200 AU	300 AU	400 AU	500 AU
$<r>$	**5.92** AU	**6.66** AU	**7.31** AU	**4.95** AU	**6.23** AU
$<e>$	**0.16**	**0.20**	**0.69**	**0.09**	**0.17**
$M_{Jup}\%$	**21.85**%	**17.54**%	**20.51**%	**26.90**%	**22.59**%

135°					
	100 AU	200 AU	300 AU	400 AU	500 AU
$<r>$	**5.73** AU	**5.83** AU	**5.19** AU	**8.00** AU	**6.53** AU
$<e>$	**0.74**	**0.69**	**0.47**	**0.64**	**0.55**
$M_{Jup}\%$	**34.28**%	**27.24**%	**29.07**%	**19.37**%	**24.20**%

180°					
	100 AU	200 AU	300 AU	400 AU	500 AU
$<r>$	**5.00** AU	**5.59** AU	**6.67** AU	**7.14** AU	**4.72** AU
$<e>$	**0.13**	**0.09**	**0.53**	**0.08**	**0.09**
$M_{Jup}\%$	**25.86%**	**23.07%**	**21.36%**	**16.95%**	**28.23%**